University of California

Los Angeles

Ultra-high strain rate behavior of FCC nanostructures

A dissertation submitted in partial satisfaction

of the requirements for the degree

Doctor of Philosophy in Mechanical Engineering

by:

Ryan Scott Crum

2016

ABSTRACT OF DISSERTATION

Ultra-high strain rate behavior of FCC nanostructures

by

Ryan Scott Crum

Doctor of Philosophy in Mechanical Engineering

University of California, Los Angeles, 2016

Professor Vijay Gupta, Chair

This work addresses the influence of ultra-high strain rates loading observed in our world today via ballistics, explosions and astrophysical collisions on well-defined metal structures. There is a plentiful amount of research examining metals at a macroscopic level that are subjected to ballistics and explosions but observing the microstructure is difficult as those procedures are fairly destructive testing mechanisms. Therefore, to understand the true mechanisms that occur in these loading situations a more novel technique is necessary. Modifications were made to the Laser Spallation Technique in order to load structures under a single transient wave pulse. This study characterized FCC nanostructures shock loaded at extreme pressures, strain rates and temperatures. By utilizing nanostructures, extremely large values of stain could be produced within the structure. It was first observed that at lower laser fluence levels and subsequently low stress states that there was a chemical activation of the surface of Cu

nanopillars. This occurred due to nanofacet formation on the surface of the nanopillars which left pristine Cu surfaces to recombine with the environment. Dislocation motion was also observed and clearly identified in Cu nanopillars, Cu nanobenches and Al nanopillars. Further studies analyzed Cu nanopillars subjected to higher laser fluence generated stress waves, which led to bending and axial shortening deformation. These deformations were observed at laser fluence values of 144.9 kJ/m^2 for bending and 303.3 kJ/m^2 for bulging similar to that of Taylor Impact experiments. To explore an even more extreme loading environment, a specialized test setup was employed to cryogenically cool the copper nanopillars to a temperature of 83K in an attempt to elucidate brittle behavior. Under these loading conditions the nanopillars continued to deform in a ductile manner but with delayed onset of both bending deformation and bulging deformation compared to the room temperature counterpart. Finally, the mechanical behavior of the Cu nanopillars was studied by nanocompression testing and compared to that of a reference nanopillar from the same substrate. The mechanical properties of the copper pillars were improved at lower laser fluence levels. At higher laser fluence levels, the tests were inconclusive as slight bending of the shock loaded Cu nanopillars rendered the comparison to the non-deformed reference nanopillar inconclusive.

The dissertation of Ryan Scott Crum is approved.

Suneel Kodambaka

Christopher S. Lynch

Ajit K. Mal

Vijay Gupta, Committee Chair

University of California, Los Angeles

2016

This is dedicated to my family and friends that have helped me get to this stage and will continue with me beyond!

Table of Contents

List of Figures

Acknowledgements

I would like to thank my advisor Professor Vijay Gupta for allowing me the independence of exploring different fields of study. He provided encouragement and was helpful at all stages of my development. I would like to thank my committee members Professors Kodambaka, Lynch, and Mal for being part of my committee and providing much needed guidance.

As well, during my time at UCLA, I have come across many people that aided in my development and helped me along the way.

Finally, I would like to thank my family and friends. Their encouragement, love and support have helped me get to this point.

Vita

2007	Saint Stephen's Episcopal School Bradenton, Florida
2011	B.S. Physics with a minor in Economics Davidson College Davidson, North Carolina
2013	M.S. Mechanical Engineering University of California, Los Angeles Los Angeles, California

1 Introduction

Metals have been mechanically studied for many years under varying loading situations. As time has progressed, the majority of literature has addressed all of the different types of loading situations imaginable. Tests at low strain rates have been common for hundreds of years while more sophisticated high strain rate tests are more recent and need to be studied more. The highest of the strain rates observed in our world today are that of ballistics, explosions and astrophysical collisions. There is a plentiful amount of research examining metals at a macroscopic level that are subjected to ballistics and explosions. As one could imagine, these are fairly destructive testing mechanisms. Therefore, to understand the true mechanisms that occur in these loading situations a more novel technique is necessary. By completing these tests, we can further understand how metals deform under shock/blast loading and therefore engineer/optimize materials that will be able to withstand these types of loading for shielding as well as determine defeat mechanisms of protective shielding.

1.1 Motivation of Present Study

By measuring and understanding the deformation mechanisms of metals under shock/blast loading, we can learn how to optimize protective shieldings as well as determine defeat mechanisms within a structure under these types of loading. It should be recognized that the primary materials that are used in this study are copper and aluminum, both of which are not ideal structural materials. What works well with these

materials is the fact that they are very common FCC metals in which a significant amount of research has been published upon. Therefore, we expect that all known mechanisms that can occur will be easily found/known for these materials and any new mechanisms that may arise will be new and need explanations.

The Laser Spallation Technique, previously used to find adhesion strength of thin-films is modified in this study to create a single temporal stress pulse that is imparted upon the testing sample. These nanostructures are subjected to varying states of stress and temperatures, all at ultrahigh strain rates. As well, by utilizing nanostructures, we can explore the same structures both before and after the shock/blast loading by scanning electron microscopy (external structure) and transmission electron microscopy (internal structure).

1.2 Objectives of Present Study

The intentions of this study are:

1. To investigate deformation mechanisms of FCC metals at high strain rates.
2. To investigate stress dependence of deformation mechanisms in FCC metals at high strain rates.
3. To investigate temperature dependence of deformation mechanisms in FCC metals at high strain rates.
4. To characterize the mechanical properties of nanostructures after shock loading.

(a) Nanopillars will have some standard dislocation structure to start with, forcing the material to either nucleate new dislocations or move current dislocations (e.g. stacking faults tetrahedra, nano-voids, and twinning).

(b) The small sample size will present limitations on defect-defect interaction because of the large surface-to-volume ratio.

(c) Utilizing Al and Cu allows for the study of a low Peierls barrier and low stacking fault energy metal on dislocation and defect motion.

(d) Loading small pillars of lengths 1000 nm with such large pressures should generate very high strains. Unlike gas gun methodologies that generate *square stress pulses* of *several microseconds* in duration, the laser-generated stress waves with rarefaction shock can be tuned to cause material deformation (nucleation of defects, their propagation or formation of metastable phases) at any point along the ramp, including very near the pulse amplitude. The advantage of this approach is that the maximum time over which material is subjected to shock is less than 5 nanoseconds (when deformed at peak amplitude). This already knocks the *nominal* dynamic deformation time by three orders of magnitude (i.e. x1000) compared with what is possible with the current gas gun facilities. In this regard, the proposed research will be a first step toward closing the wide gap between the material deformation times (~picoseconds) that can be afforded in the molecular dynamics (MD) simulations and the current experimental setups. These MD simulations predict several defect structures and metastable phases that were previously not experimentally verifiable because of the experimental constraints mentioned above.

(e) Since shock loading will be performed on discrete samples, it provides an extremely powerful tool to experimentally correlate the evolved structures to experimental parameters of pressure and strain rate with minimal modeling. MD simulations can be carried out virtually in the same geometries as the shock experiments and thereby allowing for a direct comparison between the two. This should help establishing the basis for the experimentally observed new deformation mechanisms or vice versa where the experiments can be tuned to capture deformation modes uncovered during specific MD simulations.

(f) This experimental shock profile allows for a direct comparison with MD simulations, including evolution of substructures predicted at small time steps. This is because in a typical time step of 0.5 to 5 ps for MD simulations, the stress wave travels a distance that is of the order of the length of the nanopillars considered in this work. Also, the time duration of the stress pulse is on the order of a few nanosecond when at its peak stress.

1.3 Document Organization

Because of the multitude of disciplines utilized in this study, Chapter 2 is dedicated to provide a better understanding of the current high strain rate testing methodologies, the laser spallation technique and our modifications, stress state analysis via interferometry, the characteristics of FCC metals, characterization via electron microscopy, sample preparation via focused ion beam (FIB) and the Hysitron nanoindentation system. Chapters 3, 4, and 5 study the influence of low laser fluence generated stress waves on Cu nanopillars, Al nanopillars and Cu nanobenches, respectively. Chapter 6 probes the

same Cu nanopillars discussed in Chapter 3 but loaded by higher laser fluence generated stress waves. Chapter 7 discusses loading Cu nanopillars from low (38 kJ/m^2) to high (512.6 kJ/m^2) laser fluence levels at cryogenic temperatures (83K) and the resulting deformation. Chapter 8 addresses the mechanical properties of pillars loaded at room temperature characterized by nanocompression testing. Chapter 9 draws final conclusions from this study and offers new directions for future work.

2 Background

2.1 Introduction

Most of the current understanding of plastic deformation of metals at high strain rates is based on dislocation models, and is calibrated with experiments and Molecular Dynamics (MD) modeling. However, experimentally attained strain rates by Hopkinson bar and gas-gun loading are limited to 10^4 s^{-1} and 10^6 s^{-1}, respectively, while MD simulation strain rates are typically performed at strain rates in excess of 10^9 s^1. The basic dislocation mechanisms invoked in the calibration of shock compression experiments assume that dislocations already exist in the material, that they are initially pinned, and that their motion in response to the applied strain rate is controlled by two key phenomena: (1) thermal activation over pinning barriers; and (2) phonon drag during motion in-between barriers. A large variety of mainly phenomenological models are typically used to interpret and extrapolate shock compression data [1]–[7].

Recently, however, metal deformation under extreme strain rate conditions has revealed substantial inconsistencies with the conventional dislocation-barrier models. In pure FCC metals of low stacking fault energy, for example, dislocation barriers do not exist *a priori*, and the energy differential between twinning mode deformation and slip-type dislocation motion is very small, leading to a transition from dislocation-dominated deformation to twinning-dominated deformation [8]. Remington *et al*. [9] found that in FCC metals with low stacking fault energy (such as copper), shock compression initiated the twinning-slip transition and a new $\alpha \rightarrow \varepsilon$ (bcc to hcp) phase transformation in iron

during plastic deformation at sub-nanosecond time scales. Thin FCC metal samples subjected to high strain rate tension/compression have been shown by Kiritani and co-workers to be dislocation-free [10], [11]. This is a tantalizing prospect, which if understood, can lead to super-plasticity without dislocations. Various defect structures were observed by Kiritani and co-workers in Au and Cu, most notably, nano-voids and stacking fault tetrahedra [10], [11]. These observations are contrary to dislocation-based models (e.g. Johnson–Cook [7], Zerilli–Armstrong [6], the mechanical threshold stress (MTS) [5], thermal activation phonon drag [4], Steinberg–Lund [1], Steinberg–Guinan [2], and Preston–Tonks–Wallace [3] models). Large-scale MD simulations of shocked copper single crystals [12] have been performed with pre-existing dislocation sources in the form of prismatic loops. The simulations indicate that once the pressure ramp wave exceeds the threshold for either activating the source (~10 GPa) or homogeneous nucleation of dislocations (~30 GPa), a high density of dislocations and stacking faults is created, and the evolution towards 3D plastic relaxation behind the shock front commences [12], where the dislocation density relaxes by a factor of three.

Based on these prior works it can be concluded that metals when subjected to extreme conditions of stress and strain rate (beyond 10^4 s^{-1}) deform via new micromechanisms, which cannot be explained using conventional dislocation barrier-type models. The current work is motivated by these observations and aims at subjecting FCC nanostructures to stress and strain rate levels never investigated before via laser-generated stress waves of 1-2 ns rise times and strain rates exceeding 10^7 s^{-1}. Additionally, the novel profile of the interrogating stress wave allows investigation of

certain micromechanisms, which cannot be done using the current dynamic loading setups. Atomic-scale mechanisms allowing the material to rearrange itself even when subjected to such extreme conditions were uncovered by Scanning Electron Microscopy (SEM) and Transmission Electron Microscopy (TEM) analysis of the shocked samples and use of Selected Area Electron Diffraction (SAED) technique. Finally, the experimental observations were used to validate and refine MD simulations to model the new phenomena [13].

Remington et al. [14] discuss solid state experiments on single crystals (e.g., Cu, Fe, Ti) of varying orientations under extreme pressure (10-100 GPa) and strain rate (10^6 – 10^8 s^{-1}) conditions. Time resolved lattice response and phase were measured with dynamic X-ray diffraction while lattice compression, phase, and temperature were deduced by extended X-ray absorption fine structure (EXAFS) measurements. These experiments were backed by MD simulations and also a number of constitutive models were evaluated in light of their experimental observations. While it is not possible in this work to match the laser power levels and therefore generate very large shock pressures in large sample volumes, it has been shown that comparable extreme conditions can be obtained in this study because of small sample volume and ultra-short rise-time stress pulses. Even though the laser spallation assembly can only generate nominal stress levels on the 3-5 GPa range, the local strain levels within the nanopillars could be elevated by nearly 100 times by fabricating 1 μm tall pillars.

Loading small pillars of length 1 μm with such large pressures generates very high strains. Unlike gas gun methodologies that generate *square stress pulses* of *several microseconds* in duration, the laser-generated stress waves shock can be tuned to cause material deformation (nucleation of defects, their propagation or formation of metastable phases) at any point along the ramp, including very near the pulse amplitude. The advantage of this approach is that the maximum time over which material is subjected to shock is well below five nanoseconds (when deformed at peak amplitude). This already knocks down the *nominal* dynamic deformation time by three orders of magnitude (i.e. x1000) compared with what is possible with the current gas gun facilities. In this regard, the proposed research will be a first step toward closing the wide gap between the material deformation times (~picoseconds) that can be afforded in the molecular dynamics (MD) simulations and the current experimental setups. (These MD simulations predict several defect structures and metastable phases that were previously not experimentally verifiable because of the experimental constraints mentioned above.)

Similarly, even though use of dynamic X-ray diffraction and EXAFS measurements are beyond the scope of the proposed research it appears that loading a series of pillars by varying stress wave amplitudes may result in locking-in or isolation of different phases of evolving lattice/defect structures, which can be observed in TEM analysis of recovered samples. Essentially we can control the amount of stress that is *just* necessary for defect nucleation or propagation into a fully transformed state and to scale it in-between so as to lock-in various transformations in their evolutionary phases. That is, the limited volume of the material of the pillar that is constrained between its substrate

and a catcher plate should help pin down the deformed microstructure. These deformed structures are easily revealed through conventional SEM and TEM examination, before and after shock experiments. This luxury is often not capable of the gas-gun methodologies, studying the post-loading sample is not an option as the violent impact often will obliterate a sample.

Since shock loading was performed on single crystal samples, this study provides an extremely powerful tool to experimentally correlate the evolved structures to experimental parameters of pressure and strain rate with minimal modeling. MD simulations can be carried out virtually in the same geometries as the experiments and thereby allowing for a direct comparison. This direct comparison has led to two MD papers [13], [15] which continue to establish scientific underpinning for the experimentally observed new deformation mechanisms or vice versa where the experiments can be tuned to capture deformation modes uncovered during specific MD simulations.

Two figures are attached below that address the methods utilized to mechanically test materials systems at varying strain rates. Figure 2.1 is adapted from Ramesh [16]. In Ramesh's work [16] he characterizes the different regimes of strain rate; creep domain ($< 10^{-6}$ s^{-1}), quasistatic ($< 10^{-3}$ s^{-1}), high ($> 10^{2}$ s^{-1}), very high ($> 10^{4}$ s^{-1}) and ultrahigh ($> 10^{6}$ s^{-1}). Meyers [17] expands upon this with a table addressing the testing procedures, their associated strain rates and their dynamic considerations.

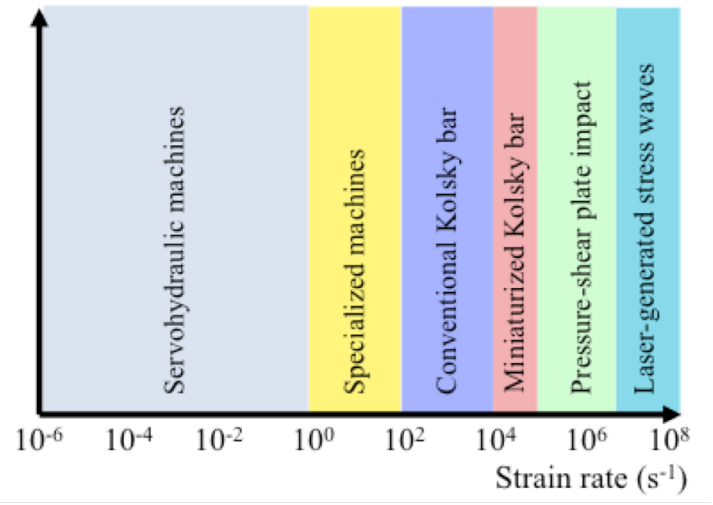

FIG. 2.1. A schematic covering the testing procedures utilized at various strain rates. Adapted from Ramesh [16].

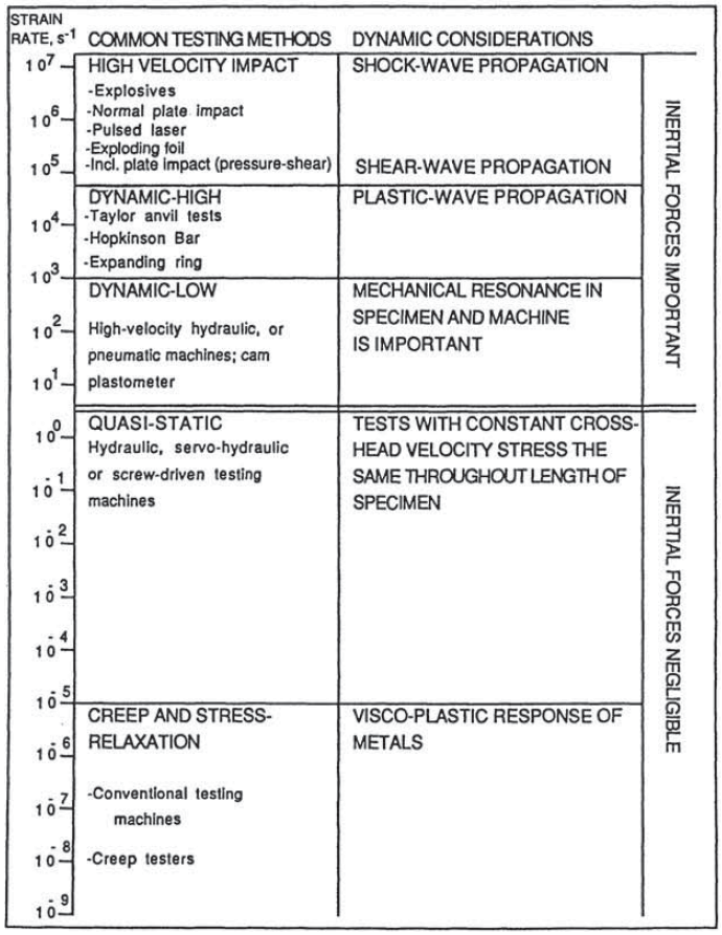

FIG. 2.2. Mechanical testing methods covering various strain rates. From Meyers [17].

2.2 Laser Spallation Technique

Gupta *et al*. [18]–[22] optimized laser-generated stress wave profiles for measuring the tensile strength of a thin film interface. In the laser spallation experiment (Fig. 2.3), a 2.5 nanosecond (ns) long Nd:YAG laser pulse is impinged over a 3 mm-dia area on a 0.5 μm thick Al film sandwiched between the back surface of a substrate disc (25 mm-dia and 1-mm thick) and a 50 to 100 μm thick layer of SiO_2. The melting-induced expansion of Al under confinement generates a compressive stress wave (with sub-nanosecond rise-time) directed towards the test coating, which is deposited on the substrate's front surface. The compression stress pulse reflects into a tensile wave from the coating's free surface and leads to its spallation (complete removal) at a sufficiently high amplitude. The spalling of the film occurs over a region of approximately 3 mm diameter and can be visually spotted. During this film separation process, the transient free surface velocity of the coating is continuously recorded using a state-of-the art optical interferometer [23], a schematic of which is shown towards the right in Fig. 2.3. Optical fringes corresponding to stress pulses of 1-2 ns rise-time and 16-20 ns total duration are recorded in a single shot mode, with a resolution of 5 ps. In addition, the novel design of the interferometer can handle reflection from optically rough surfaces. This ability of the interferometer is shown in Fig. 2.4a, which displays fringes obtained from the free surface of a bare glass substrate having a very thin metal reflective film on its free surface.

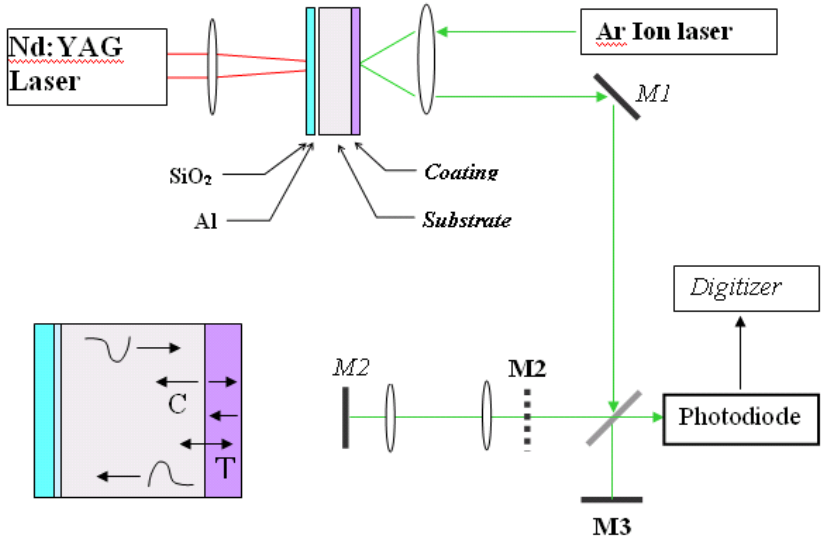

FIG. 2.3. Typical Interferometry setup

Next, the recorded fringe information is reduced to transient free surface velocity profile v(t) using standard interferometric procedures. Figure 2.4b shows the velocity profile obtained from the fringe record of Fig. 2.4a. For a coating of density ρ and thickness h, the interface stress σ can be calculated from the measured transient velocity v(t) as:

$$\sigma(t) = \frac{\rho c_o}{2}\left[v\left(t+\frac{h}{c}\right) - v\left(t-\frac{h}{c}\right)\right] \qquad (2.1)$$

where c is the longitudinal stress wave velocity in the film, which can be expressed in terms of the Lamé constant λ and the shear modulus μ as:

$$c = \sqrt{\frac{\lambda+2\mu}{\rho}} \qquad (2.2)$$

where λ is related to the Young's modulus E, the shear modulus μ, and the Poisson's ratio v, in the standard manner. Thus, with known values of these parameters, interfacial tensile strength can be calculated. Because of high strain rate loading, all inelastic effects

are largely suppressed during interface decohesion, and thus, the measured strengths are intrinsic and related directly to the atomic microstructure and chemistry of the interfacial region [24]–[26]. Using this technology, interfacial strengths in the range of 0.1 GPa to 2.5 GPa have been measured in a variety of engineering systems (paints, multilayer electronic devices, engines, tribology) involving metal, ceramic and polymeric coatings deposited on metal, semiconductor and ceramic substrates.

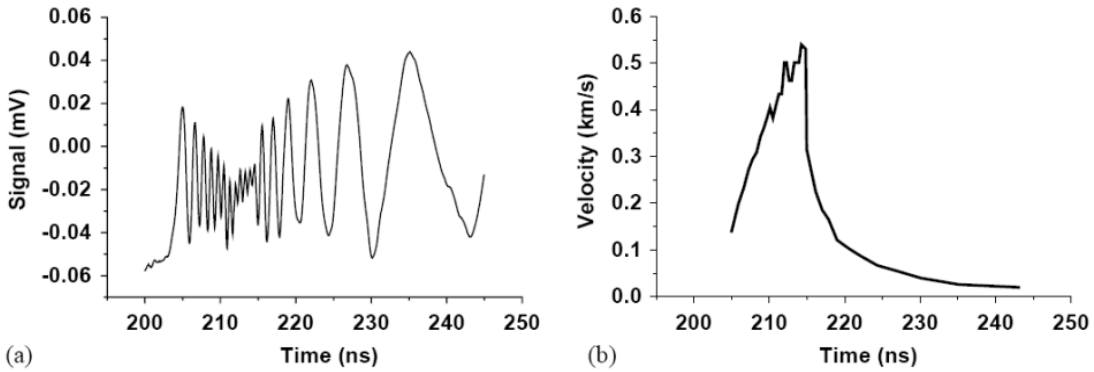

FIG. 2.4. (a) raw voltage vs. time signal collected in the digitizer from the interferometry setup and **(b)** the particle velocity profile measured from of the free surface.

When there is no coating, as is the case in this study, the above procedures can be used to generate and record well-defined stress waves in any substrate using the above procedures. An integral part of the film separation process is the profile of the stress wave. When any hard engineering substrate (e.g., Si, sapphire, etc.) is used, the above setup leads to generation of a transient stress wave profile that has sub-nanosecond rise-time and gradual post-peak decay. Peak amplitudes up to 5 GPa can be generated. Even with the gradual post-peak decay, the total pulse length is limited to only 50 to 100 ns in most substrates. The key to generating the short stress wave is the process of wave

shaping induced by the thin waterglass layer that constrains the laser-absorbing metal layer [20]. Upon laser-induced exfoliation of the constrained metal layer, compression waves are generated in opposite directions into the substrate and the waterglass layer. The compression wave in waterglass reflects into a tensile wave from its free surface and removes the still-ablating metal layer from the substrate. This essentially removes the heat source that is well known to be the cause of the elongated tail of the stress wave that is launched inside the substrate. The waterglass layer thickness is designed so that the reflecting tensile wave reaches the ablating layer when it is nearly fully ablated. This ensures generation of stress waves with highest pressure.

2.2.1 Modifications to the Laser Spallation Technique

Figure 2.5 shows the typical test setup for carrying out the following experiments. Nanostructures with desired material composition, crystallinity, and orientations are fabricated on the surface of a thin parent single crystal substrate. The flat featureless surface of the single crystal substrate is bonded to a glass substrate. Details of the fabrication are provided in Section 2.6. A catcher plate is then lapped onto the nanostructures (e.g., nanopillars) from the top. To match the acoustic impedance, a catcher plate of the same material as that forming the nanostructures is used. Other procedures to minimize the unloading waves coming back into the nanostructures were also used. This involves making sure the catcher plate is polished to a mirror finish as well as adding a low viscosity vacuum pump oil layer at the sample/catcher plate interface to allow more wave transmission compared to air.

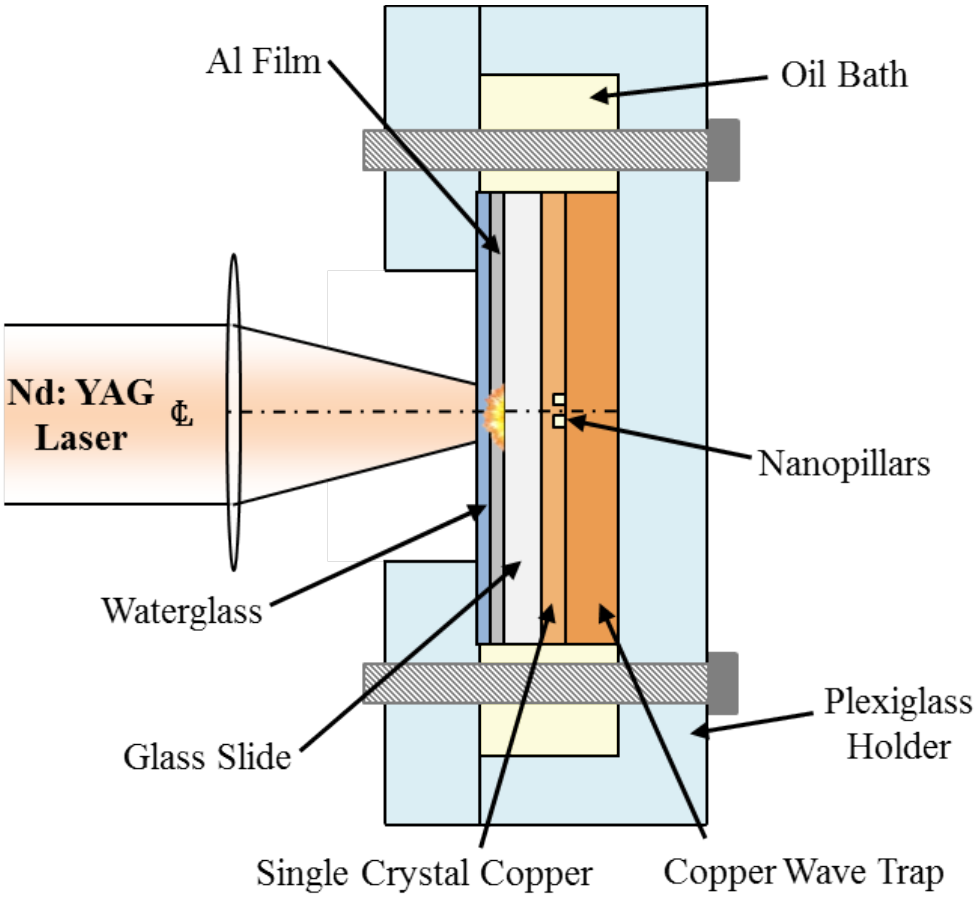

FIG. 2.5. Standard laser shock loading apparatus used on nanostructures.

Unlike the interface strength measurement strategy where the YAG laser pulse was focused onto a 3 mm diameter area, here we will focus the beam over a smaller diameter. The generated stress wave will load a group of nanostructures simultaneously. Because of the rather low area density of the nanostructures (e.g., nanopillars), the reflected waves from the pillar/catcher interface are likely to scatter away from the pillars into the adjoining pump oil/catcher plate interface and separate the catcher away from the pillars.

The advantage of using small nanostructured samples is that we can look at the initial and final deformed structure before and after high strain rate loading, without introducing

many errors stemming from sample to sample variability. The overall pressure amplitudes and rise times are obtained by using the same interferometric procedures as used to record stress waves in the interface strength measurement research. The local stress inside the nanopillars and the attendant strain and strain rate are computed using FEM and MD simulations. These local parameters will be related to any significant structural changes observed under a SEM and TEM.

2.2.2 1-D Wave Propagation Theory

In this study, a 1D wave propagation model has been assumed. In order for this to be true, there are specific requirements necessary for the material assembly. These requirements were provided by Lev and Argon [27]. In this work, Lev and Argon determined the range of validity of the 1D wave propagation model when compared its 3D counterpart for laser generated stress pulses. From this work, it was determined that 95% of the wave will remain in a columnar 1D manner for a propagation distance equal to the diameter of the laser heating spot. This naturally is dependent upon the geometry of the testing setup. There must not be any geometric confinement of the pulse in the radial direction. Therefore, the directions perpendicular/radial to the propagation of the stress pulse must also be sufficiently large for Lev and Argon's assumption to hold true.

With the understanding that the wave will travel in a 1D manner, the displacement of a free surface can be measured by Doppler/Michelson interferometry. This method is used in the laser spallation technique and is capable of characterizing the stress state of the experiments described herein. The 1D particle displacement (u) and velocity (v)

depends on position (x), time (t) and wave speed (c). The longitudinal wave speed is dependent upon the substrate material and for our calculations kept constant. From the use of 1D wave theory, the particle displacement and particle velocity within the substrate of interest can be defined as:

$$u(x,t) = u_s(t + {}^{x}/_{c}) + u_s(t - {}^{x}/_{c}) \tag{2.3}$$

and

$$v(x,t) = v_s(t + {}^{x}/_{c}) + v_s(t - {}^{x}/_{c}) \tag{2.4}$$

with subscript s for the substrate material. From linear elasticity, the stress and strain behavior in the material can be defined as:

$$\epsilon(x,t) = \frac{\partial u}{\partial x} = \frac{1}{c}[v_s(t + {}^{x}/_{c}) + v_s(t - {}^{x}/_{c})] \tag{2.5}$$

and

$$\sigma(x,t) = (\lambda + 2\mu)\frac{\partial u}{\partial x} = \rho c[v_s(t + {}^{x}/_{c}) + v_s(t - {}^{x}/_{c})] \tag{2.6}$$

where λ and μ are the Lamé constants. In the interferometry experiments there are significant boundary conditions to be considered. Equation 2.7 states that the free surface must be traction free and Equation 2.8 addresses the transient velocity (v_0) of the free surface from the interferometrically measured signal.

$$\sigma(0,t) = 0 \tag{2.7}$$

and

$$v_o(t) = v(0,t) = 2v_s(t) \tag{2.8}$$

From these calculations we obtain the transient stress state that causes the free surface displacement of the substrate:

$$\sigma_i = \sigma(h, t - \Delta t) = -\frac{1}{2}\rho c v_o(t) \tag{2.9}$$

where under lateral constraints, the wave speed within a material under uniaxial strain conditions is:

$$c = \sqrt{\frac{\lambda+2\mu}{\rho}} \tag{2.10}$$

With some manipulations, the free surface displacement and free surface velocity can be simplified to a profile determined by three variables α, β, and γ as shown below.

$$u_o(t) = \gamma\left\{-\alpha\left[e^{-t/\alpha} - 1\right] + \beta\left[e^{-t/\beta} - 1\right]\right\} \tag{2.11}$$

and

$$v_o(t) = \gamma\left\{\alpha e^{-t/\alpha} + \beta e^{-t/\beta}\right\} \tag{2.12}$$

Where the raw interferometry signal can be fit by the generalized equation:

$$A_o(t) = \frac{A_{max}+A_{min}}{2} + \frac{A_{max}-A_{min}}{2}\sin\left(\frac{4\pi}{\lambda}u_o(t) + \delta\right) \tag{2.13}$$

With A_{max} being the global maximum of the signal, A_{min} being the global minimum of the signal, λ being the wavelength of frequency stabilized laser (632.8 nm), δ being the phase shift in radians and u_0 being the free surface displacement of the substrate.

Also of importance to this study is how the wave will transmit across different materials. This can be determined by the acoustic impedance (*Z*) of the materials:

$$Z = \rho c = \sqrt{\rho(\lambda + 2\mu)} \tag{2.14}$$

where the reflection coefficient (*R*) and transmission coefficient (*T*) are:

$$R = \frac{Z_2 - Z_1}{Z_1 + Z_2} \tag{2.15}$$

and

$$T = 1 - R \tag{2.16}$$

for a wave moving from medium 1 to medium 2. Therefore, Z_1 is the acoustic impedance of medium 1 and Z_2 is the acoustic impedance of medium 2.

2.3 Testing Setups

We provide well-defined test structures that enable systematic investigation of the role of shape on the mechanical behavior. SEM and TEM are used to determine the morphology, composition, and microstructure of these structures before and after the shock, which will help better understand the structure-property relationships. In order to understand the mechanical properties of the nanostructures post-loading, a Hysitron Pico-Indenter is utilized to back out the force vs. time and stress vs. time curves.

These experiments focus on Cu and Al since several MD simulations are already in place for these materials. Well-defined test structures such as nanopillars and nanobenches were fabricated from single-crystalline samples following the procedure described below. Using the procedures described in section 6 of this chapter, single-crystalline pillars and benches with a (100) crystal orientation were prepared for this study.

The process for fabricating single-crystalline nanostructures begins with commercially available single crystalline substrates (thickness ~ 0.5 mm) of orientation (001). Focused ion beams (FIB) are then used to etch desired geometries at selected regions of interest on the substrate. To this purpose, a dual-beam FIB/SEM facility available at UCLA is utilized for this study. For the fabrication of nanopillars, the height

(or the depth) can be controlled by the incident ion energy, flux, and time. Nanopillars with diameters of approximately 450 nm and lengths of 1.25 μm will be prepared using this technique. Previous studies have employed FIB to create 1D pillars of desired sizes and shapes for mechanical testing [28], [29].

2.4 Face Centered Cubic Structures and Dislocations

Face centered cubic (FCC) metals have very common slip planes {111} and directions <110>. Since there are four {111} planes and each of those planes has three <110> directions, there are 12 slip systems in a FCC unit cell. The {111} planes correspond to the closest packed direction of an FCC metal and the <110> relates to the shortest possible Burger's vector ($\vec{b}$) in an FCC crystal of ½ <110>. This direction is such because the energy of a dislocation (E_λ) is proportional to the square of the Burger's vector and therefore the shortest Burger's vector corresponds to the lowest energy state. In order for a metal to be ductile, it must have slip systems and low lattice resistance. In order to have deformation, there must be five active slip systems in a crystal. The lattice resistance, very low for FCC metals, is determined by the Peierls barrier or the critically resolved shear stress (σ_{CRSS}). As well, the FCC crystal has an ABCABC stacking structure, which is the closest packed structure possible. These FCC metals have common deformations through stacking faults, which arise from their low stacking fault (SF) energy. Cu has a SF energy of 43 mJ/m^2 while Al has a much larger 158 mJ/m^2 SF energy. These can often lead to stacking fault tetrahedral (SFT) which when the stacking fault energy is low will produce large SFTs. The previously mentioned ½ <110> direction is the ideal orientation of a Burger's vector in an FCC metal, also referred to as a perfect

dislocation. But, when it is energetically favorable, these perfect dislocations can decompose into partial dislocations. The most common partial dislocations are Shockley partials $\vec{b} = \frac{1}{6}<112>$, Frank partials $\vec{b} = \frac{1}{3}<111>$ and Stair rod partials $\vec{b} = \frac{1}{6}<110>$. When two partial dislocations interact, there can be the creation of a Lomer-Cottrell lock in which a pinning of the dislocations occurs and dislocation pile up ensues.

Of significant importance to this work is the lattice resistance of a given material. This lattice resistance is the critically resolved shear stress (σ_{CRSS}) or also referred to as the Peierls stress when at 0K. Therefore, the lattice resistance can be modeled as an energy barrier using the Gibbs free energy [30]. The Gibbs free energy (ΔG) is described as:

$$\Delta G = \Delta U - \tau \cdot V^* - T\Delta S \tag{2.17}$$

where ΔU is the intrinsic energy barrier (Peierls barrier), τ is the shear stress, V^* is the interaction volume, T is the temperature in Kelvin and ΔS is the entropy of the system. Therefore, this means that in order to increase the effective lattice resistance the stress state, interaction volume, temperature or entropy can increase. In these studies, the stress state and the temperature can be adjusted.

2.5 Electron Microscopy Characterization

2.5.1 Analysis using SEM

Scanning electron microscopy will be an important characterization tool for this study. Since this work depends upon nanostructures, observations of these structures are not capable with the human eye (resolution of 0.2 mm) so another tool is necessary. An

optical microscope is capable of high magnifications but has significant limitations in its resolution. One can determine the maximum theoretical resolution by the equation by a classical Rayleigh criterion of:

$$r = \frac{0.61 \cdot \lambda}{\mu \sin \alpha} \tag{2.18}$$

where r is the smallest distance that can be resolved, λ is the wavelength of the light or electron that is probing the sample, μ is the refractive index of the medium and α is the aperture angle. Ideally, the resolution given by just blue light will be ~250 nm while white light is ~550 nm. In order to obtain higher resolution, a shorter wavelength will be needed. In order to do so, one can use the de Broglie wavelength formulation, which states that:

$$\lambda \sim \frac{1.22}{\sqrt{E}} \tag{2.19}$$

where the wavelength (λ in nm) is inversely related to the square root of the energy (E in eV) of the particle or light. From this formulation, one could determine the wavelength of an electron. If an electron has an energy of 100 keV, its wavelength will then be ~ 0.0034 nm, much smaller than the diameter of an individual atom. By using high-energy electrons, one can obtain resolutions in the SEM approaching 1 nm which is much larger than the theoretical resolution using Equation 2.17 for a wavelength of 0.0034 nm. This is due to limitations of the resolution due to astigmatism, spherical aberration and chromatic aberration within a sample as well as the interaction volume of the electron beam and natural contrast that a sample may provide.

Within a SEM, there are multiple types of signals that can be captured. As the electron beam proceeds in a raster like probing of the sample, the sample will emit either

electrons or X-rays. The emission of X-rays occurs when a low energy electron is ejected from the atom in which a higher energy electron within the atom will transition to the lower state. When this transition occurs, the energy difference between the higher energy electron and the lower energy state is emitted by the atom in the form of an X-ray. Therefore, since different elements will have varying and discrete atomic energy levels, the emitted X-ray will be specific to the atom, hence a characteristic X-ray. Collection of these X-rays can help characterize elements that are present within a sample in EDS or EDX mode (Energy Dispersive Spectroscopy or Energy Dispersive X-rays). The other type of signal that can be captured is by emitted electrons. There are two common types of electrons that can be emitted, secondary and backscattered electrons. Secondary electrons refer to the low energy electrons that are ejected from the sample by the incident electron beam. These electrons are low energy and provide high resolution of the surface topography of a sample. Backscattered electrons are from the SEM's electron beam that elastically collides with a sample/atom. These signals provide significant information regarding the location of different elements present as high Z (atomic number) elements will be more likely to elastically interact with the incident electron beam compared to low Z elements.

2.5.2 Analysis using TEM

Transmission electron microscopy is another characterization tool that is of importance to this study. In the previous section, it was acknowledged that electrons are capable of attaining wavelengths of 0.0034 nm, smaller than an atomic diameter. One of the main reasons why the resolution of the SEM is limited to 1 nm is that there is a

significant interaction volume of the electron beam in the sample. Since SEM samples are generally thick, the electron beam will penetrate into the sample and can emit electrons or X-rays from a given volume, larger than the electron beam's diameter from the sample. In order to counter this one can make very thin samples that will be electron transparent within a TEM. For copper, a sample must be no thicker than 100 nm to be electron transparent. The electrons will then be diffracted through the crystallographic structure of the sample. This diffraction will be able to provide very high-resolution characterization of the sample. The resolution limits of a TEM approach 0.2 nm, which is on the order of atomic diameters. Therefore, TEM is able to provide information of a material on the atomic level, probing dislocations, defects, voids and other atomic sized structures.

In some TEM systems there is a dual SEM/TEM setup, which is shortened to STEM (scanning transmission electron microscope). In this type of machine, one can collect electrons that transmit through the sample and provide the TEM image but also can obtain the electrons and X-rays that do not pass through the sample and are emitted on the electron-beam incident side of the sample (SEM). In this setup since the interaction volume of the sample will be largely decreased one can obtain higher resolution SEM images and more precise EDS characteristic X-ray analysis.

2.6 Focused Ion Beam Milling

In this study, it was of importance to fabricate nanostructures in a repeatable manner. In order to obtain nanostructures (nanopillars and nanobenches) Focused Ion Beam (FIB) milling was utilized. FIB is a specific technique that uses ions, in this study

Gallium ions (Ga^+), to dislodge or mill atoms from a given substrate. This procedure is completed in a dual SEM/FIB system in which high resolution imaging can allow for uniform and consistent FIB prepared samples. Several variables are very important to the milling process, which include Ga^+ accelerating voltage, current, and mill time. In this work (Figure 2.6), groups of nanopillars or benches were fabricated within given regions of the substrate with an identification marking 'T' to allow for easy identification of the region within an optical microscope and SEM.

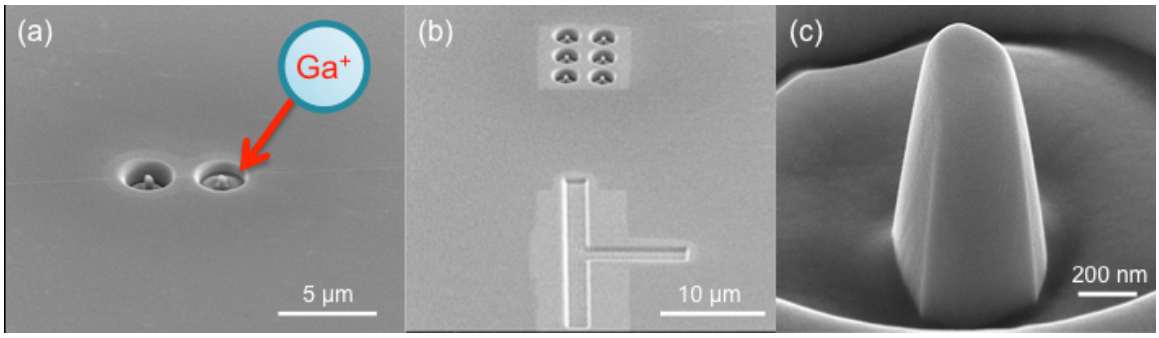

FIG. 2.6. Nanopillar fabrication process via FIB where **(a)** is during the process with the left pillar completed and the right pillar mid-milling, **(b)** is the final product with a region of 6 or 8 pillars located near the location 'T' marker and **(c)** is the final nanopillar product.

As mentioned in Section 2.5.2, it is necessary for a sample to be electron transparent in order to use the sample in a TEM. For copper, its thickness must be no more than 100 nm. Since the diameters of the nanostructures are approximately 450 nm, they will not be electron transparent. Therefore, a methodology will be necessary in order to obtain thin cross-sections from these given nanostructures. Once again, FIB will be used since mechanical polishing and thinning of the sample will be too cumbersome and plagued with potential error. The FIB lift off method is used in this study in order to

obtain an electron transparent cross-section from the nanostructures and is shown in Figure 2.7. This process begins with coating the nanostructures of interest with a protective carbon/platinum mix to prevent unnecessary damage from the FIB milling. Next FIB mills away the regions surrounding the area of interest and then undercuts the region. This is then followed by attaching a probe to the undercut sample and then completely detaching the region from the substrate and lifting it off the substrate. This cross-section is then adhered to a TEM grid or post and is ready for TEM analysis. The exact milling parameters and their values can be found in the appendix.

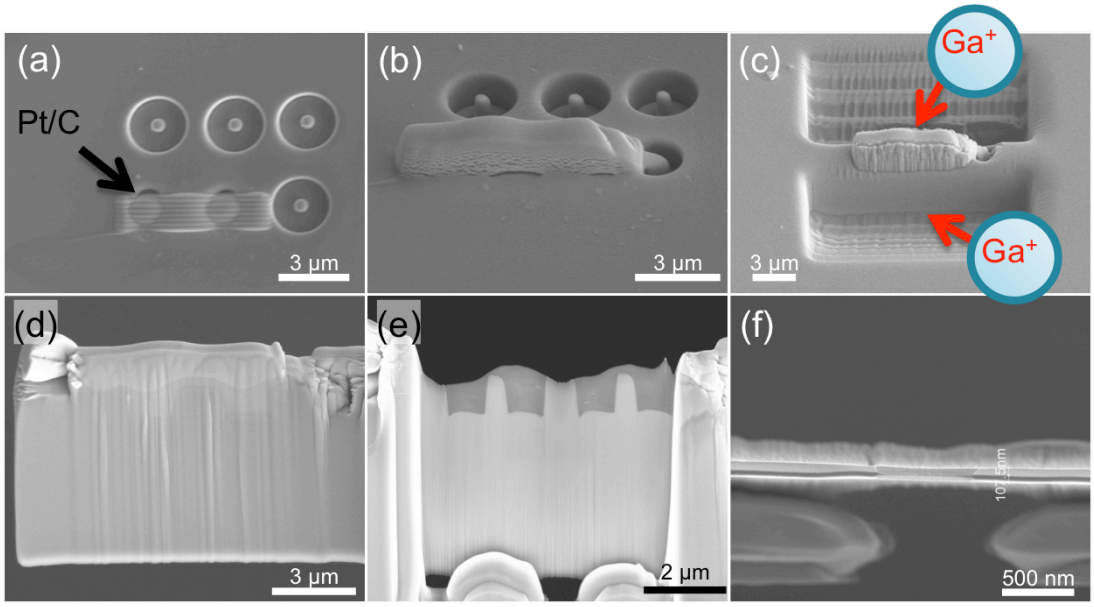

FIG. 2.7. Sample preparation via the lift off method. **(a), (b)** Coating the pillars of interest with a platinum carbon mix, **(c)** Milling material surrounding pillars away with Ga^+, **(d)** the cross-section that has been lifted off the substrate, **(e), (f)** a thinned to an electron transparent 100 nm TEM sample.

2.7 Hysitron Nanoindentation System

A testing procedure was needed in order to mechanically characterize the influence of the testing procedure upon these nanostructures. Typical low strain rate indentation tests nor Instron compression/tension tests were not possibilities due to their macroscopic scale when testing nanopillars. Hence, a specialized nano-compression system with precisely controlled alignment was needed. Several procedures and testing methodologies have been used in recent works for nano-scale structures [28], [29], [31]–[40]. This system utilized an SEM setup to be able to identify the location of the 10 μm boron doped diamond indenter head with fine precision. Either hardness or indentation tests are possible in this setup. For this study, indentation tests were obtained with a displacement control of 5 nm/s. This is a very low strain rate but is capable of producing force versus displacement curves and therefore stress versus strain curves.

3 Copper Nanopillars Loaded at Low Laser Fluence

3.1 Introduction

In the present work, we report on fabrication and shock loading of 100-oriented, single-crystalline, Cu nanopillars, with pillar axes aligned with the wave propagation (compression) direction. To this purpose, we developed an apparatus and related test procedures for the compression of Cu nanopillars at pressures and strain rates greater than 1 GPa and 10^7 s^{-1}, respectively using laser-generated stress waves of 1-2 ns rise-times and 16-20 ns total duration. Deformation mechanisms are identified by transmission electron microscopy (TEM) characterization of the residual microstructure in shock-loaded samples. The experimental approach presented here is general and applicable to shock loading of other materials. The experimentally-measured stress wave profiles and the sample microstructures can be used as input for large-scale MD and finite element simulations to help elucidate the underlying microscopic dislocation dynamics and the atomistics of deformation mechanisms.

3.2 Experimental Procedure

All experiments were carried out using single-crystalline Cu(001) pillars in the Laser Spallation Facility, developed previously to measure tensile strengths of interfaces [41]. Schematics of the experimental setup are shown in Figures 3.1 and 3.2. The Cu pillars (~ 1.20 μm tall and 0.45 μm in diameter) spanning approximately a 10 μm diameter were prepared out of Cu(001) substrates (10 mm × 10 mm × 0.5 mm purchased from MTI Corporation, Richmond, CA). Pillar dimensions were chosen so that the

morphologies of the as-prepared and shock-loaded pillars could be determined using electron microscopy. Four groups of 6 identical pillars were prepared in a Nova 600 Dual Beam focused-ion-beam/scanning electron microscope (FIB/SEM) system using gallium ions at 0.5 nA current and an accelerating voltage of 30 kV. Each of the four groups was separated from its neighbors by at least 5 mm so that each group of pillars could be independently loaded by the shock wave. This enabled us to carry out multiple tests on the same substrate.

In a typical experiment, the Cu sample was sandwiched between a 1-mm-thick glass substrate and a 9-mm-thick brass plate as shown in Figure 3.1. The back surface of the glass substrate was coated with a 0.5-μm-thick, laser absorbing Al film, which was constrained from the top by a transparent 20-50 μm thick layer of waterglass. The thicknesses of the Al and the waterglass layers were optimized by Yuan *et al.* [42] and Gupta *et al.* [42] to generate stress waves with the fastest rise times (< 1 ns) and shortest duration so that Cu pillars could be loaded under extreme conditions. Brass was chosen to minimize the wave reflection effects and maintain a uniaxial compressive state of stress in the copper nanopillars since it has a low acoustic impedance mismatch with the Cu substrate (3.7×10^7 Ns/m^3 for brass vs. 4.1×10^7 Ns/m^3 for Cu). Moreover, in order to preserve the deformation caused by the incoming stress wave, the brass plate was made very thick to geometrically disperse the waves and therefore decrease the possibility of any reloading of the pillars by the reflected waves. The glass substrate, copper sample, and the brass plate assembly was mechanically joined, sandwiched between two plexiglass plates and submerged in an oil bath to ensure proper coupling and continuity

between all the interfaces so that stress waves could transmit across them. A window was cut in the plexiglass plate to allow access to the YAG laser pulse, as shown in Figure 3.1.

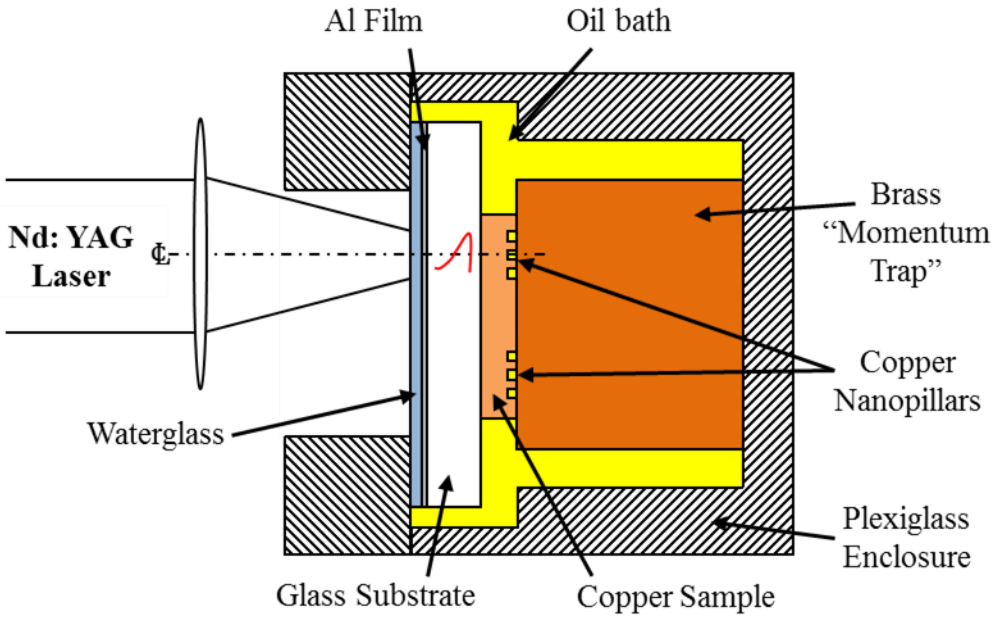

FIG. 3.1. Cross-sectional view of the experimental setup, showing two sets of nanopillars on a copper sample, oriented such that the axes of the pillars are aligned with the stress wave propagation direction.

In this setup, a nominal 8 ns long Nd:YAG laser pulse was focused over 2.22 mm diameter on the Al film. Upon absorption of the laser energy, the Al film melts and exfoliates. This process results in the launch of a pressure wave with a 1-2 ns rise-time and 16-20 ns duration towards the sample mounted on the front surface of the substrate disc ([43], [44]). Prior to the laser shot, the axis of laser beam was aligned with the center of one of the pillar groups. This configuration allowed for the stress waves propagate along the axes of each of the nanopillars and transmit into the brass plate.

Each group of pillars was shock-loaded once using laser shots of different energies. All the pillars within a group were uniformly loaded as they were located 1.5 mm from the laser heating area and within 50 μm of the stress wave propagation axis. This can be concluded based on the calculations of Lev and Argon [27], who showed that plane wave conditions are maintained over 95% of the initially stressed area at a wave propagation distance equal to the diameter of the laser heating spot.

In order to obtain the stress state in our copper sample, a state-of-the-art optical interferometer (see Figure 3.2), capable of recording fringes with 0.2 ns resolution in the single shot mode, was used to measure the free surface displacement. In prior studies, where thin film samples were subjected to tensile loads, optical interferometry was used to calculate the peak interfacial stress using a wave mechanics simulation [41]. Utilizing this setup, interfacial strengths of 0.1 to 2.5 GPa have been reported for a variety of interfacial systems, involving metals, ceramics, and polymers ([18], [20], [21], [25], [26], [41], [42], [45], [46]). In this study, it was not possible to measure the incident time-dependent stress wave profile $\sigma(t)$ generated in the glass plate during the deformation of the Cu pillars. Instead, $\sigma(t)$ was obtained in a separate experiment in which an isolated glass plate was shock-loaded under the same stress wave generation conditions (laser fluence and thicknesses of glass substrate, Al film, and waterglass layers) as those used for compression of the Cu pillars. The free surface velocity $v(t)$ of the glass plate was recorded using the optical interferometer (see Figure 3.2) and used to calculate $\sigma(t)$ by equation:

$$\sigma(t) = \frac{\rho c_o}{2}\left[v\left(t+\frac{h}{c}\right) - v\left(t-\frac{h}{c}\right)\right], \qquad (3.1)$$

where c_o (= 2289 m/s), ρ, and h are the longitudinal wave speed in the medium (glass), its density, and thickness, respectively. Details of interferometer methodology can be found in Pronin and Gupta [23], Barker and Hollenback [47], and Clifton [48]. The exact compressive stress-state inside each pillar can be determined using finite element simulations with $\sigma(t)$ as an input. Thus, local stresses obtained can be used for carrying out MD simulations [49].

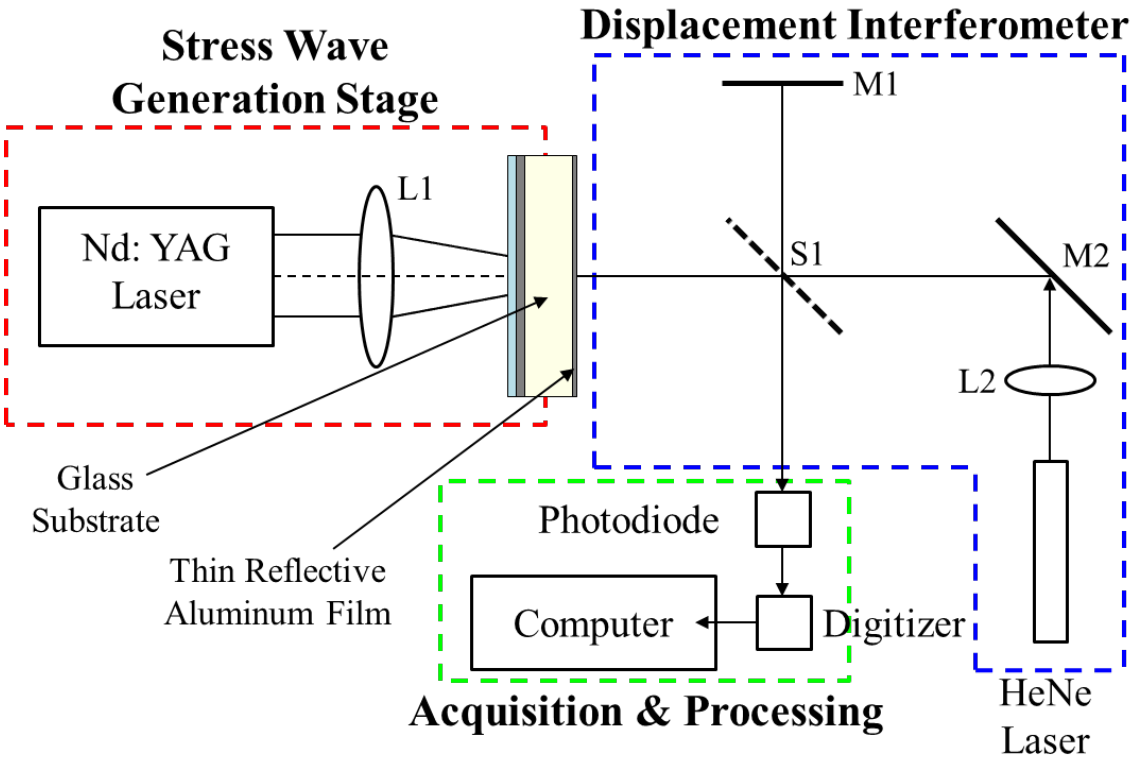

FIG. 3.2. Schematic of the laser spallation test set-up along with that of an optical interferometer used to generate and record stress waves. Adapted from [49], [50].

After shock-loading, the pillars were lifted off the substrate using FIB and mounted on TEM grids. Electron-transparent (< 100 nm) cross-sectional samples were prepared by FIB milling of the pillars at a low accelerating voltage, 5 kV. TEM, selected

area electron diffraction (SAED), scanning TEM (STEM), along with energy dispersive X-ray spectroscopy (EDS) measurements were carried out using a JEM-100CX (JEOL) TEM operated at 100 kV and a Titan (FEI) S/TEM operated at 300 kV.

3.3 Results and Conclusions

Figure 3.3a is a typical interferometric fringe record obtained at a laser fluence of 95.2 kJ/m^2 from the free surface of the isolated glass plate sample using the same stress generation conditions as those used to shock-load Cu pillars. Figures 3.3b and 3.3c show the corresponding velocity and stress wave profiles, $u(t)$ and $\sigma(t)$, respectively obtained from this fringe record, by using the well-established procedures of interferometry mentioned earlier. Using this stress wave profile as input, finite element simulations of the wave propagation under identical experimental conditions yielded a maximum compressive stress of 1 GPa and peak strain rate of 3 x 10^7 s^{-1} inside the Cu pillars (with percent errors of ± 5%). In the following sections, we focus on the effect of shock-loading on morphologies and microstructures of the pillars.

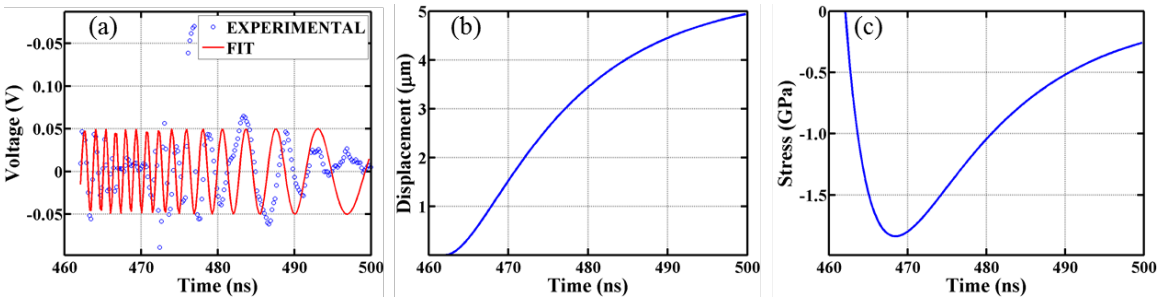

FIG. 3.3. (a) Fringe record obtained at laser fluence 95.2 kJ/m^2 using the interferometry shown in Fig. 3.2b. **(b)** The reduced displacement profile derived from (a). **(c)** The stress wave profile derived from (b).

In order to investigate the effect of shock-loading on surface morphologies of the Cu pillars, each of the pillar groups were subjected to a different laser fluence and the resulting morphologies were examined using SEM. Figure 4 is a representative panel of SEM images acquired from three different pillars each belonging to a separate group on the same Cu(001) sample. The images (Figures 3.4a-c) in the top row show a reference pillar that was not shock-loaded. The middle (Figures 3.4d-f) and bottom (Figures 3.4g-i) rows show SEM images of two different Cu pillars that were shock-loaded under uniaxial compression by stress waves generated at laser fluence of 39.5 kJ/m^2 and 93.4 kJ/m^2, respectively. The time t = 0 in the panel, i.e. the left column images (Figures 3.4a, 3.4d, and 3.4g), is defined arbitrarily and corresponds to the pillar morphologies prior to mounting the Cu sample for shock-loading experiments. Following loading, the sample containing these three different pillars was submerged in isopropyl alcohol (IPA) for ten minutes. It is assumed that IPA helps dissolve any oil that may be present on the sample, which was surrounded by an oil bath used as a coupling medium during loading. The sample was subsequently removed from the IPA solution and left air-exposed for 12 h at room temperature. SEM images were acquired from this sample and are shown in the middle column (see Figures 3.4b, 3.4e, and 3.4h). When compared to the reference pillar (Figure 4b), note the changes in surface morphologies of the shock-loaded pillars in Figures 3.4e and 3.4h. On both the shock-loaded pillars, the images reveal: (1) increased surface roughness; (2) spalled regions near the tops of the pillars likely due to loading by the shock wave; and (3) an outward growth of thin films with highest coverage around the base of the pillar.

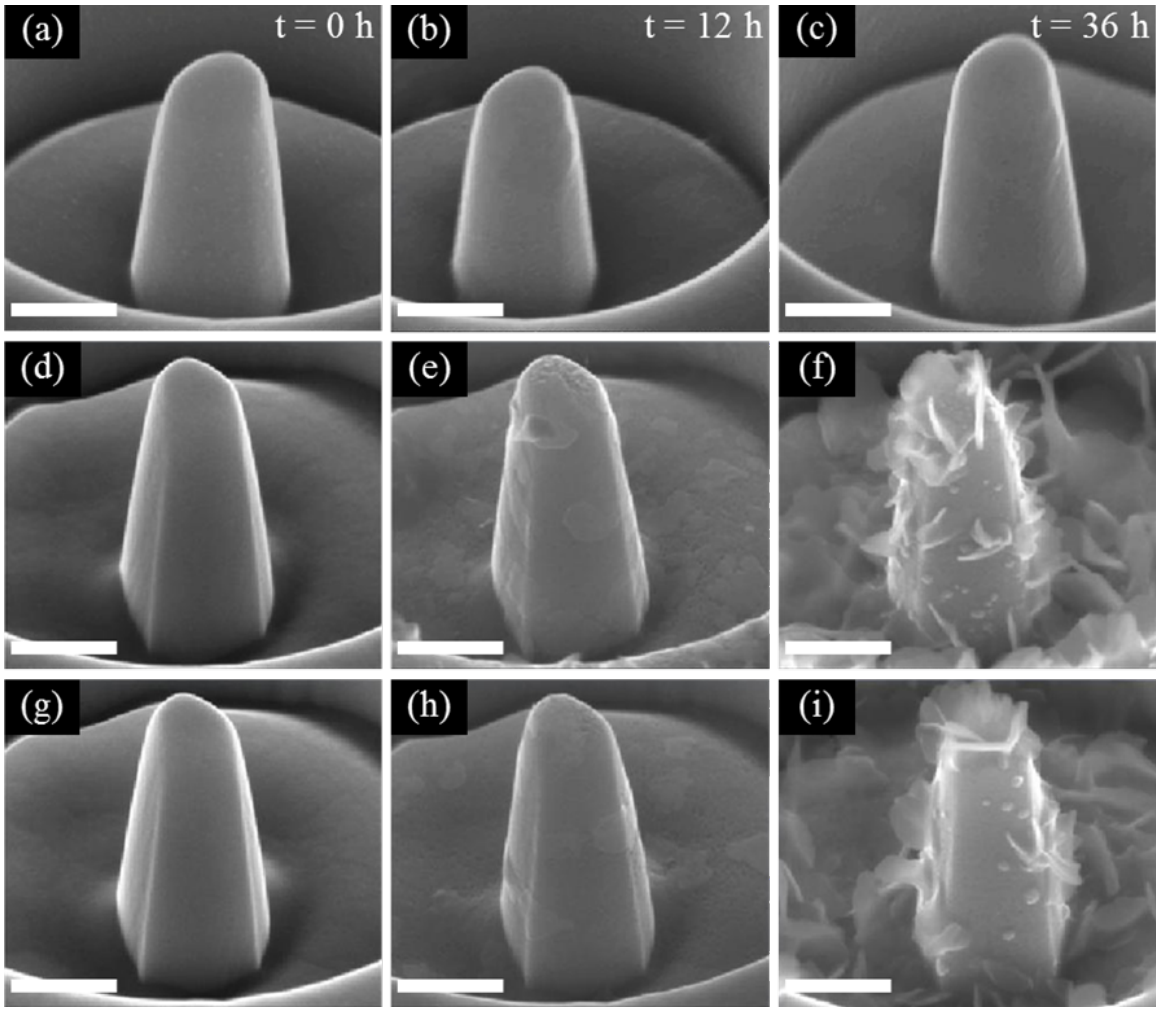

FIG. 3.4. Scanning electron microscopy (SEM) images of Cu pillars on a Cu(001) substrate **(a,d,g)** prepared via focused ion beam (FIB) milling prior to testing. **(b, e, h)** and **(c, f, i)** are obtained 12 and 36 h, respectively after loading. The images in the top, middle, and bottom rows show three different pillars tested at laser fluence of 0, 39.5, and 93.4 kJ/m^2, respectively. The scale bar in all the images is 400 nm.

Later, the same sample was submerged in IPA solution for additional 3 h, removed, and air-dried for 18 h at room temperature. Subsequently, SEM images were acquired from this sample and are shown in the right column (see Figures 3.4c, 3.4f, and 3.4i). The time t = 36 h indicated in Figure 3.4 is the total time elapsed between the loading of the sample and the acquisition of SEM images shown in the last column. The

images reveal extensive growth of thin films around the surface of shock-loaded pillars. In contrast, the surface morphology of the reference pillar changed little over the 36 h. Given that all the pillars were situated on the same Cu sample, submerged in the same set of solutions, and for the same duration, the observed film growth on the shock-loaded pillars strongly suggests that shock-loading enhanced their surface reactivities.

In order to identify the chemical composition of these films formed around the Cu pillars, EDS, to obtain the elemental constituents, and SAED, to determine the compound, were used. Figure 3.5a is a typical STEM image of the pillar shown in Figure 3.4f, shock-loaded at 39.5 kJ/m^2. Point mode was acquired from the regions surrounding the pillar. The associated plot below Figure 3.5a shows the characteristic X-ray signals from the elements (C, O, Cu, Pt, Ga and S) at the points labeled 1-3 in Figure 3.5a. The EDS data from spot 2 in Figure 3.5a, i.e. from the thin film, reveal relatively high concentrations of carbon and oxygen. (The Pt and Ga signals are due to FIB milling and S is likely due to the oil bath.) The plot associated with Figure 3.5a shows strong signal from the elements (Cu, C, and O) in spot 2 from Figure 3.5a. Based upon these results, we suggest that the thin films observed around the pillars are likely to be copper oxides or copper carbonate. Figure 3.5b is a representative SAED pattern obtained from the film at point 2 in Figure 3.5a. The observed diffraction rings indicate that the film is polycrystalline. From the measured interplanar spacings, we determined the crystal structure to be cubic copper(I) oxide (JCPDS file No. 5-667). We attribute the observed thin film growth to the exposure of fresh Cu surfaces resulting from surface material spallation and the formation of surface steps and nanoscale facets via elimination of the dislocations from the bulk. This film growth via shock-loading is possible throughout the

entire bulk but is more likely to occur where the surface area to volume ratio is high, as is found with the pillars. While the surface spalls are visible in the SEM images, the presence of surface steps and/or facets could not be confirmed. However, in the following section, we provide evidence for shock-induced dislocation motion, a strong indication of mechanical annealing.

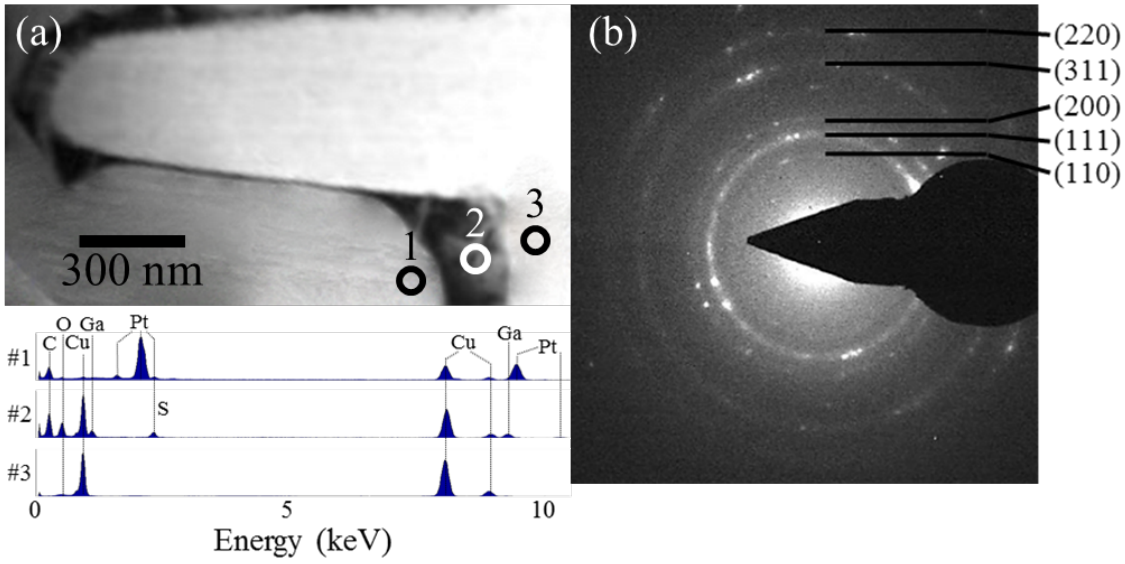

FIG. 3.5. (a) Scanning transmission electron microscopy (STEM) image of the pillar shown in Fig. 3.4f loaded at 39.5 kJ/m^2. Elemental composition spectrum, as determined using energy dispersive spectroscopy (EDS), at the points 1-3 are provided in the graphs below. **(b)** Selected area electron diffraction (SAED) pattern acquired from the region labeled 2 in (a).

Figures 3.6a-c are typical bright-field TEM images of a reference pillar that was not shock-loaded (Figure 6a) and two pillars that were independently loaded with laser fluence of 39.5 kJ/m^2 (Figure 3.6b) and 93.4 kJ/m^2 (Figure 3.6c), respectively. The SAED pattern in Figure 3.6d was obtained from the pillar in Figure 3.6a and is identical to the diffraction (not shown) from the shock-loaded pillars. That is, in our experiments, shock-

loading did not affect the crystallinity of the pillars. All the TEM images show darker contrast cellular structures within the pillars. A majority of these features are dislocations while other features are Ga clusters which are common artifacts due to the FIB fabrication processes utilized [51]. The high density of dislocations observed in the bulk of the reference pillar (Figure 3.6a) could be attributed to the quality of the Cu crystal or defects from mechanical polishing of the Cu single crystal substrate's surface [52]. The dark contrast present around the surface of the pillars is due to the FIB milling process used to fabricate the pillars, indicated by the depth of the damage [51]. Since all the pillars were milled out of the same Cu(001) crystal and used the same FIB parameters for both pillar and TEM sample fabrication, it is expected that the density and spatial distribution of radiation damage from FIB were similar in all the pillars. While the microstructures of shock-loaded pillars shown in Figures 3.6b and 3.6c are qualitatively similar to that of the as-prepared pillar, it is possible that shock-loading can increase or decrease the dislocation density by nucleation of new dislocations or by removal of dislocations by motion from the bulk to the surface, respectively. The latter process results in the formation of new surface steps and/or nanoscale facets, which could explain the enhanced surface reactivity of the shock-loaded pillars (Figures 3.4f and 3.4i).

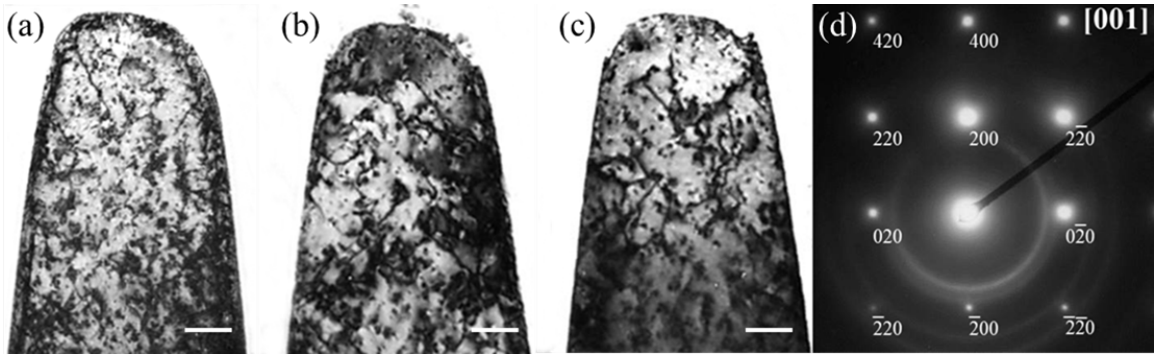

FIG. 3.6. Bright-field transmission electron microscopy (TEM) images of three different Cu(001) pillars acquired **(a)** as-prepared and after shock-loading using laser fluence of **(b)** 39.5 kJ/m^2 and **(c)** 93.4 kJ/m^2. All pillars have [001] as their main axis and the samples were oriented along the [001] zone axis during TEM analysis. The scale bars in all images is 100 nm. **(d)** Selected area electron diffraction (SAED) pattern of the pillar shown in (a). The ring pattern observed in (d) is due to Pt thin film deposited as a protective layer prior to TEM sample preparation via focused ion beam (FIB) milling.

To quantitatively assess the effect of shock loading on the microstructure of the pillars, dislocation densities and orientations were determined. For consistency, all the TEM images analyzed were acquired under identical imaging conditions, i.e. bright-field images of the pillars were taken in exact [001] zone axis. And, since the TEM samples were prepared using FIB, those dislocations near the pillar's surface were ignored. From the TEM images the average dislocation densities were calculated. The calculated dislocation density decreased from 7.9 x 10^{14} m^{-2} in the reference pillar to 3.1 x 10^{14} m^{-2} and 2.1 x 10^{14} m^{-2} in the pillars loaded at 39.5 kJ/m^2 and 93.4 kJ/m^2, respectively. The decrease in dislocation density is most likely a result of dislocation motion out of the bulk.

In order to further explore the influence of shock-loading on dislocation density in the pillars, the orientations of projected dislocations visible in the bright-field TEM images (Figures 3.6a-c) were measured with respect to the major axis of the pillars, [100]. Since detailed characterization of all of the dislocations present in the pillars is a non-trivial task requiring elaborate electron microscopy, analyses were limited to measuring *relative* changes in orientations of only those dislocations that are visible under specific imaging conditions. In particular, dislocations with ½[110] Burgers vectors are of interest, which are common in *FCC* crystals such as Cu [53]. When the [100]-

oriented Cu pillars are viewed along the [001] zone axis in the TEM, the projections of these dislocation lines are expected to appear at 45° with respect to the pillar axis, provided the deviation parameter is small [54]. In the reference pillar, the average angle subtended by the dislocations is 46.0 ± 5.5°. In comparison, the angles are 41.5 ± 8.6° and 43.2 ± 13.0° in samples loaded with stress waves generated at laser fluence of 39.5 and 93.4 kJ/m^2, respectively. Each of these values was determined from 14 dislocation lines observed in each of the pillars. While the average angles are nearly the same within the measurement uncertainties, note the increase in deviations in angles from 5.5° in the reference pillar to 8.6° and 13.0° in the shock-loaded samples. That is, the orientational spread of dislocations increases with increasing laser fluence. These results provide further evidence in support of the hypothesis that shock-loading induces motion of the dislocations and/or formation of new dislocations.

The data presented above indicate that the density and orientation of dislocations depend on the laser fluence. These results can be explained as follows. The stress waves generated within the pillars due to the laser shot are transient and over a short duration (~ 20 ns). Therefore, the amplitude of the stress and strain rate change continuously with a maximum stress of 1 GPa and strain rate of 3 x 10^7 s^{-1} for a laser fluence of 95.2 kJ/m^2. At such high strain rates and short time scales over which the pillars were loaded at a given stress value, motion of pre-existing dislocations is limited because of the increase in the local shear strength of the slip systems. When dislocation motion does occur, it is limited as they are eventually pinned by their neighbors and additional stress is required for their continued motion. This dislocation pinning can also lead to nucleation of new

dislocations. Those dislocations present near the surface, however, are likely to escape leaving behind surface steps and nanoscale facets. This is consistent with the TEM observations of a relatively low density of dislocations within the top 30 nm of the shock-loaded pillars. Consequently, dislocation motion is expected to be higher at higher laser fluence resulting in the observed lower dislocation density and wider orientational spread.

These results led to work done by Seif *et al* [13]. In this work by Seif, molecular dynamics (MD) simulations were employed to explore the results of this work. Seif *et al* determined that size has a significant effect upon the stress state necessary to obtain partial dislocations within a copper sample. Previous literature has provided a stress state of 30-40 GPa to obtain partial dislocations in Cu [9], [12], [55]–[58]. With the limited geometry of a Cu nanopillar, it was determined that a stress state of 1-1.5 GPa was necessary to nucleate partial dislocations in a copper nanopillar. This is more than an order of magnitude lower that what had been previously observed and confirms the results of the Cu nanopillar experiments.

In summary, we demonstrated an experimental approach for ultra-high strain rate, uniaxial compression of metal pillars using laser-generated shock waves. FIB-prepared single-crystalline Cu(001) nanopillars were used as model materials. Electron microscopy was utilized to investigate the effects of shock-loading on surface morphology and bulk microstructure of the pillars. We found that shock-loading enhances surface chemical reactivity via a combination of surface spallation and bulk dislocation motion resulting in exposure of pristine surfaces and the formation of surface steps and nanoscale facets. Our results indicate that materials subjected to ultra-high strain rate loading undergo

deformation and the underlying mechanisms can be different from those expected at conventional strain rates. The test procedures employed in our study are general and applicable to other crystalline materials. The sample geometry and the dimensions facilitated direct comparison of experimental results with molecular dynamics and finite element method simulations, which proved to provide valuable insights into the underlying deformation mechanisms.

4 Aluminum Nanopillars Loaded at Low Laser Fluence

4.1 Introduction

In the present work, we report on fabrication and shock-loading of 100-oriented, single-crystalline, Al nanopillars, with pillar axes aligned with the wave propagation (compression) direction. To this purpose, we developed an apparatus and related test procedures for the compression of Al nanopillars at pressures and strain rates greater than 1 GPa and 10^7 s^{-1}, respectively using laser-generated stress waves of 1-2 ns rise-times and 16-20 ns total duration. Deformation mechanisms are identified by transmission electron microscopy (TEM) characterization of the residual microstructure in shock-loaded samples. The experimental approach presented here is general and applicable to shock-loading of other materials. The experimentally-measured stress wave profiles and the sample microstructures can be used as input for large-scale MD and finite element simulations to help elucidate the underlying microscopic dislocation dynamics and the atomistics of deformation mechanisms.

4.2 Experimental Procedure

All of our experiments were carried out using single-crystalline Al(001) pillars in the Laser Spallation Facility, developed previously to measure tensile strengths of interfaces [42]. Schematics of the experimental setup are shown in Figures 4.1 and 4.2. The Al pillars (~ 1 μm tall and 0.65 μm in diameter) spanning approximately a 10 μm diameter were prepared out of Al(001) substrates (10 mm × 10 mm × 0.5 mm purchased from MTI Corporation, Richmond, CA). Pillar dimensions were chosen so that the

morphologies of the as-prepared and shock-loaded pillars could be determined using electron microscopy. Four groups of 6 identical pillars were prepared in a Nova 600 Dual Beam focused-ion-beam/scanning electron microscope (FIB/SEM) system using gallium ions at 0.5 nA current and an accelerating voltage of 30 kV. Each of the four groups was separated from its neighbors by at least 5 mm so that each group of pillars could be independently loaded by the shock wave. This enabled us to carry out multiple tests on the same substrate.

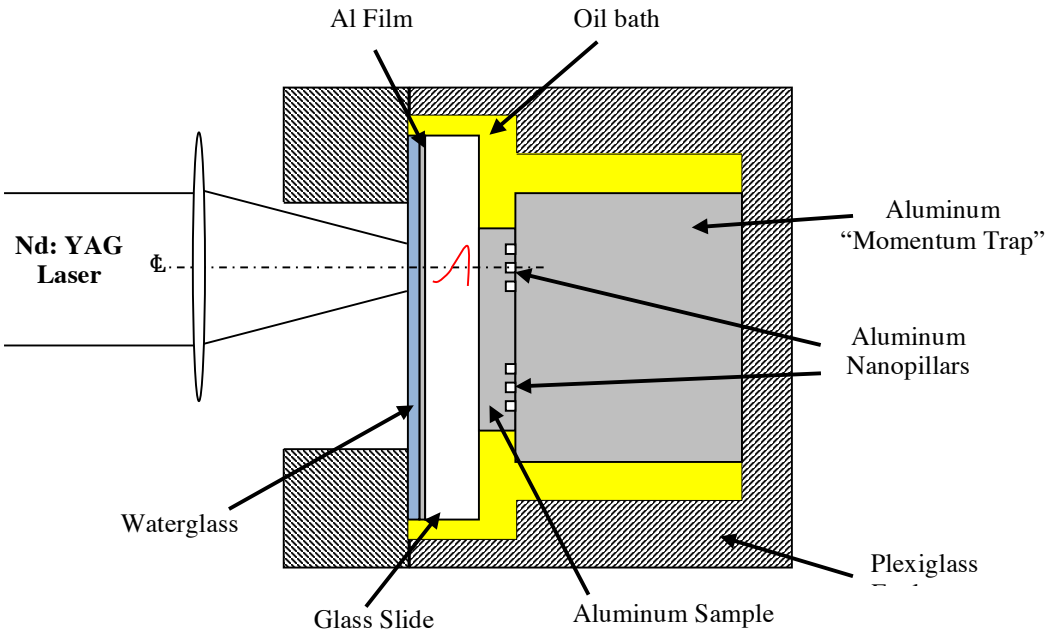

FIG. 4.1. Cross-sectional view of the experimental setup, showing two sets of nanopillars on an aluminum sample, oriented such that the axes of the pillars are aligned with the stress wave propagation direction.

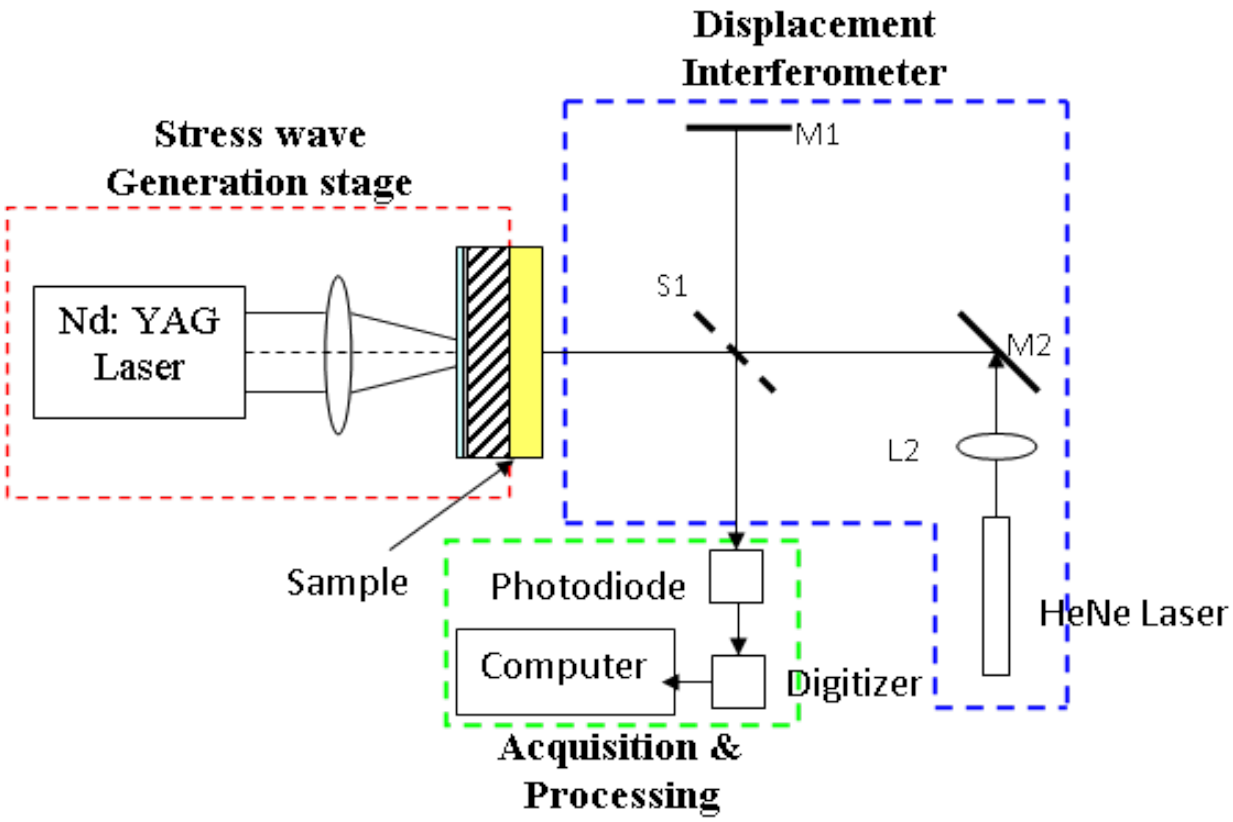

FIG. 4.2. Schematic of the laser spallation test set-up along with that of an optical interferometer used to generate and record stress waves. Adapted from Youssef and Gupta [49] and Youssef [59].

In a typical experiment, the Al sample was sandwiched between a 1-mm-thick glass substrate and a 9-mm-thick aluminum plate as shown in Figure 4.1. The back surface of the glass substrate was coated with a 0.5-μm-thick, laser absorbing Al film, which was constrained from the top by a transparent 20-50 μm thick layer of waterglass. The thicknesses of the Al film and the waterglass layer were optimized by Yuan *et al.* [42] and Gupta *et al.* [20] to generate stress waves with the fastest rise times (< 1 ns) and shortest duration so that Al pillars could be loaded under extreme conditions. Aluminum was chosen to minimize the wave reflection effects in the aluminum nanopillars and

maintain a uniaxial compressive state of stress in the pillars since it has a minimal acoustic impedance mismatch with the Al. Moreover, in order to preserve the deformation caused by the incoming stress wave, the aluminum plate was made very thick to geometrically disperse the waves and therefore decrease the possibility of any reloading of the pillars by the reflected waves. The glass substrate, aluminum sample, and the aluminum plate assembly was mechanically joined and sandwiched between two plexiglass plates and submerged in an oil bath to ensure proper coupling and continuity between all the interfaces so that stress waves could transmit across them. A window was cut in the plexiglass plate to allow access to the YAG laser pulse, as shown in Figure 4.1.

In this setup, a nominal 8 ns long Nd:YAG laser pulse was focused over 2.22 mm diameter on the Al film. Upon absorption of the laser energy, the Al film melts and exfoliates. This process results in the launch of a pressure wave with a 1-2 ns rise-time and 16-20 ns duration towards the sample mounted on the front surface of the substrate disc [43], [44]. Prior to the laser shot, the axis of laser beam was aligned with the center of one of the pillar groups. This configuration allowed for the stress waves propagate along the axes of each of the nanopillars and transmit into the aluminum plate.

Each group of pillars was shock-loaded once using laser shots of different energies. All the pillars within a group were uniformly loaded as they were located 1.5 mm from the laser heating area and within 50 μm of the stress wave propagation axis. This can be concluded based on the calculations of Lev and Argon [27] who showed that

plane wave conditions are maintained over 95% of the initially stressed area at a wave propagation distance equal to the diameter of the laser heating spot.

In order to obtain the stress state in our aluminum sample, a state-of-the-art optical interferometer (see Figure 4.2), capable of recording fringes with 0.2 ns resolution in the single shot mode, was used to measure the free surface displacement. In prior studies, where thin film samples were subjected to tensile loads, optical interferometry was used to calculate the peak interfacial stress using a wave mechanics simulation [41]. Utilizing this setup, interfacial strengths of 0.1 to 2.5 GPa have been reported for a variety of interfacial systems, involving metals, ceramics, and polymers ([18], [20], [21], [25], [26], [41], [42], [45], [46])). In this study, it was not possible to measure the incident time-dependent stress wave profile $\sigma(t)$ generated in the glass plate during the deformation of the Al pillars. Instead, $\sigma(t)$ was obtained in a separate experiment in which an isolated glass plate was shock-loaded under the same stress wave generation conditions (laser fluence and thicknesses of glass substrate, Al film, and waterglass layers) as those used for compression of the Al pillars. The free surface velocity $v(t)$ of the glass plate was recorded using the optical interferometer (see Figure 2) and used to calculate $\sigma(t)$ by equation:

$$\sigma(t) = \frac{\rho c_o}{2}\left[v\left(t + \frac{h}{c}\right) - v\left(t - \frac{h}{c}\right)\right], \tag{4.1}$$

where c_o (= 2289 m/s), ρ, and h are the longitudinal wave speed in the medium (glass), its density, and thickness, respectively. Details of interferometer methodology can be found in Pronin and Gupta [23], Barker and Hollenback [47], and Clifton [48]. The exact

compressive stress-state inside each pillar can be determined using finite element simulations with $\sigma(t)$ as an input. Thus, local stresses obtained can be used for carrying out MD simulations [49].

After shock-loading, the pillars were lifted off the substrate using FIB and mounted on TEM grids. Electron-transparent (< 100 nm) cross-sectional samples were prepared by FIB milling of the pillars at a low accelerating voltage, 5 kV. TEM measurements were carried out using a Titan (FEI) S/TEM operated at 300 kV.

4.3 Results and Conclusions

In order to investigate the effect of shock-loading on surface morphologies of the Al pillars, each of the pillar groups was subjected to a different laser fluence and the resulting morphologies were examined using SEM. Figure 4.3 is a representative panel of SEM images acquired from two different pillars each belonging to a separate group on the same Al(001) sample. The top (Figures 4.3a-c) and bottom (Figures 4.3d-f) rows show SEM images of two different Al pillars that were shock-loaded under uniaxial compression by stress waves generated at laser fluence of 42.1 kJ/m^2 and 99.2 kJ/m^2, respectively. The time t = 0 in the panel, i.e. the left column images (Figures 4.3a and 4.3d), is defined arbitrarily and corresponds to the pillar morphologies prior to mounting the Al sample for shock-loading experiments. Following loading, the sample containing these pillars was submerged in isopropyl alcohol (IPA) for ten minutes. It is assumed that IPA helps dissolve any oil that may be present on the sample, which was surrounded by an oil bath used as a coupling medium during loading. The sample was subsequently

removed from the IPA solution and left air-exposed for 4 h at room temperature. SEM images were acquired from this sample and are shown in the middle column (see Figures 4.3b and 4.3e). When compared to the loaded at 42.1 kJ/m^2 pillar (Figure 3b), note the changes in surface morphologies of the 99.2 kJ/m^2 shock-loaded pillar in Figure 3e. For the higher fluence the shock-loaded pillar, the images reveal a growth of a carbon rich region surrounding the pillar.

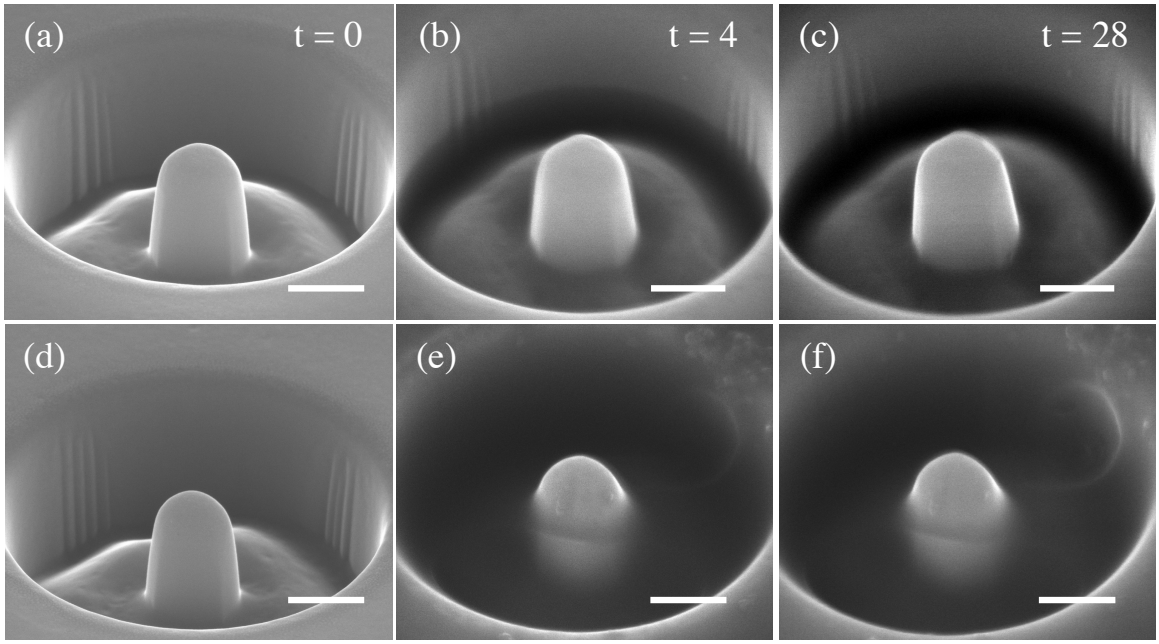

FIG. 4.3. Scanning electron microscopy (SEM) images of Cu pillars on an Al(001) substrate **(a,d)** prepared via focused ion beam (FIB) milling prior to testing. **(b, e)** and **(c, f)** are obtained 4 and 28 h, respectively after loading. The images in the top and bottom rows show two different pillars tested at laser fluence of 44.2 and 99.2 kJ/m^2, respectively. The scale bar in all the images is 500 nm.

Later, the same sample was submerged in IPA solution for additional 3 h, removed, and air-dried for 19 h at room temperature. Subsequently, SEM images were acquired from this sample and are shown in the right column (see Figures 4.3c and 4.3f).

The time t = 28 h indicated in Figure 3 is the total time elapsed between the loading of the sample and the acquisition of SEM images shown in the last column. The images reveal extensive growth of a dark region in the well surrounding the pillars. In contrast, the surface morphology of the reference pillar changed little over the 28 h. Given that all the pillars were situated on the same Al sample, submerged in the same set of solutions, and for the same duration, the observed dark region growth on the shock-loaded pillars strongly suggests that shock-loading enhanced their surface reactivities.

In order to identify the chemical composition of these films formed around the Al pillars, SAED in the TEM was used. Unfortunately, the SAED was not taken for this sample, but the growth appears to be identical to results found in copper nanobenches described in Chapter 5. In the copper nanobenches experiments, it was determined that the growth was a carbon-rich region of Cliftonite (JCPDS No. 34-567). We attribute the observed carbon growth to the exposure of fresh Al surfaces resulting from surface material spallation and the formation of surface steps and nanoscale facets via mechanical annealing of the dislocations. In the following section, we provide evidence for dislocation nucleation in the aluminum sample.

Figures 4.4a-c are typical bright-field TEM images of a reference pillar that was not shock-loaded (Figure 4.4a) and two pillars that were independently loaded with laser fluence of 42.1 kJ/m^2 (Figure 4.4b) and 99.2 kJ/m^2 (Figure 4.4c), respectively. The selected area electron diffraction (SAED) pattern in Figure 4.4d is obtained from the pillar in Figure 4a and is identical to the diffraction (not shown) from the shock-loaded

pillars. That is, in our experiments, shock-loading did not affect the crystallinity of the pillars. All the TEM images show darker contrast cellular structures within the pillars. A majority of these features are dislocations. It can be observed that compared to previous results found via Youssef *et al.* [60] for copper nanopillars, these samples are fairly "clean," not plagued by poor crystal quality nor FIB radiational damage. Therefore, with minimal radiational damage and lower dislocation densities, we can clearly observe dislocation nucleation in our samples. It is clear that when observing the Figure 4a compared to Figures 4b and 4c that there are dimensional differences between them. The procedure that the reference went through did vary from the two loaded pillars in just being prepared at a different time, which resulted in the milling of a different shape. Regardless, that difference should not affect the internal structure of the nanopillars. This is made clear by observing the localized damage found on the reference pillar in Figure 4a. Even though there are localized regions of likely point defect clusters due to the gallium implantation, there do not appear to be many dislocations present. Then when the reference pillar is compared to the pillars that were shock-loaded, it is clear that there are dislocations that are formed due to the treatment of the shock-loaded pillars.

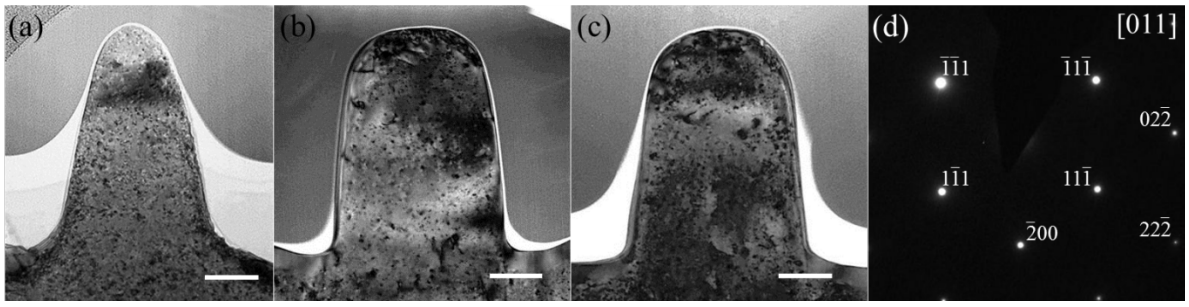

FIG. 4.4. Bright-field transmission electron microscopy (TEM) images of three different Al(001) pillars acquired **(a)** as-prepared and after shock-loading using laser fluence of **(b)** 44.2 kJ/m^2 and **(c)** 99.2 kJ/m^2. All pillars have [001] as their main axis and the samples

were oriented along the [011] zone axis during TEM analysis. The scale bars in all images is 200 nm. **(d)** Selected area electron diffraction (SAED) pattern of the pillar shown in (a).

Next, when comparing the TEM images of the pillars loaded at 42.1 kJ/m^2 (Figure 4.4b) and 99.2 kJ/m^2 (Figure 4.4c), there are fundamental differences in the locations of these dislocations. It appears from these micrographs that in Figures 4.4b and 4.4c there is nucleation of dislocations and movement of these dislocations in the direction of the wave propagation, which is toward the top of the pillar. The dislocations appear to be pinned near the top of the pillar and likely require excess energy to exceed this barrier. From the comparison of the two TEM images of pillars loaded at different energies, it is evident that there appears to be more dislocations that are pinned near the top of the pillar for the pillar loaded at the higher energy fluence. This very well could be evidence that the higher the energy fluence, the more dislocations that are nucleated within the pillar.

The data presented above indicate that the density of dislocations depend on the laser fluence. These results can be explained as follows. The stress waves generated within the pillars due to the laser shot are transient and over a short duration (~ 20 ns). Therefore, the amplitude of the stress and strain rate change continuously with a maximum stress of 1 GPa and strain rate of 3 x 10^7 s^{-1} for a laser fluence of 95.2 kJ/m^2. At such high strain rates and short time scales over which the pillars were loaded at a given stress value, motion of pre-existing and nucleated dislocations is limited because of the increase in the local shear strength of the slip systems. When dislocation motion does occur, it is limited as they are eventually pinned by their neighbors and additional stress is required for their continued motion. This dislocation pinning can also lead to

nucleation of new dislocations. Consequently, at higher laser fluence, dislocation motion and dislocation density are both expected to be greater.

5 Copper Nanobenches Loaded Transversely at Low Laser Fluence

5.1 Introduction

In the present work, we report on fabrication and shock-loading of 100-oriented, single-crystalline, Cu nanobenches, with bench axes aligned with the wave propagation (compression) direction. To this purpose, we developed an apparatus and related test procedures for the compression of Cu nanobenches at pressures and strain rates greater than 1 GPa and 10^7 s^{-1}, respectively using laser-generated stress waves of 1-2 ns rise-times and 16-20 ns total duration. Deformation mechanisms are identified by transmission electron microscopy (TEM) characterization of the residual microstructure in shock-loaded samples. The experimental approach presented here is general and applicable to shock-loading of other materials. The experimentally-measured stress wave profiles and the sample microstructures can be used as input for large-scale MD and finite element simulations to help elucidate the underlying microscopic dislocation dynamics and the atomistics of deformation mechanisms.

5.2 Experimental Procedure

All of our experiments were carried out using single-crystalline Cu(001) benches in the Laser Spallation Facility, developed previously to measure tensile strengths of interfaces [41].. Schematics of the experimental setup are shown in Figures 5.1 and 5.2. The Cu benches (~ 1.20 μm long and 0.5 μm wide) spanning approximately a 10 μm diameter were prepared out of Cu(001) substrates (10 mm × 10 mm × 0.5 mm purchased

from MTI Corporation, Richmond, CA). Bench dimensions were chosen so that the morphologies of the as-prepared and shock-loaded benches could be determined using electron microscopy. Four groups of 6 identical benches were prepared in a Nova 600 Dual Beam focused-ion-beam/scanning electron microscope (FIB/SEM) system using gallium ions at 0.5 nA current and an accelerating voltage of 30 kV. Each of the four groups was separated from its neighbors by at least 5 mm so that each group of benches could be independently loaded by the shock wave. This enabled us to carry out multiple tests on the same substrate.

In a typical experiment, the Cu sample was sandwiched between a 1-mm-thick glass substrate and a 9-mm-thick brass plate as shown in Figure 5.1. The back surface of the glass substrate was coated with a 0.5-μm-thick, laser absorbing Al film, which was constrained from the top by a transparent 20-50 μm thick layer of waterglass. The thicknesses of the Al and the waterglass layers were optimized by Yuan *et al.* [42] and Gupta *et al.* [20] to generate stress waves with the fastest rise times (< 1 ns) and shortest duration so that Cu benches could be loaded under extreme conditions. Brass was chosen to minimize the wave reflection effects and maintain a uniaxial compressive state of stress in the copper nanobenches since it has a low acoustic impedance mismatch with the Cu substrate (3.7×10^7 Ns/m^3 for brass vs. 4.1×10^7 Ns/m^3 for Cu). Moreover, in order to preserve the deformation caused by the incoming stress wave, the brass plate was made very thick to geometrically disperse the waves and therefore decrease the possibility of any reloading of the benches by the reflected waves. The glass substrate, copper sample, and the brass plate assembly were mechanically joined and sandwiched between two

plexiglass plates and submerged in an oil bath to ensure proper coupling and continuity between all the interfaces so that stress waves could transmit across them. A window was cut in the plexiglass plate to allow access to the YAG laser pulse, as shown in Figure 5.1.

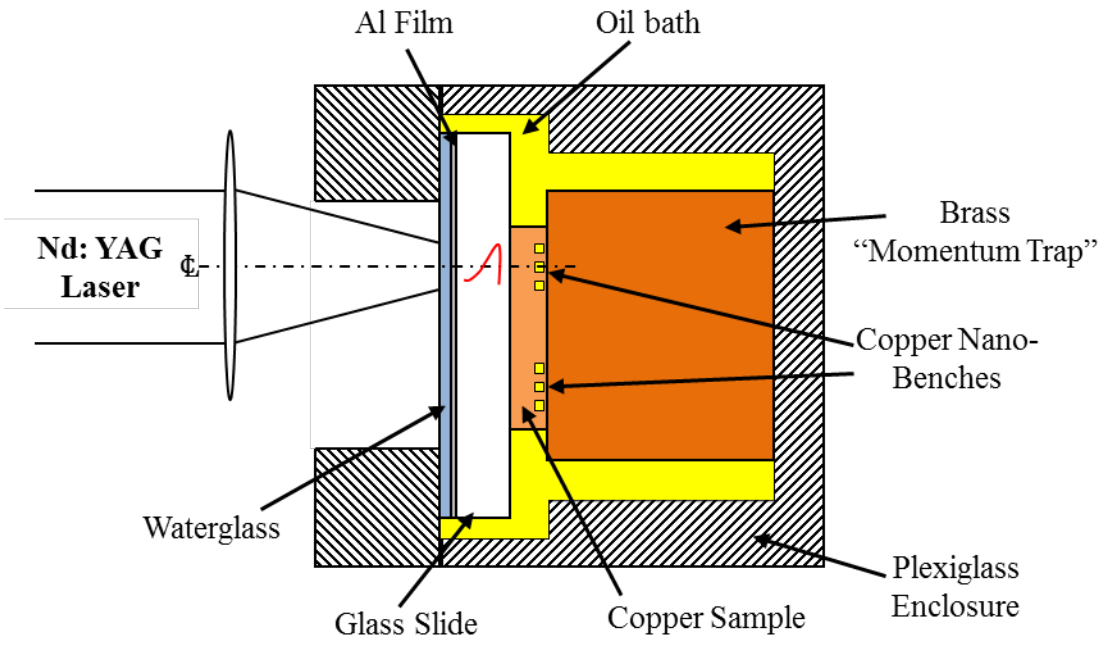

FIG. 5.1. Cross-sectional view of the experimental setup, showing two sets of nanobenches on a copper sample, oriented such that the axes of the benches are aligned with the stress wave propagation direction.

In this setup, a nominal 8 ns long Nd:YAG laser pulse was focused over 2.22 mm diameter on the Al film. Upon absorption of the laser energy, the Al film melts and exfoliates. This process results in the launch of a pressure wave with a 1-2 ns rise-time and 16-20 ns duration towards the sample mounted on the front surface of the substrate disc [43], [44]. Prior to the laser shot, the axis of laser beam was aligned with the center of one of the bench groups. This configuration allowed for the stress waves propagate orthogonal to the lengths of each of the nanobenches and transmit into the brass plate.

Each group of benches was shock-loaded once using laser shots of different energies. All the benches within a group were uniformly loaded as they were located 1.5 mm from the laser heating area and within 50 μm of the stress wave propagation axis. This can be concluded based on the calculations of Lev and Argon [27] who showed that plane wave conditions are maintained over 95% of the initially stressed area at a wave propagation distance equal to the diameter of the laser heating spot.

In order to obtain the stress state in our copper sample, a state-of-the-art optical interferometer (see Figure 5.2), capable of recording fringes with 0.2 ns resolution in the single shot mode, was used to measure the free surface displacement. In prior studies, where thin film samples were subjected to tensile loads, optical interferometry was used to calculate the peak interfacial stress using a wave mechanics simulation [41]. Utilizing this setup, interfacial strengths of 0.1 to 2.5 GPa have been reported for a variety of interfacial systems, involving metals, ceramics, and polymers ([18], [20], [21], [25], [26], [41], [42], [45], [46]). In this study, it was not possible to measure the incident time-dependent stress wave profile $\sigma(t)$ generated in the glass plate during the deformation of the Cu benches. Instead, $\sigma(t)$ was obtained in a separate experiment in which an isolated glass plate was shock-loaded under the same stress wave generation conditions (laser fluence and thicknesses of glass substrate, Al film, and waterglass layers) as those used for compression of the Cu benches. The free surface velocity $v(t)$ of the glass plate was recorded using the optical interferometer (see Figure 2) and used to calculate $\sigma(t)$ by equation:

$$\sigma(t) = \frac{\rho c_o}{2}\left[v\left(t + \frac{h}{c}\right) - v\left(t - \frac{h}{c}\right)\right], \tag{5.1}$$

where c_o (= 2289 m/s), ρ, and h are the longitudinal wave speed in the medium (glass), its density, and thickness, respectively. Details of interferometer methodology can be found in Pronin and Gupta [23], Barker and Hollenback [47], and Clifton [48]. The exact compressive stress-state inside each bench can be determined using finite element simulations with $\sigma(t)$ as an input. Thus, local stresses obtained can be used for carrying out MD simulations [49].

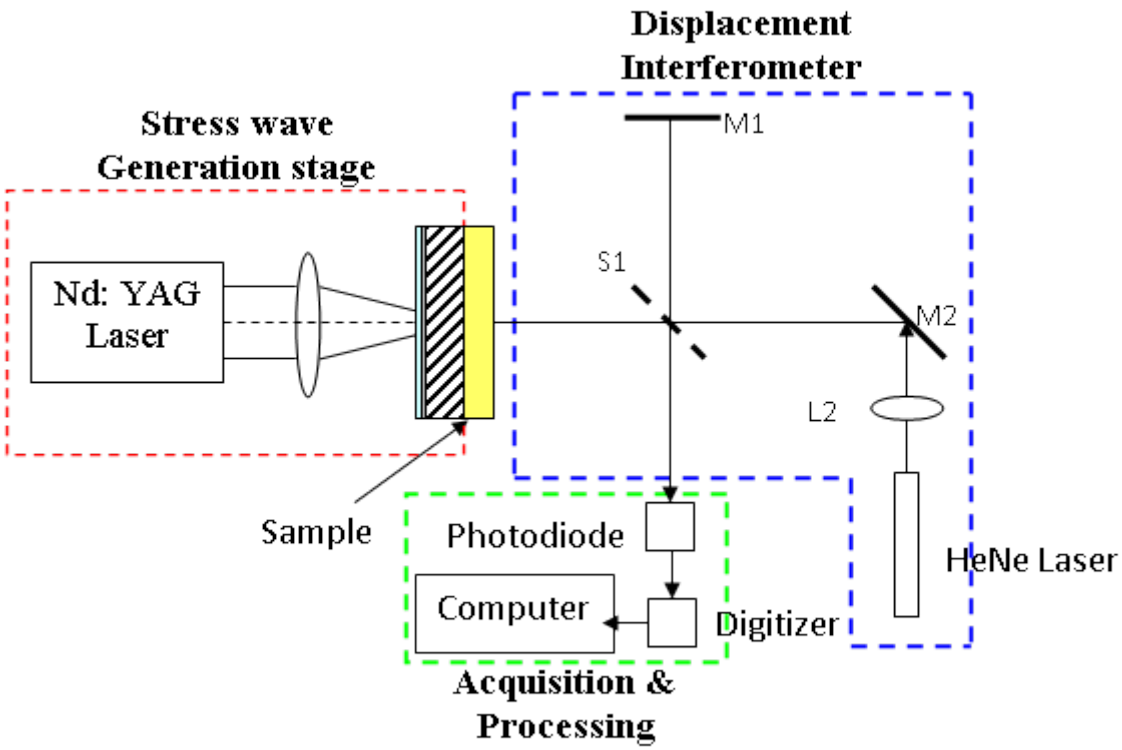

FIG. 5.2. Schematic of the laser spallation test set-up along with that of an optical interferometer used to generate and record stress waves. Adapted from [49], [50].

After shock-loading, the benches were lifted off the substrate using FIB and mounted on TEM grids. This was done in two different manners for both the reference benches and the shock-loaded benches. The first was the cross-section of the length of the bench (Figures 3a and 3b) and the second was the cross-section through the middle of the pillar, orthogonal to its length (Figures 3c and 3d). Electron-transparent (< 100 nm) cross-sectional samples were prepared by FIB milling of the benches at a low accelerating voltage, 5 kV. TEM and selected area electron diffraction (SAED) measurements were carried out using a Titan (FEI) S/TEM operated at 300 kV.

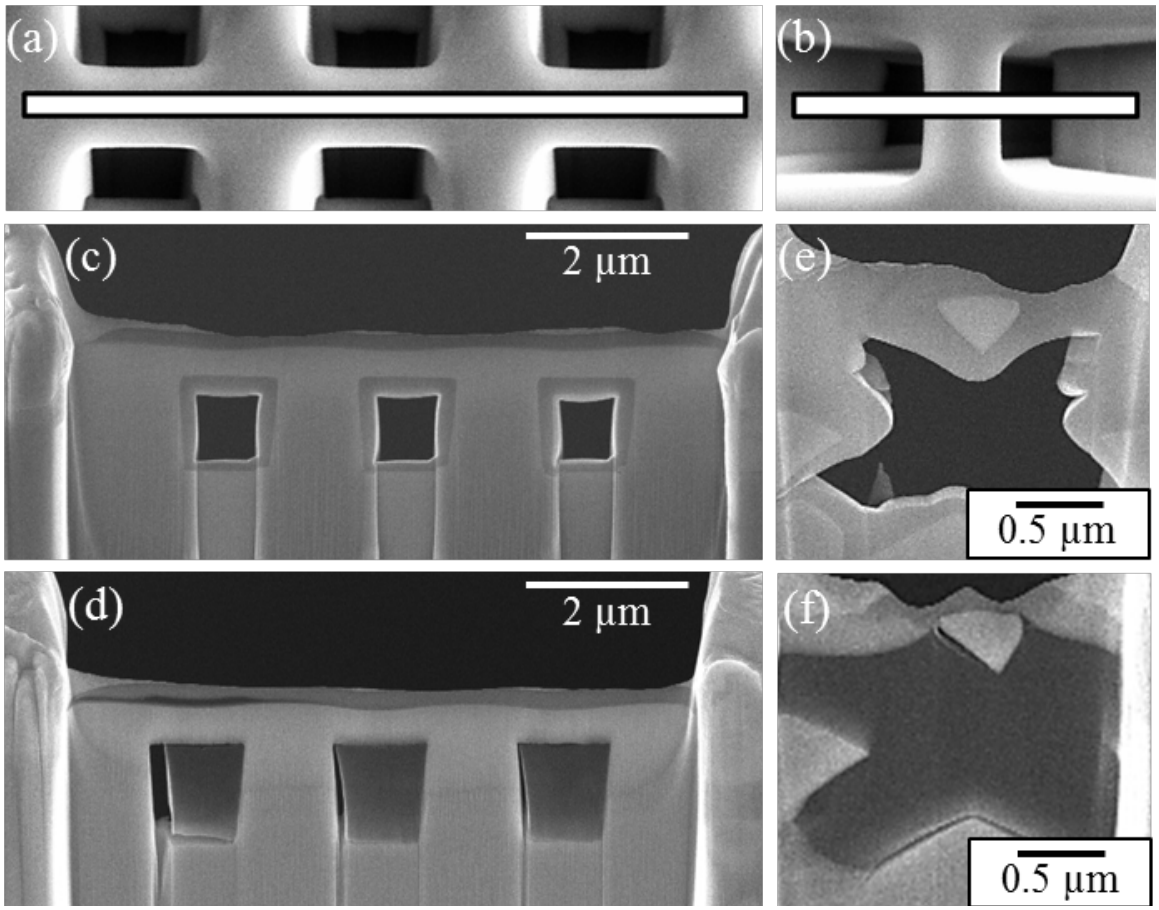

FIG. 5.3. SEM Images of the cross-sections created from the benches. Schematics of where the cross-sections were taken is shown in **(a)** and **(b)** above via the white rectangular area for the length-wise cross-section and the width-wise cross-sections,

respectively. Length-wise cross-section of the benches with **(c)** being the reference and **(d)** being the benches loaded at 64.7 kJ/m^2. Cross-sections from the middle of the pillar, perpendicular to its length are shown in the SEM images of **(e)** the reference and **(f)** the bench loaded at 64.7 kJ/m^2.

5.3 Results and Conclusions

Figure 5.4a is a typical interferometric fringe record obtained at a laser fluence of 95.2 kJ/m^2 from the free surface of the isolated glass plate sample using the same stress generation conditions as those used to shock-load Cu benches. Figures 5.4b and 5.4c show the corresponding velocity and stress wave profiles, $u(t)$ and $\sigma(t)$, respectively obtained from this fringe record, by using the well-established procedures of interferometry mentioned earlier. Using this stress wave profile as input, finite element simulations of the wave propagation under identical experimental conditions yielded a maximum compressive stress of 1 GPa and peak strain rate of 3 x 10^7 s^{-1} inside the Cu benches. In the following sections, we focus on the effect of shock-loading on morphologies and microstructures of the benches.

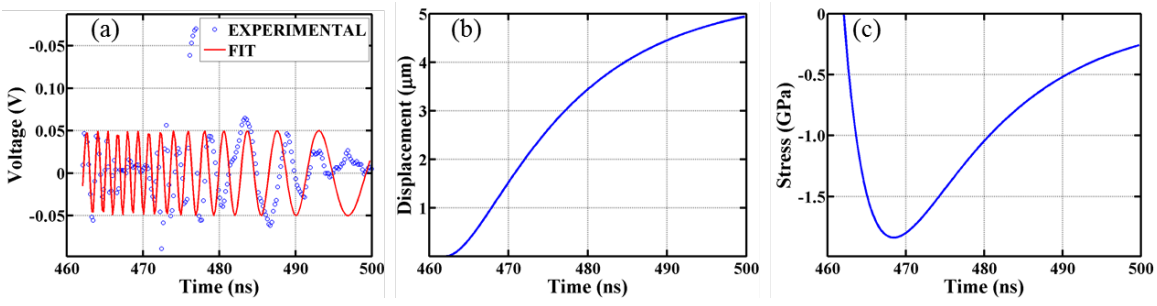

FIG. 5.4. (a) Fringe record obtained at laser fluence 95.2 kJ/m^2 using the interferometry shown in Fig. 2b. **(b)** The reduced displacement profile derived from (a). **(c)** The stress wave profile derived from (b).

In order to investigate the effect of shock-loading on surface morphologies of the Cu benches, each of the bench groups were subjected to a different laser fluence and the resulting morphologies were examined using SEM. Figure 5.5 is a representative panel of SEM images acquired from one set of benches belonging to the region loaded with a laser fluence of 64.7 kJ/m^2. Figure 5.5a shows this set of Cu benches prior to loading while Figure 5.5b shows this same set of Cu benches after they were shock-loaded under uniaxial compression by stress waves generated at laser fluence of 64.7 kJ/m^2. Following loading, the sample containing these two different benches was submerged in isopropyl alcohol (IPA) for ten minutes. It is assumed that IPA helps dissolve any oil that may be present on the sample, which was surrounded by an oil bath used as a coupling medium during loading. The sample was subsequently removed from the IPA solution and left air-exposed for 7 h at room temperature. On the shock-loaded benches, the images reveal a growth of a compact carbon rich region.

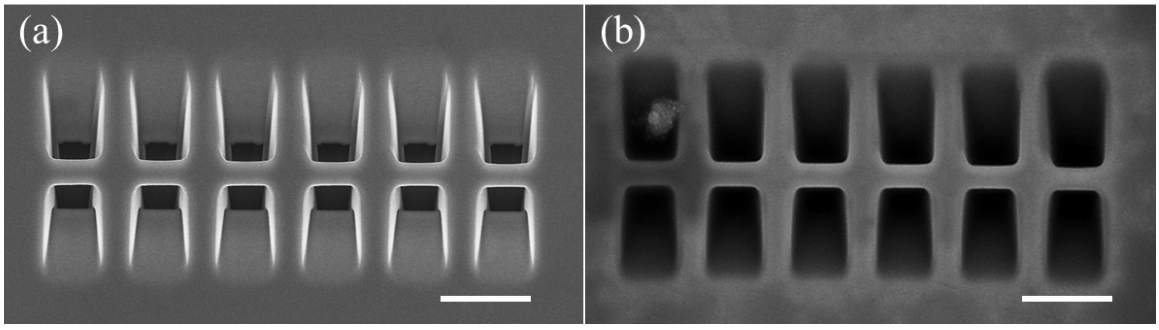

FIG. 5.5. Scanning electron microscopy (SEM) images of Cu benches on a Cu(001) substrate that have been loaded with a laser fluence of 64.7 kJ/m^2. **(a)** is as prepared via focused ion beam (FIB) milling prior to testing and **(b)** is obtained 24 h after loading. The scale bar in the images is 2 μm.

Later, the same sample was submerged in IPA solution for additional 3 h, removed, and air-dried for 19 h at room temperature. Subsequently, the SEM image acquired from this sample is shown in Figures 5.5b. The time t = 29 h indicated in Figure 5.5b is the total time elapsed between the loading of the sample and the acquisition of SEM images shown in the last column. The images reveal extensive growth of the carbon rich region around the shock-loaded benches. In contrast, the surface morphology and surroundings of the reference benches changed little over the 29 h. Given that all the benches were situated on the same Cu sample, submerged in the same set of solutions, and for the same duration, the observed carbon growth on the shock-loaded benches strongly suggests that shock-loading enhanced their surface reactivities.

In order to identify the chemical composition of the carbon film formed around the Cu benches, SAED data was used. Figure 5.6a is a typical TEM image of the bench shown in Figure 5.5b, shock-loaded at 64.7 kJ/m^2. Figure 5.6b is a representative SAED pattern obtained from the dark contrast region, which is circled in Figure 5.6a. The observed diffraction rings indicate that the film is polycrystalline. From the measured interplanar spacings, we determined the crystal structure to be a type of solid carbon, likely Cliftonite (JCPDS No. 34-567). We attribute the observed growth to the exposure of fresh Cu surfaces resulting from surface material spallation and the formation of surface steps and nanoscale facets via elimination of the dislocations from the bulk. In the following section, we provide evidence for shock-induced dislocation motion, a strong indication of mechanical annealing.

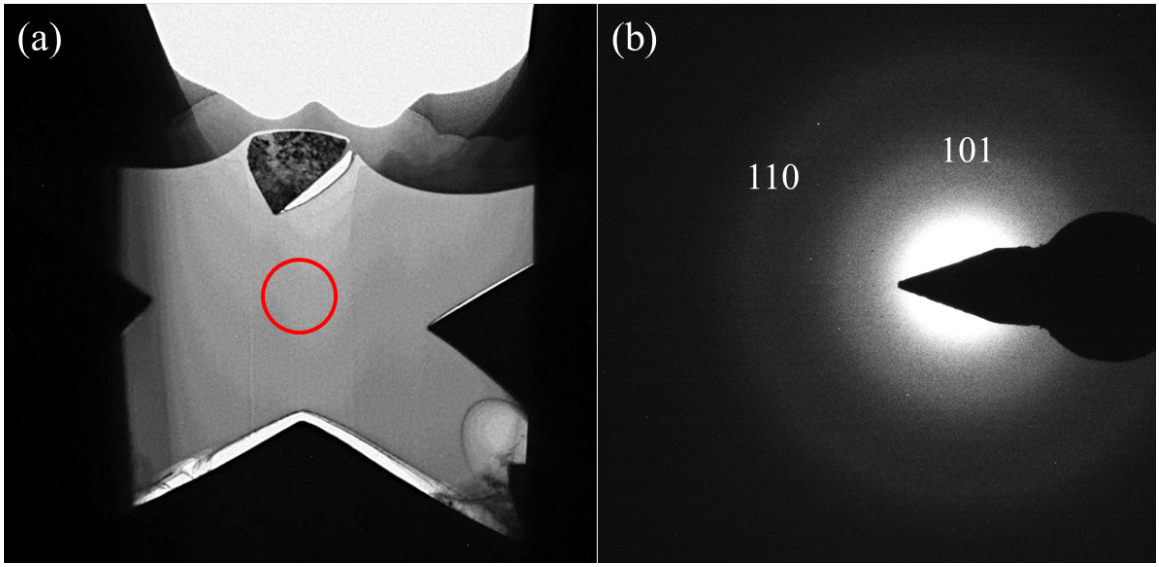

FIG. 5.6. (a) Bright-field transmission electron microscopy (TEM) image of the loaded with laser fluence of 64.7 kJ/m^2 width-wise cross-section, including the regions surrounding the copper bench cross-section (triangle shape). **(b)** Selected area electron diffraction (SAED) pattern of region under the bench from circled region in (a).

Figures 5.7a and 5.7b are typical bright-field TEM images of a reference bench that was not shock-loaded lengthwise (Figure 5.7a) and a bench that was independently loaded with a laser fluence of 64.7 kJ/m^2, lengthwise (Figure 5.7b). Figures 5.7c and 5.7d are TEM images of a reference bench not loaded, cross-wise (Figure 5.7c) and bench that was independently loaded with laser fluence of 64.7 kJ/m^2, cross-wise (Figure 5.7d). The SAED pattern in Figure 5.7e is obtained from the bench in Figure 5.7a and is identical to the diffraction (not shown) from the shock-loaded benches. That is, in our experiments, shock-loading did not affect the crystallinity of the benches. All the TEM images show darker contrast cellular structures within the benches. A majority of these features are dislocations. The high density of dislocations observed in the bulk of the reference bench (Figure 5.6a) could be attributed to the quality of the Cu crystal. And, the dislocations present around the surface of the benches are likely due to the FIB milling process used

to fabricate the benches [51]. Since all the benches were milled out of the same Cu(001) crystal and used the same FIB parameters, it is expected that the density and spatial distribution of dislocations were similar in all the benches prior to shock-loading. While the microstructures of shock-loaded bench shown in Figure 5.7b are qualitatively similar to that of the as-prepared bench, it is possible that shock-loading can increase or decrease the dislocation density by nucleation of new dislocations or by removal of dislocations by motion from the bulk to the surface, respectively. The latter process results in the formation of new surface steps and/or nanoscale facets, which could explain the enhanced surface reactivity of the shock-loaded benches (Figures 5.5f).

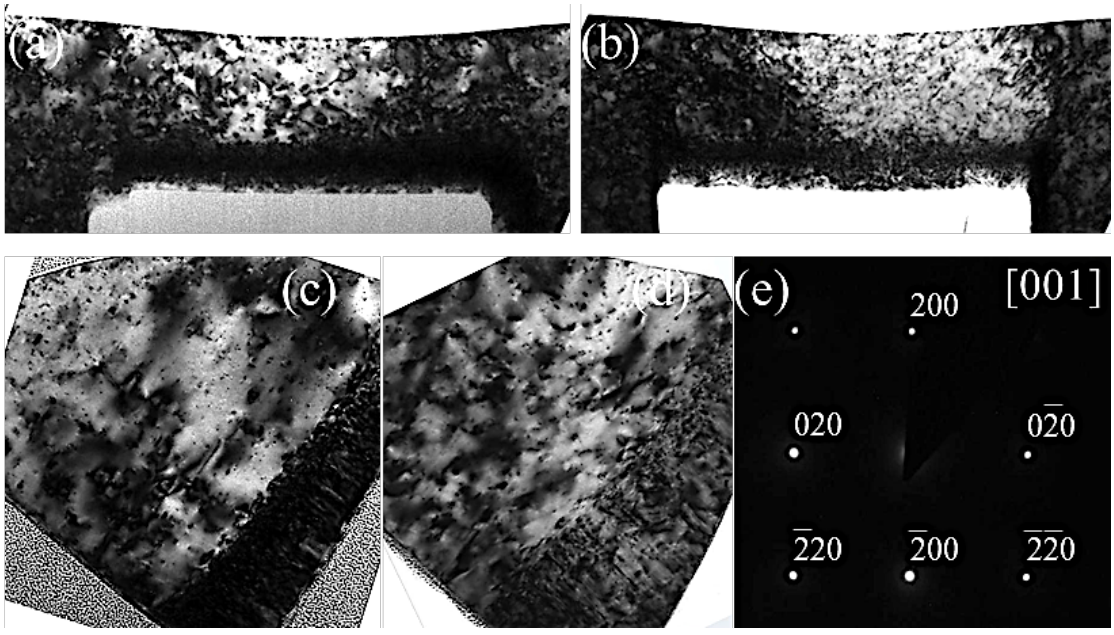

FIG. 5.7. Bright-field transmission electron microscopy (TEM) images of two different Cu(001) benches with lengthwise cross-sections, acquired **(a)** as-prepared and after shock-loading using laser fluence of **(b)** 64.7 kJ/m^2. Cross-sections through the middle section, perpendicular to the length of the pillar are shown via TEM images in **(c)** for the reference and **(d)** for the loaded with laser fluence of 64.7 kJ/m^2. All benches were oriented along the [001] zone axis during TEM analysis. **(e)** Selected area electron diffraction (SAED) pattern of the bench shown in (a).

To address the possibility of dislocation mobility in the samples, the movement of the dislocations created via FIB radiation is evident. When first observing the lengthwise samples in Figure 5.7, it is clear that the top portion of the bench is fairly dislocation free while the bottom portion of the bench is quite heavy in dislocations (Figure 5.7a). This can be explained by the increased dislocations due to the FIB radiational damage which is present on the bottom portions of the bench but never directly hit the very top and middle of the benches. Therefore, the top is relatively low in dislocations prior to the shock-loading. Post shock-loading, one can see that in Figure 5.7b, the dislocation density appears to decrease on the bottom of the bench while the top of the bench contains significantly more dislocations. This becomes even more clear in the cross-section (widthwise) of the middle of the benches for the reference and loaded regions. They not only show that the dislocation density is higher on the bottom of the pillar but also that it is mainly on one side of the bench. This is likely due to the double milling of one side of the benches during the sample preparation.

To quantitatively assess the effect of shock-loading on the microstructure of the benches, dislocation orientations were determined. For consistency, all the TEM images analyzed were acquired under identical imaging conditions, i.e. 300 kV accelerating voltage and [001] zone axis. And, since the TEM samples were prepared using FIB, those dislocations near the bench's surface and especially bench's bottom were ignored. Orientations of dislocations visible in the TEM images (Figures 5.7a-c) were measured with respect to the {100} axes of the benches. In FCC metals such as Cu, the dislocations with Burgers vector $\mathbf{b} = \frac{1}{2}[110]$ appear oriented at 45° with respect to the {100} axis of

the benches, when viewed in the TEM along [001] zone axis [53], [61]. In the reference bench, the average angle subtended by the dislocations is 49.1 ± 11.0° (SD) for the length-wise bench and 46.8 ± 9.8 (SD). In comparison, the angles are 55.14 ± 15.8° (SD) and 41.9 ± 18.0° (SD) in samples loaded with stress waves generated at laser fluence of 64.7 kJ/m^2 for the lengthwise and widthwise, respectively. While the average angles are nearly the same within the measurement uncertainties, note the increase in deviations in angles from 11.0° and 9.8 in the reference bench to 15.8° and 18.0° in the shock-loaded samples. That is, the orientational spread of dislocations increases with increasing laser fluence. These results provide further evidence in support of the hypothesis that shock-loading induces motion of the dislocations and/or formation of new dislocations.

As seen in previous studies (Youssef *et al.* [60]), the density and orientation of dislocations depend on the laser fluence. These results can be explained as follows. The stress waves generated within the benches due to the laser shot are transient and over a short duration (~ 30 ns). Therefore, the amplitude of the stress and strain rate change continuously with a maximum stress of 1 GPa and strain rate of 3 x 10^7 s^{-1} for a laser fluence of 95.2 kJ/m^2. At such high strain rates and short time scales over which the benches were loaded at a given stress value, motion of pre-existing dislocations is limited because of the increase in the local shear strength of the slip systems. When dislocation motion does occur, it is limited as they are eventually pinned by their neighbors and additional stress is required for their continued motion. This dislocation pinning can also lead to nucleation of new dislocations. Those dislocations present near the surface, however, are likely to escape leaving behind surface steps and nanoscale facets. This is

consistent with the TEM observations of a relatively low density of dislocations within the top 30 nm of the shock-loaded benches. Consequently, dislocation motion is expected to be higher at higher laser fluence resulting in the observed lower dislocation density and wider orientational spread.

6 Copper Nanopillars Loaded at High Laser Fluence

6.1 Introduction

After obtaining interesting results in Chapters 3, 4 and 5, all at relatively low laser fluence and therefore, low stress it was of interest how these nanostructures could withstand larger pressures still at high strain rates and short pulse durations. This set of experiments was setup nearly identically to those in Chapters 3, 4 and 5. The only change in this experiment compared to those of Chapters 3 and 5 is the use of a polycrystalline copper momentum trap that was impedance matched to the single crystal copper substrate. The momentum trap was also made to be significantly thick (10 mm) so that the wave would disperse and the copper nanopillars would not be reloaded by the reflected tensile wave. The surface of the copper momentum trap that was mechanically pressed against the single crystal copper substrate was polished to a mirror finish to also allow for wave continuity. Similar to the previous studies, an oil bath was utilized to allow for continuity of the wave to transfer from the nanopillar samples into the momentum trap.

6.2 Experimental Procedure

We have seen that at pressures approaching 1 GPa, we have the chemical activation of the surface of Cu nanopillars. Information on this is provided by Youssef *et al.* [60]. For further testing, Cu nanopillars will be loaded at higher laser energy fluence levels than that of Youssef *et al.* [60]. The setup of this experiment is similar to that of the work published by Youssef *et al.* [60], as shown in Figure 1. As well, the pillars were

prepared on a single crystal copper substrate with orientation [001] with 8 pillars per region that were loaded uniformly by a 2.3 mm diameter spot size.

Previous testing (Chapter 3) explored laser fluence levels of 38.8, 63.5 and 93.5 kJ/m^2. For the higher laser fluence experiment, we will load pillars with laser fluence levels of 144.9, 303.3 and 512.6 kJ/m^2, all with a 2.3 mm spot size. In this setup shown in Figure 6.1, wave trap is applied to the back surface of our single crystal copper sample to ensure the wave would transmit through the pillar interface and only provide a state of compression in the Cu pillars. Since the wave speed of Cu is approximately 4360 m/s and the duration of the stress wave is approximately 30 ns, the compression wave has a length of approximately 130 μm. Therefore, at a time in the loading of the Cu nanopillars, there is nearly a quasistatic compression state. By going through this range of fluence previously described, a critical laser fluence where the Cu nanopillars began to bend and then deform via bulging (Taylor Impact Experiment).

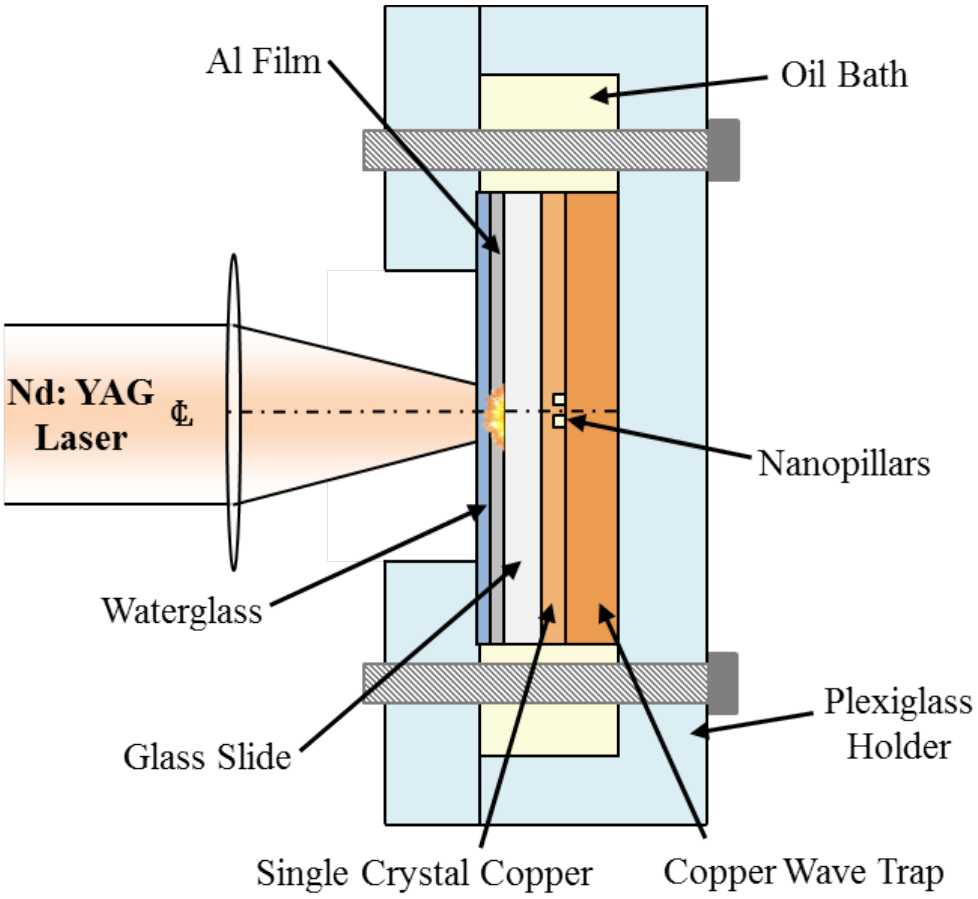

FIG. 6.1. Laser shock-loading apparatus for high-energy testing

6.3 Results and Conclusions

Figure 6.2 shows before and after images of pillars under different loading conditions of 144.9 kJ/m^2, 303.3 kJ/m^2, and 512.6 kJ/m^2. We can see that there is a threshold some value, higher than the 39.5 kJ/m^2, 63.5 kJ/m^2, and 93.4 kJ/m^2 studied in Youssef *et al.* [60] where there is clear bending/buckling of the Cu nanopillars. In order to further analyze this phenomenon, transmission electron microscope (TEM) cross-sections through the middle of the pillar in Figure 6.2b was were fabricated via the FIB "lift off method" used in Chapters 3, 4 and 5 and discussed in Chapter 2.6.

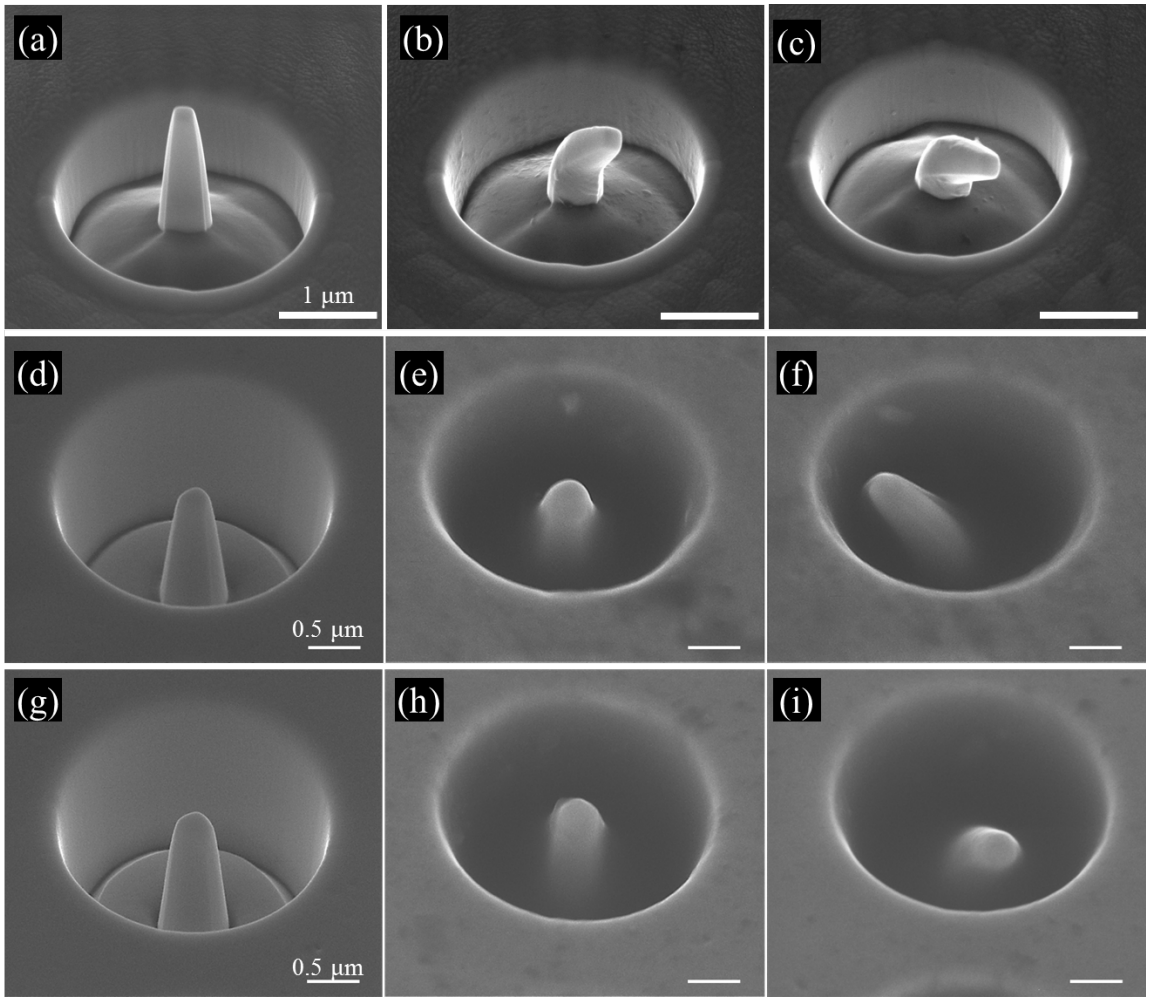

FIG. 6.2. (a, d, g) Cu nanopillar prior to shock-loading. **(b, c)** after loading the pillar with a 144.9 kJ/m^2 fluence shock-wave, **(e, f)** after loading pillar with a 303.3 kJ/m^2 fluence stress wave, and **(h, i)** after loading pillar with 512.6 kJ/m^2 fluence stress wave.

Finally, a state of the art FEI Titan Transmission Electron Microscope was utilized. First low magnification images were taken in order to observe the bending of the pillar (shown in Figure 6.2b) and its diffraction pattern (shown in Figure 6.3). In the diffraction image taken from the base of the pillar, there is an elongation of the diffraction spots, shown in Figure 6.3a. This would indicate that the atomic structure observed a significant deformation, which is to be expected. As well, the diffraction from the top of

the pillar (Figure 6.3b) shows that there is no deformation since the diffraction spots are not elongated in any direction.

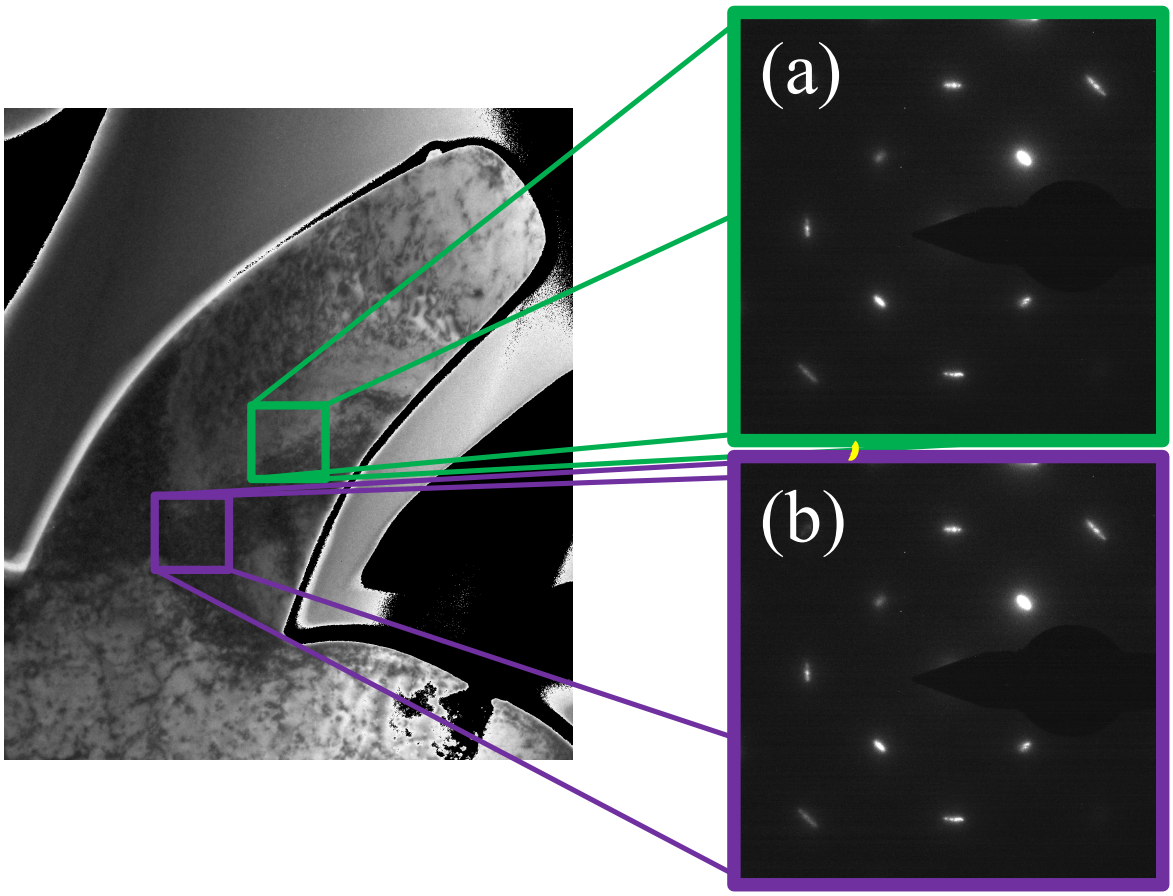

FIG. 6.3. TEM analysis of the bent Cu pillar due to high-energy loading **(a)** diffraction from the base of the pillar and **(b)** diffraction from the top of the pillar. Image taken in [001] zone axis.

In order to learn the deformation mechanism, it was necessary to take high-resolution transmission electron microscope (HRTEM) images of the bent pillar. The inside (contracted side) of the bent pillar TEM sample was analyzed. There appear to be multiple mechanisms in which the copper pillar will bend. One way, demonstrated in Figure 6.4 is by sharp kinks similar to those found by Orowan [62]. In Figure 6.4, the

kink observed is at a 5.5° angle. We find that the sample does not bend uniformly because even though it is a single crystal, the sample will indeed have defects, which cause the sample to bend/kink non-uniformly. With kinking it is expected that there will be twin formation. Even though HRTEM micrographs hinted to the possibility of twin formation, twins could not be clearly found within the sample. These can be of significant interest as Colorado *et al.* [63] demonstrated the potential for a single grain of copper to become multiple grains.

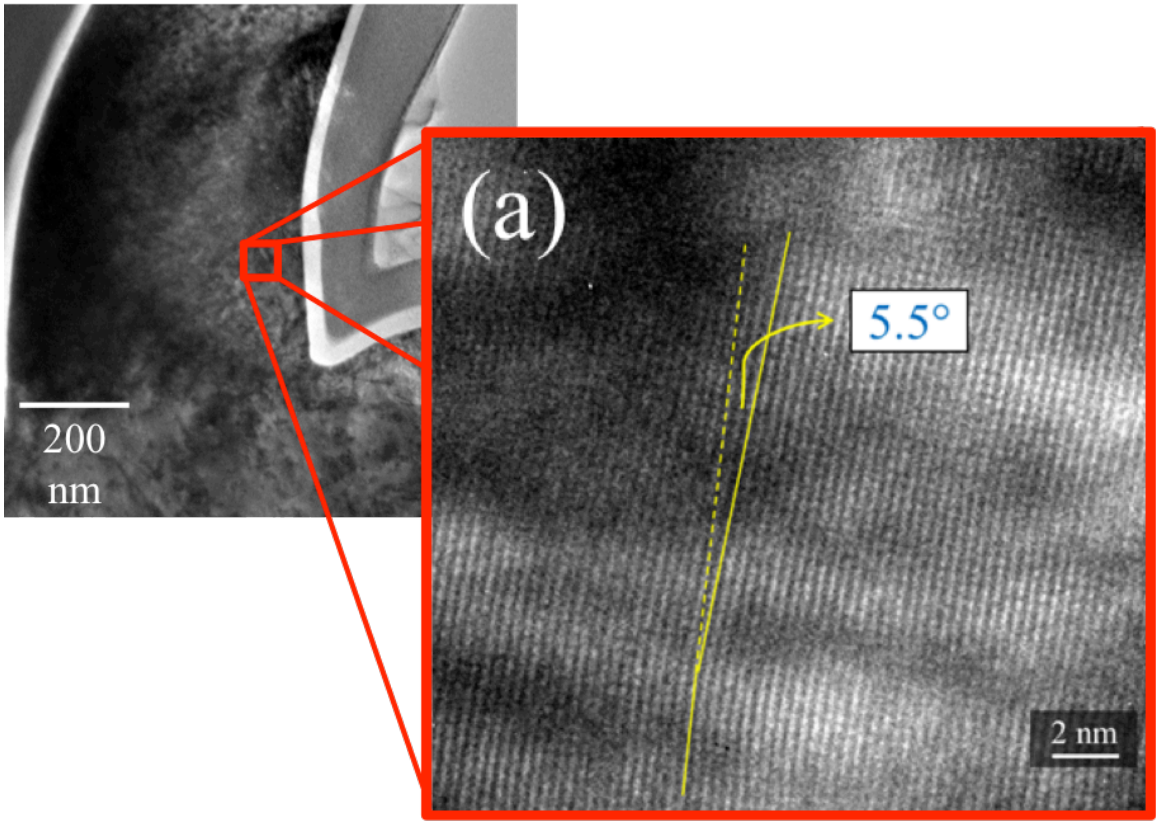

FIG. 6.4. HRTEM analysis of the bent Cu pillar due to high-energy loading with kinking of 5.5° of the atomic structure. Image taken in [001] zone axis.

Then, it was observed that at a 303.3 kJ/m^2 laser fluence there was deformation by both bending and bulging plastic deformation similar to that seen in Taylor Impact studies

[64]–[69]. From this realization, utilizing the particle velocity of the stress wave from the interferometry calculations the behavior dynamic yield stress can be determined [64], [65]. The calculations for this will be provided in Chapter 7 where this was observed in copper nanopillars loaded at high laser fluence levels but at cryogenic temperatures. The equations that dictate this deformation are defined by Wilkins and Guinan [65] as:

$$\frac{L_1}{L_0} = \left(1 - \frac{h}{L_0}\right) \exp\left(-\frac{\rho_0 U^2}{2\sigma_{yd}}\right) + \frac{h}{L_0} \tag{6.1}$$

and solving for σ_{yd} we get:

$$\sigma_{yd} = \frac{-\rho_0 U^2}{2 \ln\left(\frac{L_1 - h}{L_0 - h}\right)} \tag{6.2}$$

The calculations by Wilkins and Guinan were inspired by the work from Taylor [64] which is shown below:

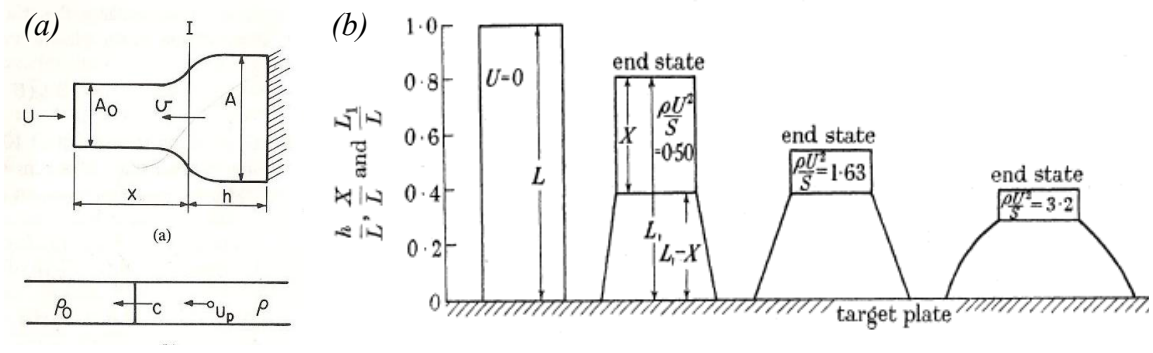

FIG. 6.5. (a) A schematic of the Taylor Impact studies and **(b)** is a simplified model for calculation of the dynamic yield strength of the material of interest depending upon its end state geometry. Figure from Taylor [64].

In this study, it is clear that beginning at 144.9 kJ/m^2, deformation by bending begins in the nanopillars. Following this, at a laser fluence of 303.3 kJ/m^2 deformation of bending and bulging of the nanopillars occurs. This means that it is at the 303.3 kJ/m^2

that bulging as seen in the taylor impact experiments will occur. It will be seen in Chapter 7 that when loading nanopillars at the same laser fluence levels but at cryogenic temperatures, bulging of the pillar will not occur until 512.6 kJ/m^2, delaying the onset of this phenomena.

In conclusion, a testing procedure was provided that allowed for testing of Cu nanopillars similar to those of Chapter 3 but loaded at higher laser fluence levels. Therefore, new deformation mechanisms were observed in the form of bending of the nanopillars and bulging of the nanopillars. It is clear that at a laser fluence of 144.9 kJ/m^2, associated with a stress state in the nanopillars exceeding 1 GPa, the onset of bending deformation for pillars that were 1.25 μm tall with 450 nm diameters occurs. At a laser fluence of 303.3 kJ/m^2 the onset of bulging of the nanopillars began similar to that of the Taylor Impact experiments.

7 Copper Nanopillars Loaded at Cryogenic Temperatures

7.1 Introduction

In this chapter we explore the fundamental connection between small size and ductility in metallic solids and explore if such a relationship can be maintained even under ultrahigh strain rate loading and cryogenic temperatures. Most engineering materials behave in a brittle fashion under such conditions. This even includes the Face Centered Cubic (FCC) metals such as copper that are among the most ductile materials when deformed at room temperature and lower loading rates. On a fundamental level, this brittleness under extreme conditions results from the very low mobility of nucleated and pre-existing dislocations as the phonon drag mechanism that controls their mobility in FCC metals at room temperature and lower loading rates becomes inefficient because of the increase in the rate-dependent viscous drag force on the dislocations. Regardless, FCC metals deform in a brittle fashion under extreme conditions. A question that arises naturally is can the microstructures of these metals be designed such that they respond in a ductile fashion under all loading conditions?

A new experimental apparatus was developed to shock load nanostructures, in-situ, at cryogenic temperature. This design was motivated by the desire to further increase the strain rate of deformation by effectively shutting down the thermal activation mechanism for the mobility of dislocations and thereby subjecting the material of the pillars to ultimate extreme conditions. Shown in Chapter 6, we were able to successfully deform nanopillars under uniaxial compression loading at laser fluence exceeding 144.9

kJ/m^2. These deformation mechanisms were in the form of bending (> 145 kJ/m^2) or bulging (> 300 kJ/m^2).

7.2 Experimental Procedure

This is a fairly sophisticated setup (Fig. 7.1) comprising of an environmental cell equipped with springs capable of holding the nanopillars submerged in a liquid nitrogen bath while still able to receive the shock wave generated by the laser. The loading procedure was the same as that utilized in Chapters 3, 4, 5 and 6 with loading at a range of laser fluence levels from 38.8 kJ/m^2 to 512.6 kJ/m^2.

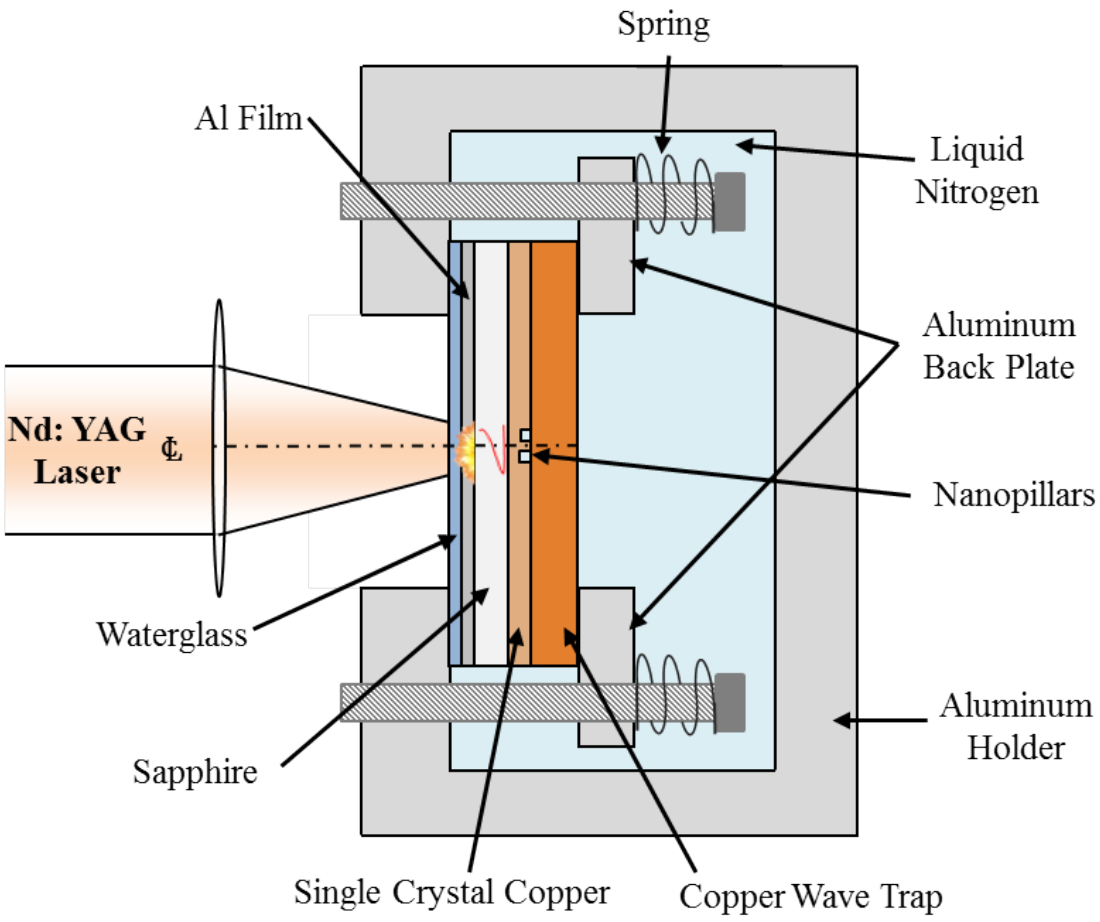

FIG. 7.1. Experimental setup for loading copper nanopillars at cryogenic temperatures via laser generated stress waves.

A Focused Ion Beam (FIB)-based procedure was used to fabricate Cu nanopillars 1.25 μm tall and 450 nm in diameter from a Cu (001) substrate plate. Groups of 8 identical pillars, each spanning a 6 μm dia area, were prepared in a Nova 600 Dual Beam focused-ion-beam/scanning electron microscope (FIB/SEM) system using gallium ions at 0.5 nA current and an accelerating voltage of 30 kV. Selected area electron diffraction (SAED) pattern of the reference pillar in Figure 3.3d from Chapter 3 confirms the pillar to be single crystal albeit it is populated with pre-existing dislocations with density 7.9 x 10^{14} m^{-2} as shown in the bright-field TEM image (Figure 3.3a from Chapter 3) of the reference unshocked pillar when viewed along the [001] zone axis.

It is remarkable that the material is able to accommodate such a large strain even under such extreme conditions. In this study, we obtain ductile deformation by bending and bulging of the sample. Through Taylor Impact testing analysis of the bulged samples, we can determine the dynamic yield stress σ_{yd} of copper under these loading conditions. These can be correlated with new MD simulations, which will be revised by shutting down the thermal activation process. A natural outcome of the above exercise will be further determination and even revision of the dislocation nucleation stress in Cu.

We showed that Cu nanopillars of 450 nm in diameter deformed in a ductile fashion even under extreme strain rate (> 10^7 s^{-1}) and temperature (83 K) conditions. The nucleation stress for Shockley partials was measured to be ~1 GPa [13] which is an order

of magnitude lower than its previous well-established value in bulk. These results suggest that there may be a fundamental connection between small size and ductility that cannot be perturbed either by ultrahigh strain rate loading or cryogenic temperatures. In this work we present results from our FCC copper study in which single crystal nanopillar samples of Cu of 1.25 μm in length and 450 nm in diameter were loaded by laser-generated stress waves of nanosecond rise times, under extreme conditions of strain rate (> 10^7 s^{-1}), and temperature (83K). Since shock loading is performed on very small samples it provides an extremely powerful tool to experimentally correlate the evolved structures to experimental parameters of pressure, strain rate, and temperature with minimal modeling.

The stress state inside the copper pillars was determined using a two-step procedure. In the first step, the incident stress wave σ(t) generated inside the glass plate was measured in a separate experiment using interferometry. In this experiment, an isolated glass plate was shock-loaded under the same stress wave generation conditions (laser fluence and thicknesses of glass substrate, Al film, and waterglass layers) as those used for shock loading of the Cu pillars. The free surface velocity v(t), recorded using the optical interferometer, is used to calculate σ(t) by equation:

$$\sigma(t) = \frac{\rho c_o}{2}\left[v\left(t + \frac{h}{c}\right) - v\left(t - \frac{h}{c}\right)\right] \qquad (7.1)$$

where c (= 2289 m/s) is the longitudinal wave speed in the glass, and ρ and h are its density, and thickness, respectively (Pronin and Gupta, 1997). In step 2, the exact stress-state inside each pillar was determined using a finite element (FE) simulation with σ(t) as an input. The FE model was implemented in ABAQUS. The mesh size was kept uniform

in all domains so as to prevent the spurious wave reflection effects that are known to occur at material interfaces and furthermore the time step of 0.2 ns was used to satisfy the numerical stability requirement relating Δt to element size Δx through the wave velocity c : $\Delta t < \Delta x/c$. The local stresses from obtained from the FE model were used for carrying out the Molecular Dynamics (MD) simulations under shock compression (Youssef *et al.* [60]).

7.3 Results and Conclusions

As shown in Figure 7.2, there are minimal changes if any to the external structure of these copper nanopillars when comparing the reference, 38.8 kJ/m^2, 63.5 kJ/m^2, 91.7 kJ/m^2 and 144.9 kJ/m^2. At laser fluence levels as low as 38.8 kJ/m^2, Chapter 3 demonstrated the ability to have a chemical activation of the nanopillar's surface where film growths would occur. Following this, at a laser fluence of 144.9 kJ/m^2 and 303.3 kJ/m^2, Chapter 6 showed plastic deformation of the copper nanopilllars via bending and bulging, respectively. These types of deformations appear to not occur at these testing levels either due to a delayed onset at higher laser energies or inability to occur under these conditions. The chemical activation of the nanopillar surface may no longer occur in the sample while a delayed onset describes the mechanism for bending and bulging as shown in Figure 7.3.

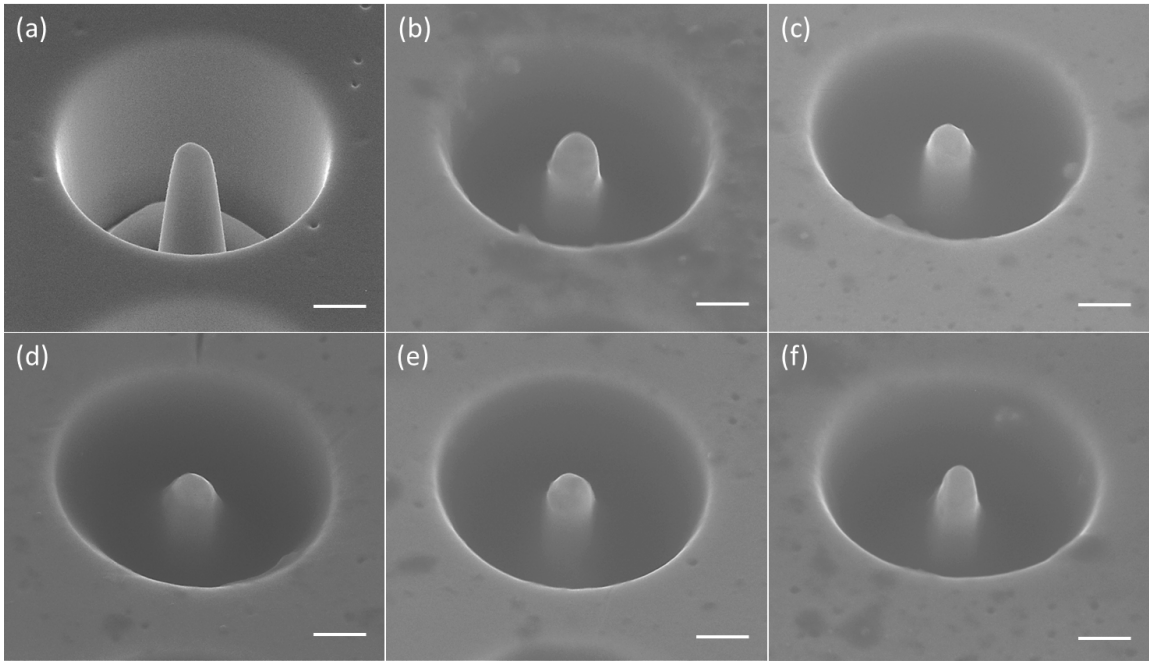

FIG. 7.2. SEM micrographs of **(a)** a typical pillar before loading at cryogenic temperatures, **(b)** a reference pillar after the testing procedure that was not subjected to the stress wave, **(c)** a pillar subjected to a 38.8 kJ/m^2 laser fluence, **(d)** a pillar subjected to a 63.5 kJ/m^2 laser fluence, **(e)** a pillar subjected to a 91.7 kJ/m^2 laser fluence and **(f)** a pillar subjected to a 144.9 kJ/m^2 laser fluence. All scale bars are 500 nm.

Figure 7.3 displays SEM micrographs of two failure modes that were observed. Depending upon the level of the axial stress and initial alignment of the shock wave propagation direction with respect to the pillars' axes, columns were found to either bend (Fig. 7.3d) or undergo large compressive strains which in turn were accommodated through substantial axial shortening and bulging (Fig. 7.3c). This demonstrates the success of our initial design and provides the confidence that we will be able to explore material deformation in a regime that has never been done before.

A further support for the above thesis was provided by the results obtained on copper pillars that were precooled to 83K before shock loading in the new setup.

Remarkably, the pillars deformed by accommodating a very large compressive strain either through substantial axial shortening (Fig. 7.3d). When the pillars were bent by orienting their axes 90° to the wave propagation direction (shock bending), pillars were found to bend by 180° without fracture even at such (10^8 s^{-1}) ultrahigh strain rates [63].

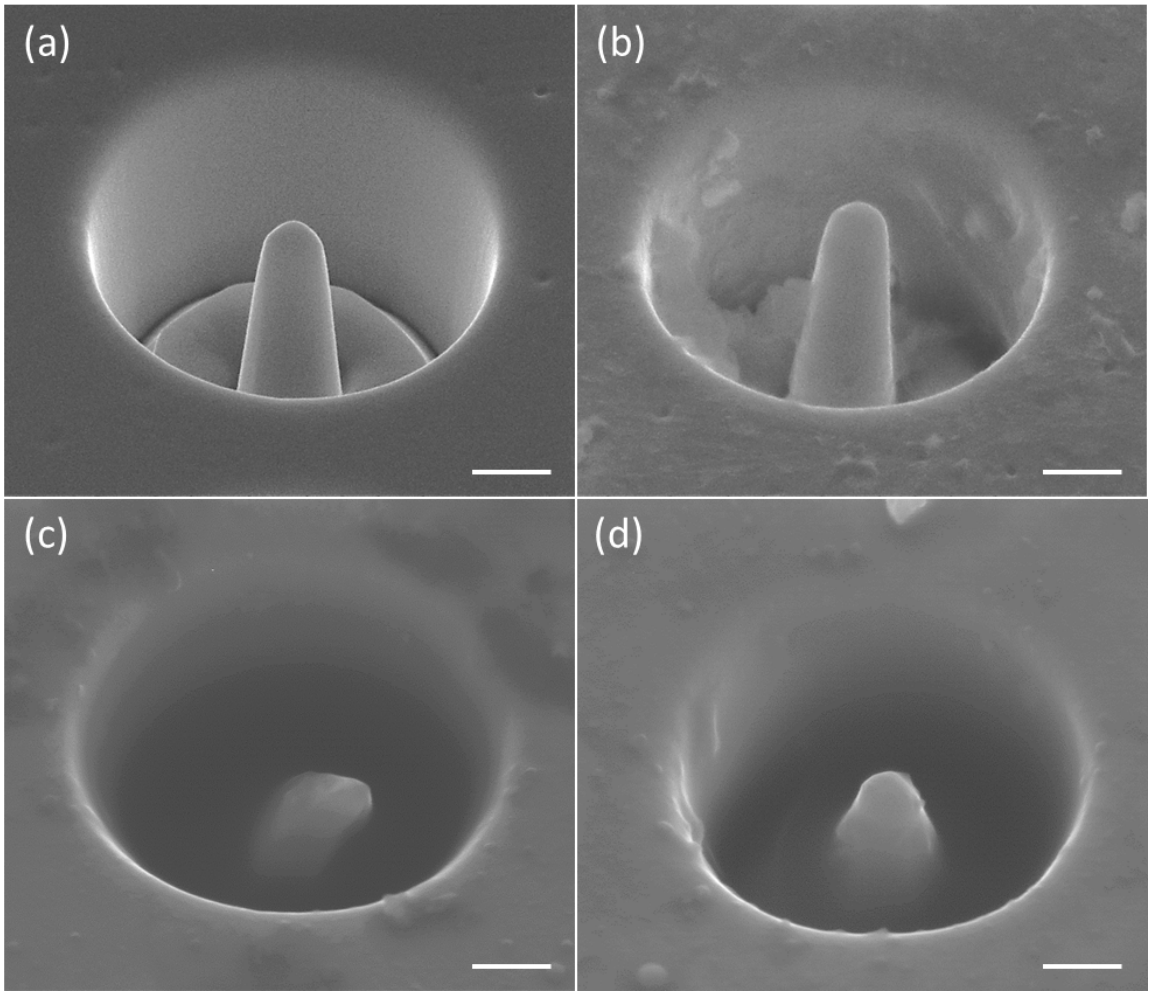

FIG. 7.3. SEM micrographs of **(a)** a typical pillar before loading at cryogenic temperatures, **(b)** a pillar subjected to a 303.3 kJ/m^2 laser fluence, **(c)** a pillar subjected to a 512.6 kJ/m^2 laser fluence, and **(d)** a pillar subjected to a 512.6 kJ/m^2 laser fluence. All scale bars are 500 nm.

After shock-loading, the pillars were lifted off the substrate using FIB and mounted on TEM grids. Electron-transparent (< 100 nm) cross-sectional samples were prepared by FIB milling of the pillars at a low accelerating voltage, 5 kV. TEM, scanning TEM (STEM), SAED, along with energy dispersive X-ray spectroscopy (EDS) measurements were carried out using a Titan (FEI) S/TEM operated at 300 kV. Figure 7.4 shows a TEM image of a post-shocked Cu nanopillar that shows clear bulging. These were analyzed at via HRTEM in order to understand the deformation mechanisms used. As well, the dynamic yield stress of the copper pillar was analyzed using the preliminary works done by Taylor [64] and work by Wilkins and Guinan [65].

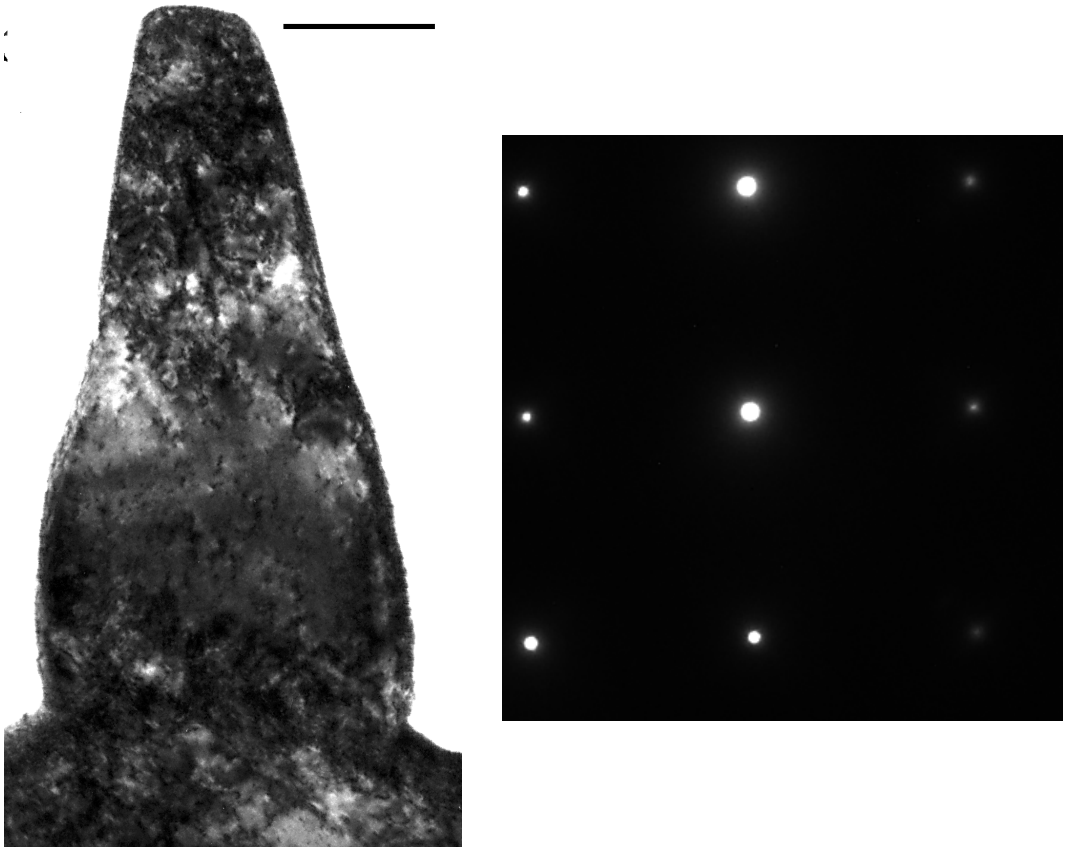

FIG. 7.4. TEM image of pillar in Figure 7.3c loaded with laser fluence of 512.6 kJ/m^2 along with the diffraction from the pillar.

In order to study the deformation of the pillar similar to that obtained in Taylor impact studies [64], [65], experimentally proven models were used in order to obtain the dynamic yield stress of the copper nanopillar under the 512.6 kJ/m^2 laser fluence loading condition. From this realization, utilizing the particle velocity of the stress wave from the interferometry calculations the behavior dynamic yield stress can be determined [64], [65]. The equations that dictate this deformation are defined by Wilkins and Guinan [65] as:

$$\frac{L_1}{L_0} = \left(1 - \frac{h}{L_0}\right) \exp\left(-\frac{\rho_0 U^2}{2\sigma_{yd}}\right) + \frac{h}{L_0} \tag{7.2}$$

and solving for σ_{yd} we get:

$$\sigma_{yd} = \frac{-\rho_0 U^2}{2 \ln\left(\frac{L_1 - h}{L_0 - h}\right)} \tag{7.3}$$

The calculations by Wilkins and Guinan were inspired by the work from Taylor [64] which is shown below:

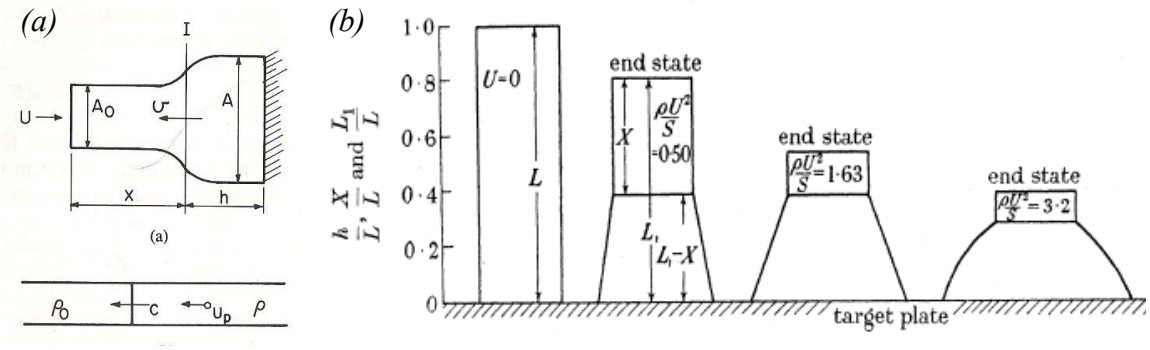

FIG. 7.5. (a) A schematic of the Taylor Impact studies and **(b)** is a simplified model for calculation of the dynamic yield strength of the material of interest depending upon its end state geometry. Figure from Taylor [64].

Variables	Definition	Our values for this study
L_1	New length	1.14 μm
L_0	Original length	1.25 μm
h	Thickness of plastic (bulging) zone	0.514 μm
ρ_0	Original density of copper nanopillar	8950 kg/m^3
U	Velocity of particles within Copper nanopillars	121 m/s
σ_{yd_WG}	Dynamic yield stress from Wilkins-Guinan model	365 MPa
σ_{yd_Taylor}	Dynamic yield stress from Taylor model	262 MPa

Table 7.1. Values used to calculate the dynamic yield stress of high laser fluence copper nanopillar experiments via Taylor [64] and Wilkins-Guinan [65] models

In the Wilkins and Guinan paper [65], they completed tests on copper cylinders at high levels of velocity. When they obtained a velocity of 123 m/s for their study, the associated dynamic yield stress was calculated as 320 MPa experimentally and matched theoretically with their model. As shown in Table 7.1, the calculated dynamic yield stress calculated in this work is 365 MPa and 262 MPa as determined by the Wilkins-Guinan and Taylor models, respectively. This is exciting that even at the nanoscale that these models hold and the calculated values match with that of the Wilkins-Guinan experiment.

In summary, a testing procedure that loads copper nanopillars under extreme conditions of pressure, strain rate and temperature is discussed. Experiments also show ductile failure mechanisms at extreme conditions of ultrahigh strain rate loading and low temperature (83K). The onset of nanosteps appears to be either delayed or bypassed while onset of plastic deformations of bending and bulging are delayed and therefore occur at higher laser fluence levels than tests completed at room temperature (300 K) (in Chapter 6).

8 Mechanical Testing of Loaded Pillars

8.1 Introduction

In Chapters 3-7, testing procedures are provided in order to mechanically load nanostructures with varying magnitude stress waves at both room and cryogenic temperatures. Following these studies, it is of importance to understand how the change in the dislocation/atomic structure of the nanopillars influences the mechanical properties of the given pillars. In order to mechanically test nanopillars, a special experimental setup is required. We have capabilities to complete compression experiments with the incredibly fine control necessary for pillars of nanometer diameters and micron heights. These compression experiments are executed in a scanning electron microscope FEI Nova 600 SEM/FIB system with 1.1 nm resolution via the PI 85 SEM PicoIndenter (Hysitron, Inc.).

8.2 Experimental Procedure

This SEM PicoIndenter transducer can exert a maximum load of 10 mN with resolution of < 3 nm and displacement of 5 μm with a resolution of < 0.02 nm. This indenter has an 8 μm boron doped diamond tip that can be used to calculate hardness, stiffness, and modulus by means of indentation, compression, bend and tensile testing ([29], [32]–[40]).

The experimental setup for the stress wave loading of these pillars is shown in Figure 8.1. This is the identical loading procedure to that of Chapter 6 but with different

laser fluence values. In this study, Cu nanopillars that were not subjected to a stress pulse were compared to Cu nanopillars that were subjected to 85 kJ/m^2 and 144.9 kJ/m^2 laser fluence generated stress waves. The PicoIndenter system's boron doped diamond tip was lowered via displacement control of 5 nm/second, shown in Figure 8.2. Due to the tapered shape of the nanopillars, calculating the exact elasticity modulus is difficult as the effective cross-sectional area is changing throughout the compression process.

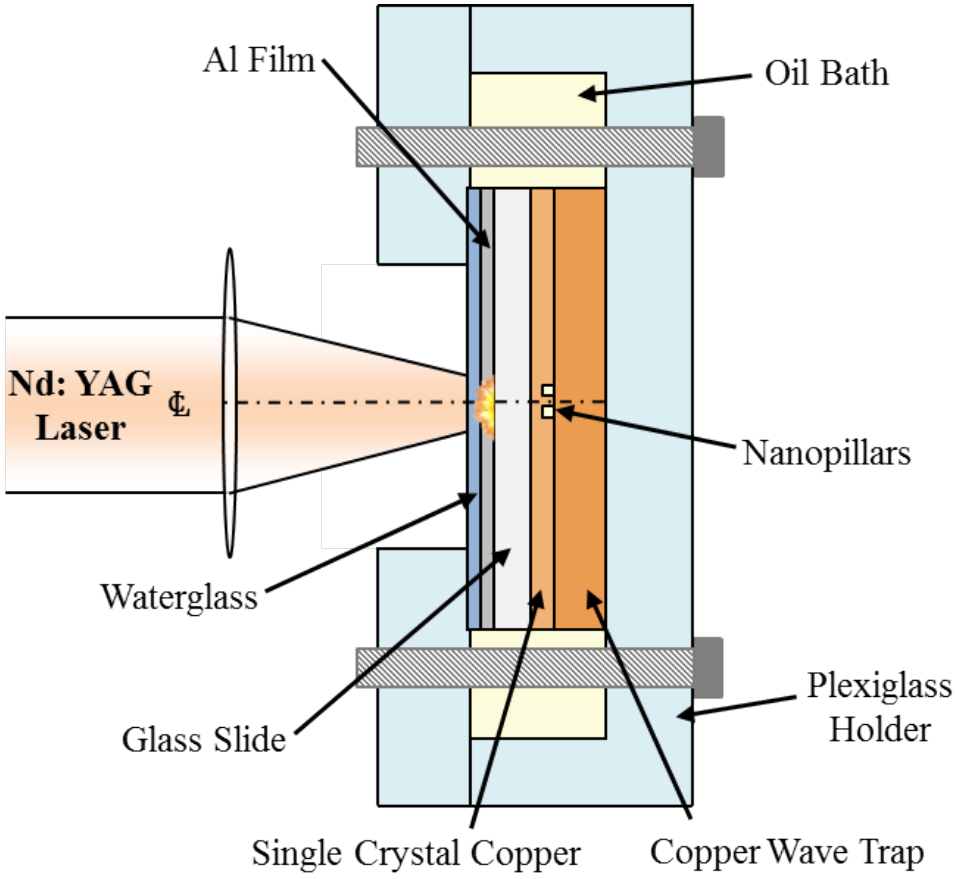

FIG. 8.1. Laser shock loading apparatus for Cu nanopillars.

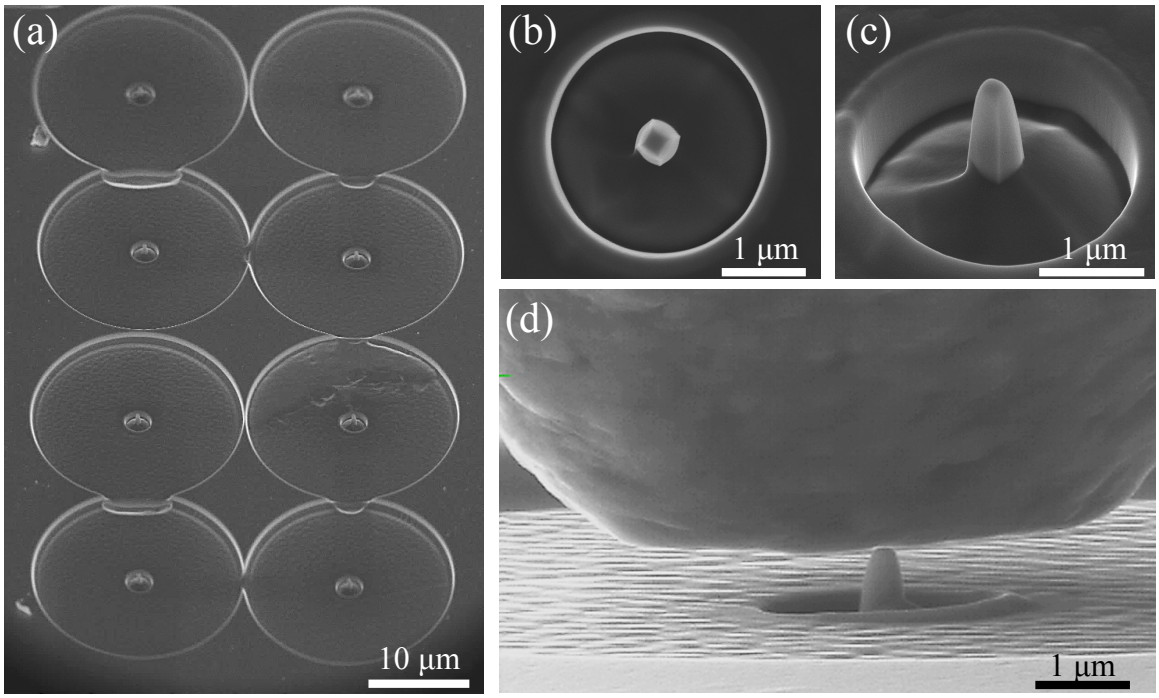

FIG. 8.2. (a, b, c) SEM Images of the Cu nanopillars to be indented for the Hysitron in-situ SEM pico-compression testing and **(d)** the Hysitron in-situ indenter being lowered to the top of the Cu nanopillar surface.

In order to test the mechanical properties of the Cu nanopillars after shock-loading, a different FIB set of prepared Cu nanopillars were needed due to the tip size of the indenters used in the compression testing. A region of 20 μm in diameter was milled away around the nanopillar (shown in Figure 8.2a) in order to not obstruct the indenter used in the Hysitron in situ-scanning electron microscope indentation system. Previous experiments provided in Chapters 3, 6 and 7 were prepared with a region of 2.5 μm surrounding the nanopillar. Figure 8.2d is an SEM image of the Hysitron indenter being lowered onto the top of a pillar prior to testing. There are several difficulties that come with this type of testing which start with the pillars being tapered. This lends itself to potential inconsistency in getting the indenter head flat on the top of the Cu nanopillars.

8.3 Results and Conclusions

In Figures 8.3 and 8.4 there are some qualitatively and quantitatively different phenomena, which are of importance to the influence that the laser induced stress wave has on these Cu nanopillars. When loaded at 85 kJ/m^2 compared to the reference in Figure 8.3, the stress strain curve demonstrates a higher propensity for the indenter head to lose contact with the top of the pillar and the force to drop down to zero. This can be described as dislocation avalanches since the deformation of the pillar equals or exceeds the 5 nm/s displacement controlled velocity of the indenter. With observations from Chapter 3 where there was significant pinning of the dislocations due to dislocation motion, it would be expected that the yield strength of the copper nanopillar would increase. As this is true, the likelihood of brittle failure also increases. It is for this reason that the more brittle, higher strength post shock loaded pillar observed more dislocation avalanches than its reference counterpart.

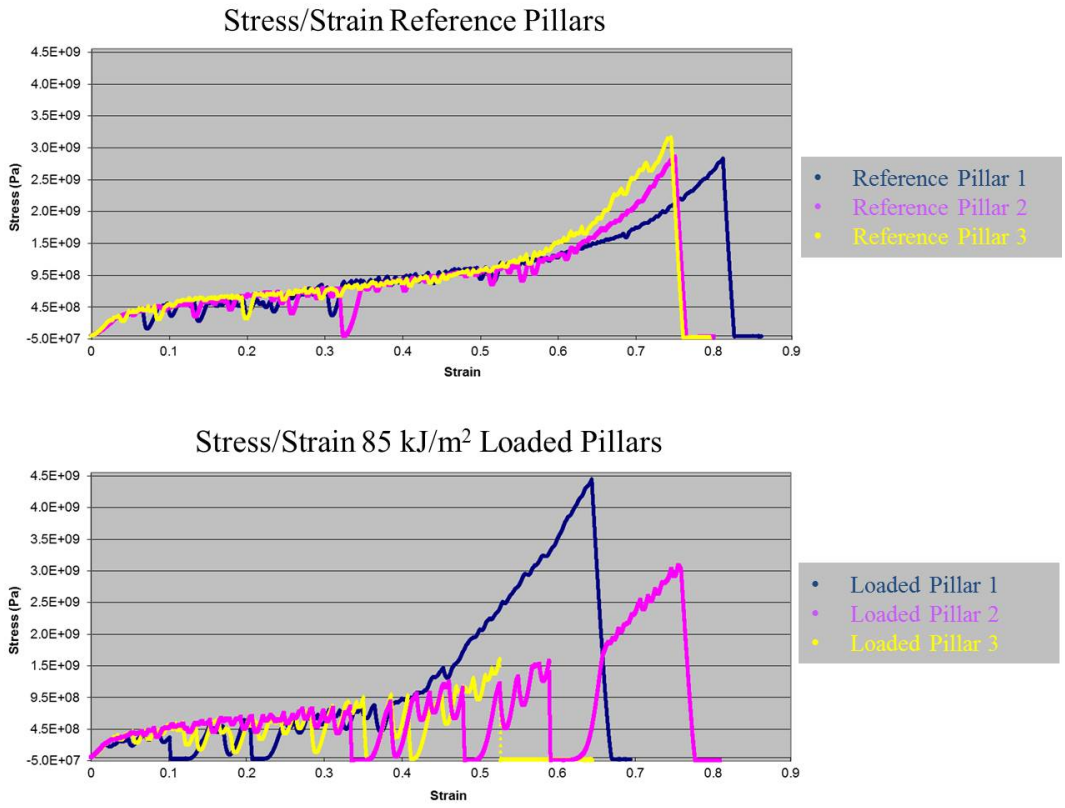

FIG. 8.3. Hysitron in-situ nano-compression testing stress strain curves of reference (not shock-loaded) and shock-loaded at 85 kJ/m^2 Cu nanopillars.

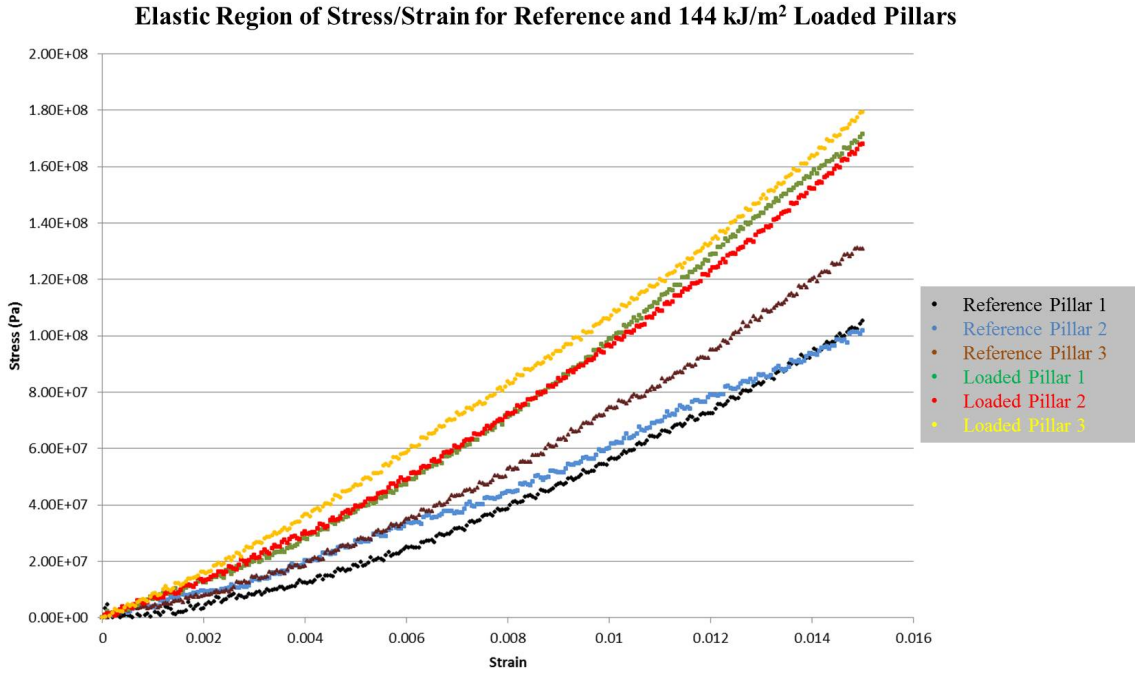

FIG. 8.4. Hysitron in-situ pico-compression testing stress strain curves of reference (not shock-loaded) and shock-loaded at 85 kJ/m^2 Cu nanopillars from the elastic/linear region of FIG. 8.3.

In Figure 8.4, the slope of the elastic regime of both the reference pillar and shock loaded at 85 kJ/m^2 pillar are analyzed. It is evident that the slope of the shock-loaded at 85 kJ/m^2 much exceeds that of the reference pillar. Both pillars are copper, so why would one be steeper. First, as shown in Chapter 3, the dislocation density decrease as the laser fluence/stress states increases. This allows for more of copper's ideal strength. Also, recall in Chapter 3 that the FIB related Ga^+ damage greatly decreased as the stress state/laser fluence increased, especially when compared to the reference. It is for both of these reasons as well as the potential densification of the Cu pillar that could attribute to the increased slope of the linear regime for the loaded nanopillar.

Next, Figures 8.5 and 8.6 analyzed pillars loaded at 144.9 kJ/m^2 by nanocompression in comparison to the reference nanopillar that was FIB milled on the same Cu substrate. In these experiments, it appears that the reference pillars now have better mechanical properties than that of the loaded nanopillars. At first, this seems to completely contradict the results from Figures 8.3 and 8.4. But, as seen in Chapter 6, a laser fluence of 144.9 kJ/m^2 is at the onset of bending deformation while at room temperature. This then tells us that if there is even a slight tilt/bend of the loaded pillars, this testing procedure is no longer only a compression test, it is now a compression and bending test. While that is occurring, the reference pillar is only subjected to a compression test so these tests are therefore not directly comparable.

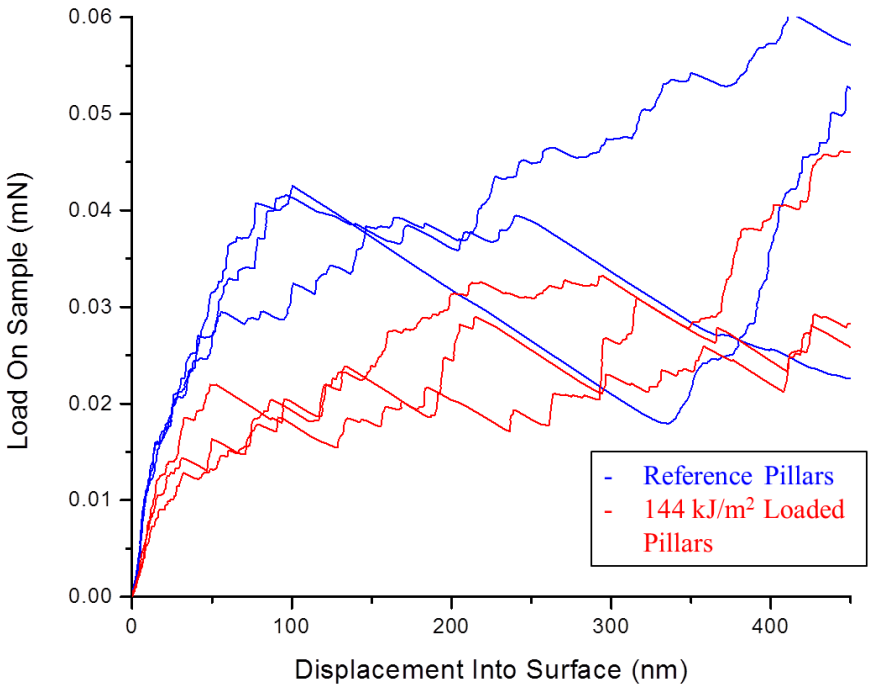

FIG. 8.5. Hysitron in-situ pico-compression testing stress strain curves of reference (not shock-loaded) and shock-loaded at 144.9 kJ/m^2 Cu nanopillars.

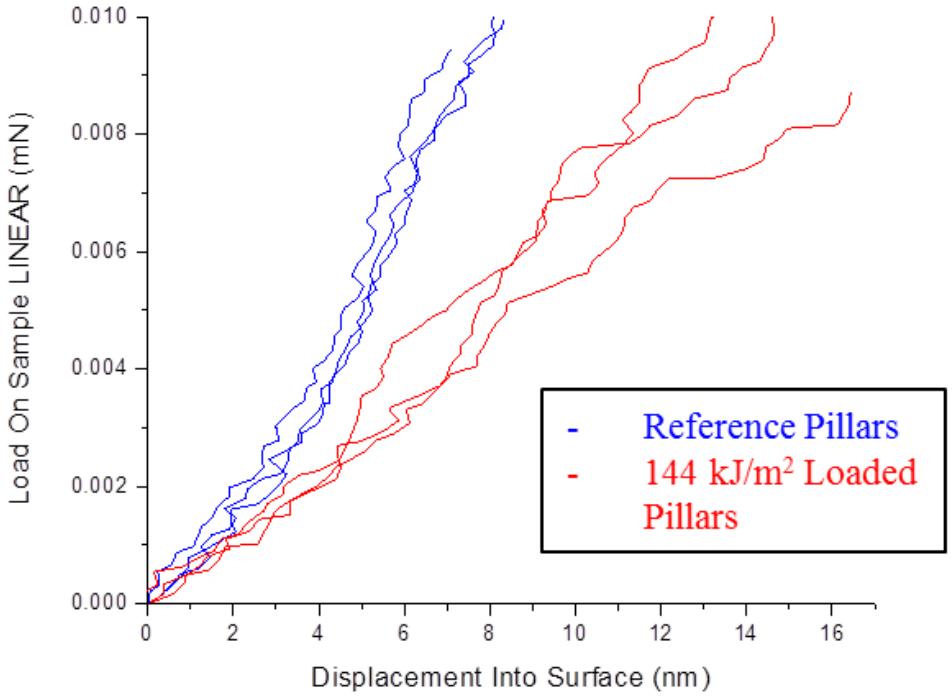

FIG. 8.6. Hysitron in-situ pico-compression testing stress strain curves of reference (not shock-loaded) and shock-loaded at 144.9 kJ/m^2 Cu nanopillars from the elastic/linear region of FIG. 8.5.

In order to compare to bulk testing, indentation testing was completed upon the regions of the copper bulk single crystal loaded with varying states of stress. The laser fluence values used were 0 kJ/m^2 (Reference), 38.8 kJ/m^2, 63.5 kJ/m^2, 91.7 kJ/m^2 and 114 kJ/m^2. It is shown in Table 8.1 below that the average elasticity modulus (E_{avg}) and the hardness (H_{avg}) values do not demonstrate any significant changes for the bulk copper piece after loading with laser induced stress waves, especially as the standard deviation of all regions were greater than 1 GPa and 0.02 GPa for E_{avg} and H_{avg}, respectively. This implies a clear size effect that influences the testing of the nanopillars.

Laser Fluence (kJ/m^2)	E_{avg} (GPa)	H_{avg} (GPa)
0 kJ/m^2	115.9	0.885
38.8 kJ/m^2	114.3	0.929
63.5 kJ/m^2	115.0	0.901
91.7 kJ/m^2	115.4	0.968
114.9 kJ/m^2	113.7	0.934

Table 8.1. Bulk indentation testing of regions subjected to varying states of stress.

In summary, Cu nanopillars that were shock loaded at laser fluence levels of 85 kJ/m^2 and 144.9 kJ/m^2 were compared to reference nanopillars from the same Cu substrate. The pillars that were shock loaded at 85 kJ/m^2 demonstrated improved mechanical properties as well as more brittle failure than that of the reference pillar. This was attributed to microstructural changes in the pillar as was observed in Chapter 3. The pillars that were loaded at 144.9 kJ/m^2 contrary to what would be expected showed diminished mechanical properties. This was the case because these pillars were at the onset of bending deformation as was observed in Chapter 6 for Cu nanopillars loaded at room temperature by a 144.9 kJ/m^2 laser fluence.

9 Conclusions and Future Work

9.1 Conclusions

Modifications were made to the Laser Spallation Technique in order to load structures under a single transient wave pulse. This study characterized FCC nanostructures shock loaded at extreme pressures, strain rates and temperatures. By utilizing nanostructures, extremely large values of stain were capable of being produced within the structure. It was first observed that at lower laser fluence levels and low stress states that there was chemical activation of the surface of Cu nanopillars. This was created by nanofacet formation on the surface of the nanopillars leaving pristine Cu surfaces to recombine with the environment. Dislocation motion was also observed and clearly identified in Cu nanopillars, Cu nanobenches and Al nanopillars. Further studies analyzed Cu nanopillars subjected to higher laser fluence generated stress waves, which led to bending and bulging deformation. These deformations were observed at laser fluence values of 144.9 kJ/m^2 for bending and 303.3 kJ/m^2 for bulging similar to that of Taylor Impact experiments. To explore a more extreme loading environment, a specialized test setup was employed to cryogenically cool the copper nanopillars to a temperature of 83K in an attempt to elucidate brittle behavior. Under these loading conditions the nanopillars continued to deform in a ductile manner but with delayed onset of both bending deformation and bulging deformation. Finally, the mechanical behavior of the Cu nanopillars was studied by nanocompression testing and compared to that of a reference nanopillar from the same substrate. The mechanical properties of the copper pillar were improved at lower laser fluence levels. At higher laser fluence levels, the tests

were inconclusive as slight bending of the shock loaded Cu nanopillars rendered the comparison to the non-deformed reference nanopillar inconclusive.

9.2 Recommendations

There are several recommendations for future work that I would suggest. First, a study of FCC structures with a crystallographic orientation different than the (001) direction. FCC metals have shown to demonstrate anisotropy.

Also, when studying the nanopillars, a more uniform structure would lead to easier analysis via Hysitron nanoindentation but also in any deformation obtained through the shock-loading process would be potentially visible in the SEM. This could mesh nicely with the nanofacet hypothesis in Chapter 3.

The next area of study would be analyzing nanostructures of different crystallographic structures. The most intriguing of these is studying BCC metals. These metals can actually be applied to systems undergoing the pressures, strains and strain rates that are observed in this study. BCC metals are more brittle and are more temperature dependent with regards to overcoming the Peierls barrier. The goal of a study like this is to see if a BCC metal like Tungsten (W) could be made to be ductile under all loading conditions. This query is of interest because of its significance to our society as this would allow design of energy-absorbing blast resistant structures and armors that are critically needed for defense and space exploration applications. In addition, the possibility of making W ductile at room temperature is very tantalizing as it would

expand its application domain considerably and also lead to tremendous cost savings as because of its brittleness W must be heated during most machining operations.

A. Appendix

A.1 FIB prepared nanostructure recipes

For each sample that was prepared, regardless of nanostructure type or material (Cu or Al), there were commonalities utilized in the processing setups. These are covered here. Each of the single crystal pieces (Al or Cu) were oriented in the (100) direction with dimensions of 10mm x 10mm x 0.5mm. For each sample, four different regions were milled via FIB in locations 2.5mm in both the lateral and vertical directions from the corners of the piece (see Figure A.1).

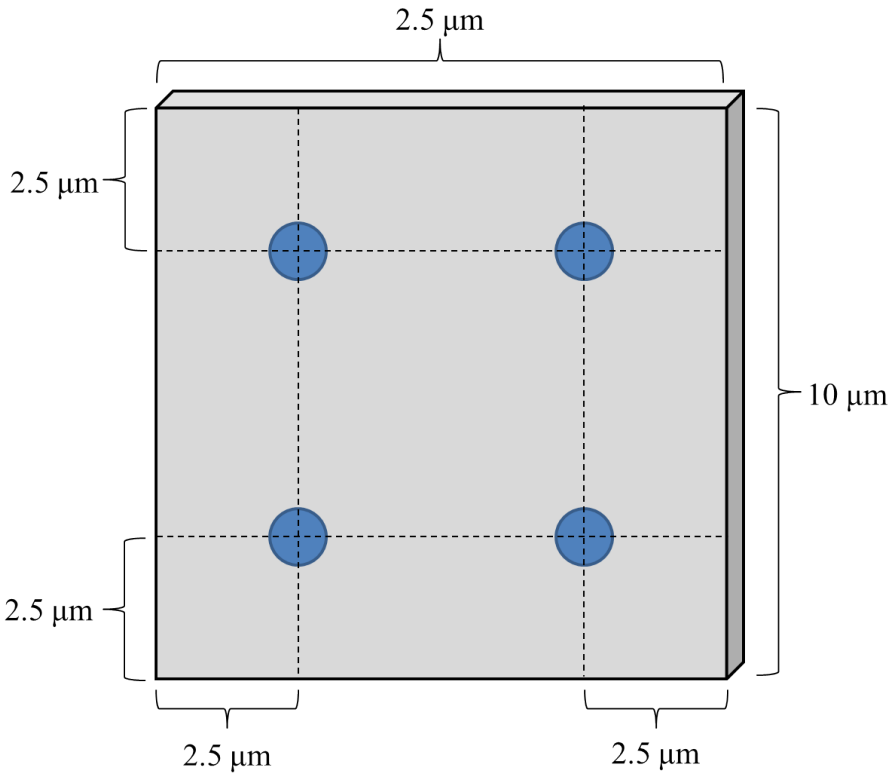

FIG. A.1. Schematic demonstrating the regions in which nanostructures were fabricated via FIB.

As well, each given region was comprised of 6-8 nanostructure samples and a location ‘T’ marker. This location ‘T’ marker was added to simplify the process of finding these nanostructures and help distinguish between different regions. All the nanostructures were placed in the same position relative to the ‘T’ for a given sample. Depending upon the closest corner of the single crystal substrate, it was easy to keep track of given regions both in the optical and scanning electron microscopes. A given FIB fabricated region had characteristics of Figure A.2 below.

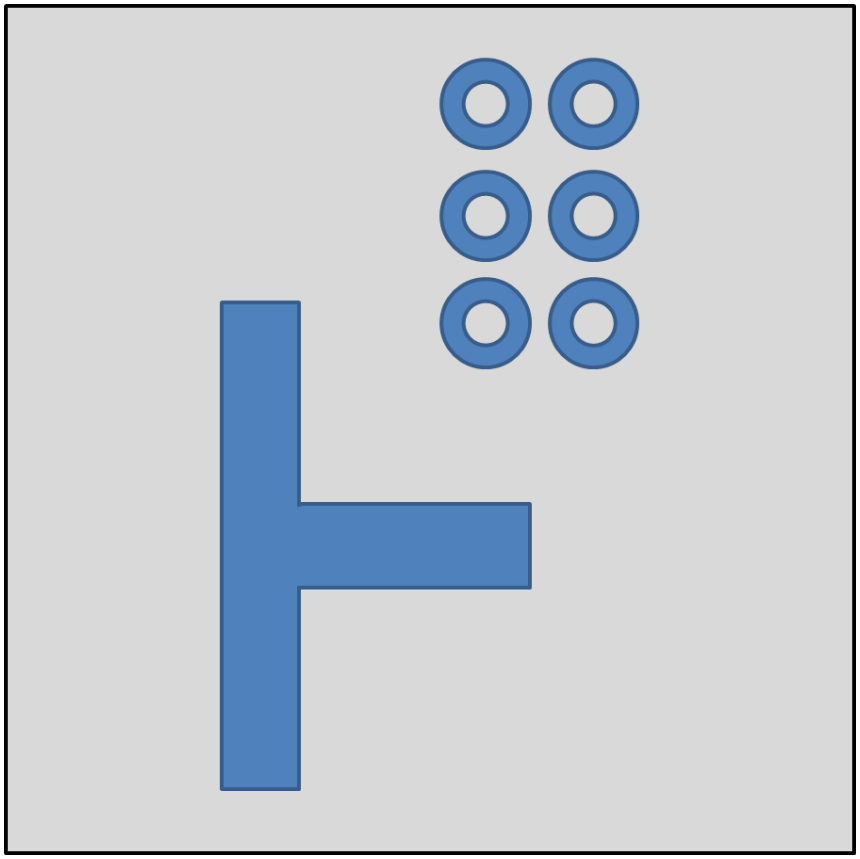

FIG. A.2. Schematic demonstrating the typical setup of a given FIB milled region with the location ‘T’ marker and the nanostructures. The regions in blue are where FIB milling will be done.

A.1.1 Copper nanostructures

A.1.1.1 Copper nanopillars for shock-loading

For these given samples, a specific ptf file was consistently used. This file consisted of an annular ring, shown in Figure A.3 with an inner diameter (ID) of 0.5 μm and outer diameter (OD) of 2.5 μm. As well, a mill depth (Z) of 0.75 μm and a Ga^+ current (I) of 0.5 nA was utilized. The distance from the center of one pillar to another pillar was kept constant at 3.5 μm.

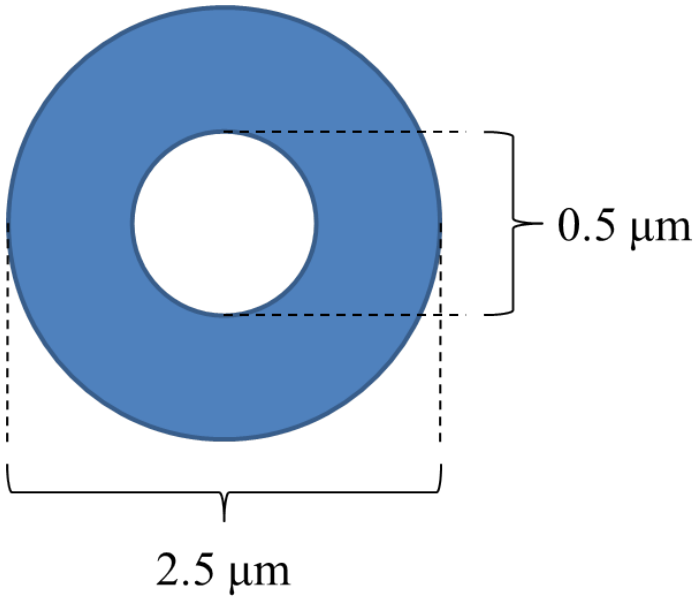

FIG. A.3. Schematic of the annular ring used for the FIB nanopillar milling process.

A.1.1.2 Copper nanopillars for shock-loading and nanocompression

For the nanocompression testing, a modified methodology was necessary as the nanoindenter's tip was 8-10 μm in diameter which would not be capable of directly compressing the pillars in the standard 2.5 μm well. Therefore, a two-step process was employed to obtain pillars of the same dimensions as described in A.1.1.1 but with a

milled out region of 20 μm in diameter. To complete this process, two sets of annular rings were used. The first had an outer diameter of 20 μm and inner diameter of 2.5 μm. This annular ring was used for the first milling steps with the depth of the milling (Z) set to 0.6 μm with a current (I) of 5 nA. Following this step, the second annular ring was used to produce a pillar in the middle of the previously milled region with a 20 μm diameter. The dimensions of the second annular ring were identical to that of A.1.1.1 with the outer diameter of 2.5 μm and inner diameter of 0.5 μm. The milling conditions were milling depth of 0.45 μm and current of 0.5 nA.

A.1.1.3 Copper benches for shock-loading

In order to fabricate nanobenches, it was required that milling was created at an angle to the single crystal's surface. This angle was set to 52° from the perpendicular to the surface. After rotating the angle of incidence of the Ga^+ ions, a rectangle of dimensions of 1.1 μm and 1.0 μm in x and y directions, respectively were used. This was done six separate times with a distance between adjoining rectangles of 1 μm. After this cut the sample was rotated 180° and a second cut was made using the same six rectangles. For the first cut, the mill depth (Z) was set to 1 μm with a current of 0.5 nA. For the second cut, the mill depth (Z) was 0.75 μm with a current of 0.5 nA. Finally, as a final cleanup cut, the sample was rotated 180° again, back to the original cut orientation. This setup a third cut. This third cut was meant to remove any copper that was FIB'ed from the second cut and deposited upon the bench. This final cut used rectangles of the same 1.1 μm by 1.0 μm dimensions with a mill depth of 0.2 μm and current of 0.5 nA.

A.1.2 Aluminum nanostructures

A.1.2.1 Aluminum nanopillars for shock-loading

For the Aluminum nanopillar samples, a specific ptf file was consistently used. This file consisted of two annular rings, shown in Figure A.3 with an inner diameter (ID) of 0.7 μm and outer diameter (OD) of 2.5 μm. As well, a mill depth (Z) of 1.5 μm and a Ga^{+} current (I) of 0.5 nA was utilized.

References

[1] C. M. Lund and D. J. Steinberg, “A constitutive model for strain rates from 10^-4 to 10^6 s^-1,” *J. Appl. Phys.*, vol. 65, no. February 15, 1989, pp. 1528–1533, 1989.

[2] D. J. Steinberg, S. G. Cochran, and M. W. Guinan, “A constitutive model for metals applicable at high-strain rate,” *J. Appl. Phys.*, vol. 94550, no. November 1979, pp. 1498–1504, 1980.

[3] D. L. Preston, D. L. Tonks, and D. C. Wallace, “Model of plastic deformation for extreme loading conditions,” *J. Appl. Phys.*, vol. 93, no. 1, p. 211, 2003.

[4] K. G. Hoge and a. K. Mukherjee, “The temperature and strain rate dependence of the flow stress of tantalum,” *J. Mater. Sci.*, vol. 12, no. 8, pp. 1666–1672, Aug. 1977.

[5] P. S. Follansbee and U. F. Kocks, “A constitutive description of the deformation of copper based on the use of the mechanical threshold stress as an internal state variable,” *Acta Metall.*, vol. 36, no. 1, pp. 81–93, Jan. 1988.

[6] F. J. Zerilli, N. Surface, and S. Spring, “The effect of dislocation drag on the stress-strain behavior of f.c.c. metals,” *Acta Metall. Mater.*, vol. 40, no. 8, pp. 1803–1808, 1992.

[7] G. R. Johnson, J. M. Hoegfeidt, U. S. Lindholm, and A. Nagy, “Response of Various Metals to Large Torsional Strains Over a Large Range of Strain Rates - Part 2: Less Ductile Metals,” *J. Eng. Mater. Technol.*, vol. January, pp. 48–53, 1983.

[8] L. Li and N. Ghoniem, “Twin-size effects on the deformation of nanotwinned copper,” *Phys. Rev. B*, vol. 79, no. 7, p. 075444, Feb. 2009.

[9] B. a. Remington, P. Allen, E. M. Bringa, J. Hawreliak, D. Ho, K. T. Lorenz, H. Lorenzana, J. M. McNaney, M. a. Meyers, S. W. Pollaine, K. Rosolankova, B. Sadik, M. S. Schneider, D. Swift, J. Wark, and B. Yaakobi, “Material dynamics under extreme conditions of pressure and strain rate,” *Mater. Sci. Technol.*, vol. 22, no. 4, pp. 474–488, Apr. 2006.

[10] M. Kiritani, “Analysis of high-speed-deformation-induced defect structures using heterogeneity parameter of dislocation distribution,” *Mater. Sci. Eng. A*, vol. 350, no. 1–2, pp. 63–69, Jun. 2003.

[11] M. Kiritani, K. Yasunaga, Y. Matsukawa, and M. Komatsu, “Plastic Deformation of Thin Metal Foils without Dislocations and Formation of Point Defects and Point Defect Clusters,” *MRS Proc.*, vol. 673, no. 100, pp. 1–6, 2001.

[12] E. M. Bringa, A. Caro, Y. Wang, M. Victoria, J. M. McNaney, B. a Remington, R. F. Smith, B. R. Torralva, and H. Van Swygenhoven, “Ultrahigh strength in nanocrystalline materials under shock loading.,” *Science*, vol. 309, no. 5742, pp. 1838–1841, Sep. 2005.

[13] D. Seif, G. Po, R. Crum, V. Gupta, and N. M. Ghoniem, “Shock-induced plasticity and the Hugoniot elastic limit in copper nano films and rods,” *J. Appl. Phys.*, vol.

115, no. 5, p. 054301, Feb. 2014.

[14] B. A. Remington, G. Bazan, J. Belak, E. Bringa, M. Caturla, J. D. Colvin, M. J. Edwards, S. G. Glendinning, D. S. Ivanov, B. Kad, and D. H. Kalantar, "Materials Science Under Extreme Conditions of Pressure and Strain Rate," *Metall. Mater. Trans. A*, vol. 35, no. 9, pp. 2587–2607, 2004.

[15] D. Seif, G. Po, R. Crum, S. Kodambaka, S. V. Prikhodko, V. Gupta, and N. M. Ghoniem, "Ultra-High Strain Rate Deformation of Nano-Structured FCC and BCC Metals," in *Proceedings of the 8th European Solid Mechanics Conference*, 2012.

[16] K. T. Ramesh, "High Strain R 33.1," *Handb. Exp. Solid Mech.*, p. 874, 2008.

[17] M. A. Meyers, *Dynamic Behavior of Materials*. New York: John Wiley and Sons, Inc., 1994.

[18] V. Gupta and J. Yuan, "Measurement of interface technique. II. Applications strength by the modified laser spallation to metal/ceramic interfaces," *J. Appl. Phys.*, vol. 74, no. 4, pp. 2397–2404, 1993.

[19] V. Gupta, A. S. Argon, D. M. Parks, and J. A. Cornie, "Measurement of Interface Strength by a Laser Spallation Technique," *J. Mech. Phys. Solids*, vol. 40, no. I, pp. 141–180, 1992.

[20] V. Gupta, J. Yuan, and A. Pronin, "Nanosecond rise-time laser-produced stress pulses with no asymptotic decay," *Rev. Sci. Instrum.*, vol. 64, no. 6, p. 1611, 1993.

[21] V. Gupta, Y. Jun, and A. Pronin, "Recent developments in the laser spallation technique to measure the interface strength and its relationship to interface toughness with applications to metal/ceramic, ceramic/ceramic and ceramic/polymer interfaces," *J. Adhes. Sci. Technol.*, vol. 8, no. 6, pp. 713–747, 1994.

[22] X. Wang, V. Gupta, and S. N. Basu, "Effects of Substrate Orientation and Metal Film Thickness on the Intrinsic Strength, Intrinsic Fracture Energy, and Total Fracture Energy of Tantalum-Sapphire Interfaces," *J. Am. Ceram. Soc.*, vol. 88, no. 7, pp. 1909–1913, Jul. 2005.

[23] A. Pronin and V. Gupta, "lnterferometry on diffuse surfaces in high-velocity measurements," *Rev. Sci. Instrum.*, vol. 64, no. August, pp. 2233–2236, 1993.

[24] J. Yuan and V. Gupta, "The effect of Microstructure and Chemistry on the Tensile Strength of Nb/Sapphire Interfaces with and without Interlayers of Sb and Cr," *Acta Metall. Mater.*, vol. 43, no. 2, pp. 781–794, 1995.

[25] J. Yuan, V. Gupta, and M. Kim, "Structure and Chemistry of Nb/Sapphire Interfaces, With and Without Interlayers of Sb and Cr," *Acta Metall. Mater.*, vol. 43, no. 2, pp. 769–779, 1995.

[26] V. Gupta, J. Wu, and A. N. Pronin, "Effect of Substrate Orientation, Roughness, and Film Deposition Mode on the Tensile Strength and Toughness of Niobium-Sapphire Interfaces," *J. Am. Ceram. Soc.*, vol. 80, no. 12, pp. 3172–3180, Jan. 2005.

[27] L. C. Lev and A. S. Argon, "Spallation of thin elastic coatings from elastic

substrates by laser induced pressure pulses," *J. Appl. Phys.*, vol. 80, no. 1, p. 529, 1996.

[28] M. D. Uchic, D. M. Dimiduk, J. N. Florando, and W. D. Nix, "Sample dimensions influence strength and crystal plasticity.," *Science*, vol. 305, no. 5686, pp. 986–9, Aug. 2004.

[29] V. Sriram, J. Yang, J. Ye, and A. M. Minor, "Determining the Stress Required for Deformation Twinning in Nanocrystalline and Ultrafi ne-grained," *JOM*, vol. 60, no. 9, pp. 66–70, 2008.

[30] D. Hull and D. J. Bacon, "Introduction to Dislocations." 2001.

[31] M. D. Uchic and D. M. Dimiduk, "A methodology to investigate size scale effects in crystalline plasticity using uniaxial compression testing," *Mater. Sci. Eng. A*, vol. 400–401, no. ., pp. 268–278, Jul. 2005.

[32] J. Y. Kim and J. R. Greer, "Tensile and compressive behavior of gold and molybdenum single crystals at the nano-scale," *Acta Mater.*, vol. 57, no. 17, pp. 5245–5253, Oct. 2009.

[33] D. Jang, C. Cai, and J. R. Greer, "Influence of homogeneous interfaces on the strength of 500 nm diameter Cu nanopillars.," *Nano Lett.*, vol. 11, no. 4, pp. 1743–6, Apr. 2011.

[34] A. T. Jennings, M. J. Burek, and J. R. Greer, "Microstructure versus size: mechanical properties of electroplated single crystalline Cu nanopillars.," *Phys. Rev. Lett.*, vol. 104, no. 13, pp. 135503–1 – 135503–4, Apr. 2010.

[35] J. R. Greer, C. R. Weinberger, and W. Cai, "Comparing the strength of f.c.c. and b.c.c. sub-micrometer pillars: Compression experiments and dislocation dynamics simulations," *Mater. Sci. Eng. A*, vol. 493, no. 1–2, pp. 21–25, Oct. 2008.

[36] M. J. Burek and J. R. Greer, "Fabrication and microstructure control of nanoscale mechanical testing specimens via electron beam lithography and electroplating.," *Nano Lett.*, vol. 10, no. 1, pp. 69–76, Jan. 2010.

[37] A. T. Jennings and J. R. Greer, "Tensile deformation of electroplated copper nanopillars," *Philos. Mag.*, vol. 91, no. 7–9, pp. 1108–1120, Mar. 2011.

[38] J. R. Greer, J.-Y. Kim, and M. J. Burek, "The in-situ mechanical testing of nanoscale single-crystalline nanopillars," *Jom*, vol. 61, no. 12, pp. 19–25, Dec. 2009.

[39] A. T. Jennings, J. Li, and J. R. Greer, "Emergence of strain-rate sensitivity in Cu nanopillars: Transition from dislocation multiplication to dislocation nucleation," *Acta Mater.*, vol. 59, no. 14, pp. 5627–5637, Aug. 2011.

[40] Z. W. Shan, R. K. Mishra, S. a Syed Asif, O. L. Warren, and A. M. Minor, "Mechanical annealing and source-limited deformation in submicrometre-diameter Ni crystals.," *Nat. Mater.*, vol. 7, no. 2, pp. 115–9, Feb. 2008.

[41] J. Yuan and V. Gupta, "Measurement of interface strength by the modified laser spallation technique. 1. Experiment and simulation of the spallation process," *J. Appl. Phys.*, vol. 74, no. 4, pp. 2388–2396, 1993.

[42] J. Yuan, V. Gupta, and A. Pronin, “Measurement of interface strength by the modified laser spallation technique. III. Experimental optimization of the stress pulse,” *J. Appl. Phys.*, vol. 74, no. 4, pp. 2405–2410, 1993.

[43] G. Youssef and V. Gupta, “Dynamic tensile strength of polyurea,” *J. Mater. Res.*, vol. 27, no. 2, pp. 494–499, Dec. 2011.

[44] G. Youssef, C. Moulet, M. S. Goorsky, and V. Gupta, “Inter-wafer bonding strength characterization by laser-induced shock waves,” *J. Appl. Phys.*, vol. 111, no. 9, pp. 0–4, 2012.

[45] V. Gupta, V. Kireev, J. Tian, H. Yoshida, and H. Akahoshi, “Glass-modified stress waves for adhesion measurement of ultra thin films for device applications,” *J. Mech. Phys. Solids*, vol. 51, no. 8, pp. 1395–1412, Aug. 2003.

[46] A. N. Pronin and V. Gupta, “Measurement of Thin Film Interface Toughness By Using Laser-Generated Pulses,” *J. Mech. Phys. Solids*, vol. 46, no. 3, pp. 389–410, 1998.

[47] L. M. Barker, “Shock-Wave Studies of PMMA, Fused Silica, and Sapphire,” *J. Appl. Phys.*, vol. 41, no. 10, p. 4208, 1970.

[48] R. J. Clifton, “Analysis of the Laser Velocity Interferometer,” *J. Appl. Phys.*, vol. 41, no. 13, p. 5335, 1970.

[49] G. Youssef and V. Gupta, “Dynamic response of polyurea subjected to nanosecond rise-time stress waves,” *Mech. Time-Dependent Mater.*, vol. 16, no. 3, pp. 317–328, Nov. 2011.

[50] G. H. Youssef, “Dynamic Properties of Polyurea,” *UCLA Diss.*, 2011.

[51] N. I. Kato, “Reducing focused ion beam damage to transmission electron microscopy samples,” *J. Electron Microsc. (Tokyo).*, vol. 53, no. 5, pp. 451–458, Oct. 2004.

[52] L. E. Samuels, *Metallographic polishing by mechanical methods*, 3rd ed. Materials Park, OH: American Society of Metals, 1982.

[53] W. T. Read, *Dislocations in Crystals*. New York: McGraw-Hill, 1953.

[54] J. W. Edington, *Practical Microscopy in Materials Science*. New York: Vn Nostrand Reinhold Co., 1976.

[55] E. M. Bringa, K. Rosolankova, R. E. Rudd, B. A. Remington, J. S. Wark, M. Duchaineau, D. H. Kalantar, J. Hawreliak, and J. Belak, “Shock deformation of face-centred-cubic metals on subnanosecond timescales.,” *Nat. Mater.*, vol. 5, no. 10, pp. 805–9, Oct. 2006.

[56] E. M. Bringa, B. D. Wirth, M. J. Caturla, J. Stölken, and D. Kalantar, “Metals far from equilibrium: From shocks to radiation damage,” *Nucl. Instruments Methods Phys. Res. Sect. B Beam Interact. with Mater. Atoms*, vol. 202, pp. 56–63, Apr. 2003.

[57] L. P. Dávila, P. Erhart, E. M. Bringa, M. a. Meyers, V. a. Lubarda, M. S. Schneider, R. Becker, and M. Kumar, “Atomistic modeling of shock-induced void collapse in copper,” *Appl. Phys. Lett.*, vol. 86, no. 16, p. 161902, 2005.

[58] E. M. Bringa, J. U. Cazamias, P. Erhart, J. Stolken, N. Tanushev, B. D. Wirth, R. E. Rudd, and M. J. Caturla, "Atomistic shock Hugoniot simulation of single-crystal copper," *J. Appl. Phys.*, vol. 96, no. 7, pp. 3793–3799, 2004.

[59] G. H. Youssef, "Los Angeles Dynamic Properties of Polyurea by," 2010.

[60] G. Youssef, R. Crum, S. V Prikhodko, D. Seif, G. Po, N. Ghoniem, S. Kodambaka, and V. Gupta, "The influence of laser-induced nanosecond rise-time stress waves on the microstructure and surface chemical activity of single crystal Cu nanopillars.," *J. Appl. Phys.*, vol. 113, no. 8, p. 84309, Feb. 2013.

[61] D. B. Williams and C. B. Carter, *Transmission Electron Microscopy*. New York: Springer Science+Business Media, LLC, 1996.

[62] E. Orowan, "A Type of Plastic Deformation New in Metals," *Nature*, vol. 149, pp. 643–644, 1942.

[63] H. a. Colorado, a. Navarro, S. V. Prikhodko, J. M. Yang, N. Ghoniem, and V. Gupta, "Ultrahigh strain-rate bending of copper nanopillars with laser-generated shock waves," *J. Appl. Phys.*, vol. 114, no. 23, p. 233510, 2013.

[64] G. Taylor, "The use of flat-ended projectiles for determining dynamic yield stress I . Theoretical considerations," *Society*, vol. 194, no. 1038, pp. 289–299, 2009.

[65] M. L. Wilkins and M. W. Guinan, "Impact of cylinders on a rigid boundary," *J. Appl. Physics1*, vol. 44, p. 1200, 1973.

[66] S. Sarva, A. D. Mulliken, and M. C. Boyce, "Mechanics of Taylor impact testing of polycarbonate," *Int. J. Solids Struct.*, vol. 44, no. 7–8, pp. 2381–2400, 2007.

[67] S. E. Jones, J. a. Drinkard, W. K. Rule, and L. L. Wilson, "An elementary theory for the Taylor impact test," *Int. J. Impact Eng.*, vol. 21, no. 1–2, pp. 1–13, 1998.

[68] J. E. Field, S. M. Walley, W. G. Proud, H. T. Goldrein, and C. R. Siviour, *Review of experimental techniques for high rate deformation and shock studies*, vol. 30, no. 7. 2004.

[69] R. K. Spears, "Dielectric characteristics of PZT 95/5 ferroelectric ceramics at high pressures," *Ferroelectrics*, vol. 37, no. 1, p. 653, 1981.